Charles University in Prague
Faculty of Mathematics and Physics

Doctoral Thesis

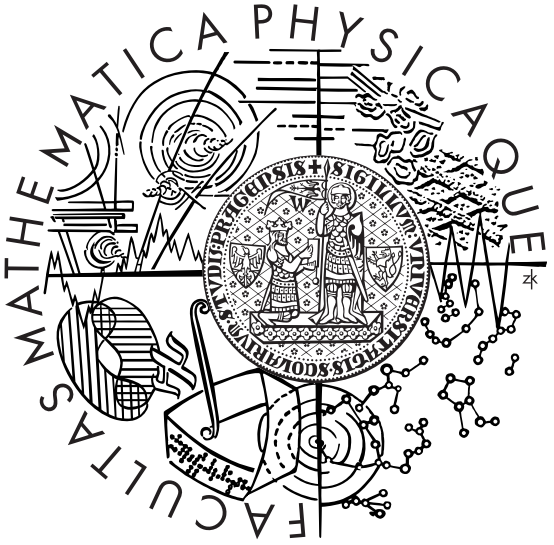

Cohesive and magnetoelastic properties of materials with strongly correlated electrons

Jan Prokleška

Department of Condensed Matter Physics

Supervisor: Prof. RNDr. Vladimír Sechovský, DrSc.

Prague, April 2008

Acknowledgements

Here I would like to thank everyone who supported me and helped me with the work described in this thesis. First of all, I would like to thank my supervisor Prof. RNDr. Vladimír Sechovský, DrSc. for his guidance and support during my studies and for his valuable comments and suggestions during writing my thesis.
I am indebted to Dr. Garry McIntyre for his kind guidance during my stay at ILL, Grenoble and for introducing me into the world of the Laue diffraction.
This work could not have been possible also without a high quality single crystals provided by RNDr. Jana Poltierová Vejpravová, Ph.D., Prof. Dr. Alexander V. Andreev and Mgr. Matuš Mihálik.
I would like to thank Dr. Fuminori Honda for introducing me into the methods of thermal expansion measurements. I also thank Ing. Josef Šebek, Ph.D. and RNDr. Eva Šantavá, CSc. for their help with performing experiments in the JLMS. Many thanks also belong to Mgr. Blanka Detlefs, Ph.D. for her help during my stay at ILL, Grenoble. I express thanks to other colleagues and friends from our department and JLMS for friendly and stimulative atmosphere, especially to RNDr. Jiří Prchal, PhD.

Contents

List of Figures

List of Tables

List of symbols

B	magnetic field (magnitude)
$\mathbf{B}$	magnetic field (vector)
B_l^m	crystal field parameters
B_c	critical field
C	capacitance
C_V	heat capacity at constant volume
c_V	specific heat capacity at constant volume
d	gap between capacitor plates
$\left\{\frac{\Delta l}{l}\right\}$	relative linear change
E_F	Fermi energy
ΔF_m	magnetic free energy
I_S	Stoner exchange integral
k_B	Boltzman constant
$\mathbf{k}$	wavevector
M	magnetisation
O_l^m	Stevens operators
p	pressure
$\mathbf{Q}$	momentum transfer
$\mathbf{Q_1}$	unit vector in the direction of the momentum transfer
$\mathbf{q}$	propagation vector
S	entropy
T	temperature
T_C	Curie temperature
T_c	critical temperature
T_N	Néel temperature
T_t	transition temperature
V	volume
α	coefficient of linear thermal expansion
α_V	coefficient of volume thermal expansion
γ_G	Grüneisen function
κ_T	isothermal compressibility
κ_S	adiabatic compressibility

θ_{p}	paramagnetic Curie temperature
ϱ	electrical resistivity
μ_{eff}	effective moment
μ_{B}	Bohr magneton
$\boldsymbol{\mathcal{N}}(E_{\mathrm{F}})$	density of states at the Fermi energy
$\boldsymbol{\mathcal{H}}$	Hamiltonian

Chapter 1

Introduction

One of main motivations for extensive study of rare earth compounds is the fact that their properties are notably different from the properties of each of individual components. Large number of isostructural and isoelectronic series allow well controlled changing of electronic properties and therefore large field for testing of theoretical models and approaches. The rare-earth intermetallics are in a prominent situation not only from a fundamental point of view but also for the large number of technological applications.

Large number of ground states and complexity of magnetic phase diagrams is a challenge for experimental physicists trying to map the physical properties as well as for theoreticians developing the formalisms capable of describing and predicting ground state properties and their evolution with application of external parameters (temperature, magnetic filed, pressure).

Due to the relatively small effects accompanying the magnetic ordering at low temperatures, there is a lack of the high quality elastic data, especially the determination of the full elastic tensor is very seldom, contrary to fact that strong anisotropic properties are observed in many of these compounds. Lately, the development of capacitance dilatometry allows construction of the compact and relatively simple dilatometric cells. This allows measurements of small single crystal samples with sensitivity higher than in the case of using a strain gauge or majority of diffraction methods. One of the goals of this thesis is to interface one of these microdilatometers to the PPMS apparatus in the Joint Laboratory of Magnetic Studies and develop an approach to the data measurement and evaluation.

An important part in the investigation of magnetic materials is the determination of the magnetic structure in the ordered state using neutron diffraction. This is done in some of the international facilities, using either powder or single crystal instruments. The powder crystal instruments allow fast acquisition of all (in principle) available data, however, the interpretation may be ambiguous, especially in the case of complex magnetic structures. On the contrary, the majority of single crystal instruments is capable of thorough investigation which may be rather time consuming due to the fact that detector is usually covering only small portion of the reciprocal space. As a solution the usage of a white neutron beam with large detector is possible (e.g. VIVALDI in ILL, Grenoble). However, this face to the

problems with the data evaluation in compounds with a complicated propagation vector, more specifically with the propagation vector determination and intensity integration and evaluation. As a part of this thesis a set of routines should be proposed and written, which allow to bypass this imperfection in the current data evaluation and profit from the full range of VIVALDIs capabilities in the reciprocal space.

Using the microdilatometric capacitance cell in this work, single crystals of selected anisotropic compounds are studied, in order to investigate the temperature and field dependence of the elastic tensor. A selection was made in the way that interesting phenomena or novel compounds are studied in detail. Two uranium compounds (UCoAl and UNiAl) were selected due to several unanswered question concerning their behaviour above characteristic temperatures, namely the possible contribution from spin fluctuation to elastic properties. In the NdRhSn compound the unclear ordering scheme was investigated in order to clarify the contradictory claims in literature. A detail investigation of the irreversible phase in the CePtSn was done, connected with the study of the field and temperature dependencies of the elastic tensor in the low temperate region. The last compound studied in this thesis is $PrCo_2Co_2$, antiferromagnetically ordered in low temperatures with strong anisotropy, firstly prepared in a single crystal form.

Thesis organisation

The theory behind the observed phenomena is summarised in the chapter 2. Chapter 3 is devoted to the description of used methods for sample investigation followed by discussion of the data evaluation, when necessary. Main emphasis is placed on the description of the novel microdilatometric cell used for the measurement of elastic properties and the evaluation of the obtained data, as well as on the neutron diffraction, particulary on the single crystal Laue diffraction and the propagation vector determination from the Laue patterns. The next chapter is devoted to the presentation of obtained experimental data, each subsection is introduced by a overview of previous results and concluded by partial résumé. In the last chapter the overall discussion of the results is presented followed by concluding remarks and a suggestion of possible directions in the future investigation.

Chapter 2

General theory

2.1 Itinerant-electron and local-moment model

Magnetic properties of metallic materials can be understood in the framework of two basic approaches - the itinerant electron model and the model in which localised magnetic moments are assumed. Both models can be well used in fact only in limit cases.
The next two sections briefly summarise the basics of these two approaches (free-ion-like and itinerant-electron model) and discuss their appearance in the real cases. General notes are discussed about the impact on the magnetism of the intermetallic compounds.

2.1.1 Local moment model

Local moment behaviour is usually associated with the magnetic moments of well localised electrons, which do not contribute to conductivity or chemical bonding. Such a situation is well established for 4f electrons in most of the lanthanide based compounds, as the 4f shell lies deeply inside the 5d and 6s shells.[1] This leads to an unique situation when the electrons in a partially filled 4f shell belong to the chemically inert ionic core.

ion		$\frac{\mu_{\mathrm{eff}}}{\mu_{\mathrm{B}}}$	exp
La^{3+}	$4f^0$	0.00	dia
Ce^{3+}	$4f^1$	2.54	2.4
Pr^{3+}	$4f^2$	3.58	3.5
Nd^{3+}	$4f^3$	3.62	3.5
Pm^{3+}	$4f^4$	2.68	—
Sm^{3+}	$4f^5$	0.84	1.5
Eu^{3+}	$4f^6$	0.00	3.4
Gd^{3+}	$4f^7$	7.94	8.0
Tb^{3+}	$4f^8$	9.72	9.5
Dy^{3+}	$4f^9$	10.63	10.6
Ho^{3+}	$4f^{10}$	10.60	10.4
Er^{3+}	$4f^{11}$	9.59	9.5
Tm^{3+}	$4f^{12}$	7.57	7.3
Yb^{3+}	$4f^{13}$	4.54	4.5
Lu^{3+}	$4f^{14}$	0.00	dia

Table 2.1: Comparison of theoretical and experimental values of magnetic moments [1].

The model is based on spatially well defined electron wave functions, which are centred at particular ions. There is a negligible spatial overlap between 4f wave functions of neighbours which allows maintaining a nearly the free-ion form. This leads to the well defined 4f energy levels in the solid, which are only slightly modified with respect to the free-ion sit-

[1] The exceptions are compounds based on cerium, europium and ytterbium in some cases.

uation. Moreover, owing to the fact that the wave functions are limited in space, the electrons have fully developed orbital moments (and accordingly the associated orbital magnetic moments). Probably the most transparent manifestation of the localised character of a system is that the observed effective magnetic moments are close to full values ($\mu_{\mathrm{eff}} = \mu_{\mathrm{B}} g_{\mathcal{J}} \sqrt{J\,(J-1)}$) expected from Hunds rules for a free ion (see Table 2.1).

The local moment model was firstly used to explain the Curie law for the paramagnetic susceptibility [2] and for derivation of Curie-Weiss law with the additional hypothesis of a molecular field [3].

In the case of noninteracting atoms (paramagnetic state) the Hamiltonian can be written in the form

$$\mathcal{H} = -\sum_{i}^{N} \mathbf{m}_i \cdot \mathbf{H} \ .$$

We can express the magnetisation as the thermal average

$$M(T,H) = N \frac{\sum -g\,\mu_{\mathrm{B}} J_z \mathrm{e}^{\frac{-g\,\mu_{\mathrm{B}} J_z H}{k_{\mathrm{B}} T}}}{\sum \mathrm{e}^{\frac{-g\,\mu_{\mathrm{B}} J_z H}{k_{\mathrm{B}} T}}}$$

where the summation is from $-J$ to J in both cases. The summation gives us

$$M = M_0 B_J(x) \tag{2.1}$$

where $B_J(x)$ is Brillouin function

$$B_J(x) = \frac{2J+1}{2J} \coth\left(\frac{2J+1}{2J}x\right) - \frac{1}{2J}\coth\left(\frac{1}{2J}x\right) \ .$$

and M_0 and x are abbreviations for

$$M_0 = N g J\,\mu_{\mathrm{B}}$$
$$x = \frac{g J\,\mu_{\mathrm{B}} H}{k_{\mathrm{B}} T} \ .$$

The classical solution of this problem leads to the expression of the same type as 2.1, just a Brillouin function is replaced by a Langevin function $L(x)$

$$L(x) = \coth(x) - \frac{1}{x} \ .$$

If we are interested in the low field and high temperature behaviour we are looking for the limit

$$\lim_{x\to 0} B_J(x) = \lim_{x\to 0} L(x) = \frac{x}{3}$$

which we can use for the explicit formulation of the temperature dependence of magnetic susceptibility (Curie law)

$$\chi = \left.\frac{\partial M}{\partial B}\right|_{B=0} = C/T$$
$$C = \frac{N \mu_{\mathrm{eff}}^2 \mu_{\mathrm{B}}^2}{3 k_{\mathrm{B}} T}$$

where μ_{eff} can be obtained from experimental data and compared to the theoretical value (see Table 2.1).

2.1.2 Itinerant electron model

The fundamental characteristic for the itinerant electron model is a strong overlap of the charge distributions of neighbouring atoms, which can be found in the 3d, 4d and 5d transition metals (and light actinides) and many compounds containing them, where the d (or 5f) electrons are largely delocalised and contribute to both conductivity and chemical bonding.

The electrons responsible for the magnetic moments originate from uncompletely filled shells in metals and they are situated below (in energy and space scale) electrons forming conduction bands. In this case relatively wide energy bands are formed, occupied according to the Pauli exclusion principle. These electrons loose completely or nearly completely the non-zero time averaged angular momentum (and hence the magnetic orbital moment).[2] The magnetism is mainly of spin origin with presence of a small orbital contribution due to spin orbit interaction (see Table 2.3).

The effort to describe a metallic state started with the free electron gas model developed by Pauli [4]. After the development of the electron band model Bloch [5], Mott [6] and Slater [7], [8] advanced the description of the metallic state as the electron gas, which was finalised by Stoner [9], [10], who succeeded to formulate a phenomenological molecular field model (analogous to the Weiss model) by employing the electronic bandstructure instead of the discrete angular momentum levels. Stoner formulated model of itinerant electron magnetism on the following postulates:

- The carriers of magnetism are the unsaturated spins in the d-band.
- Effects of exchange interactions are treated within molecular field approximation.
- One must conform to Fermi statistics.

Under these assumptions the so called *Stoner criterion* for a spontaneous magnetic order of a system of itinerant electrons can be derived

$$I_{\text{S}}\,\mathcal{N}(E_{\text{F}}) > 1\ , \tag{2.2}$$

element	$\mathcal{N}(E_{\text{F}})$	I_{S}
Li(bcc)	3.25	172
Be(fcc)	0.36	156
Ca(fcc)	10.5	74
Cr(bcc)	4.70	56
Mn(fcc)	10.5	60
Fe(bcc)	21	68
Co(fcc)	14	73
Ni(fcc)	27	74
Cu(fcc)	2	54
Zn(fcc)	2	76
Ga(fcc)	2.8	74
In(fcc)	3.4	30

Table 2.2: Stoner exchange integral I_{S} (in mRy) and density of states at the Fermi energy $\mathcal{N}(E_{\text{F}})$ (in Ry^{-1}) for some metallic elements [11], [12].

[2] Generally, this is not valid for the 5f electrons, see Section 2.3 with more detailed discussion about 5f electron itinerant magnetism specifics and differences in comparison with d electron type itinerant magnetism.

ion		$g_J\sqrt{J(J-1)}$	$g_J\sqrt{S(S-1)}$	exp
K^+, La^{3+}	$3d^0$	0.00	0.00	dia
Ti^{3+}, V^{4+}	$3d^1$	1.55	1.73	1.7
V^{3+}	$3d^2$	1.63	2.83	2.8
V^{2+}, Cr^{3+}, Mn^{4+}	$3d^3$	0.77	3.87	3.8
Cr^{2+}, Mn^{3+}	$3d^4$	0.00	4.90	4.9
Mn^{2+}, Fe^{3+}	$3d^5$	5.92	5.92	5.9
Fe^{2+}	$3d^6$	6.70	4.90	5.4
Co^{2+}	$3d^7$	6.64	3.87	4.8
Ni^{2+}	$3d^8$	5.59	2.83	3.2
Cu^{2+}	$3d^9$	3.55	1.73	1.9
Cu^+, Zn^{2+}	$3d^{10}$	0.00	0.00	dia

Table 2.3: Comparison of theoretical and experimental values of magnetic moments [13].

where I_S is the Stoner exchange integral and $\mathcal{N}(E_F)$ is the density of states at the Fermi energy E_F. The values of $\mathcal{N}(E_F)$ and I_S derived from electronic band calculations [11] (using the KKR[3]–method and the LSDA[4] for exchange and correlation) are in Table 2.2 (for the elements marked in bold the Stoner criterion 2.2 is fulfilled).

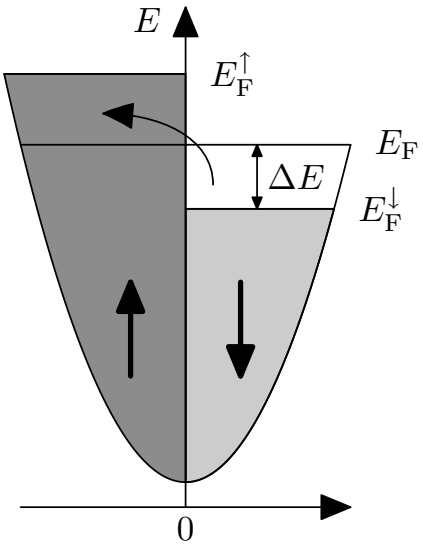

Figure 2.1: Spin split density of states. Fermi energy E_F for non-magnetic split and Fermi energies for spin-up $E_F^{\uparrow}$ and spin-down $E_F^{\downarrow}$.

Criterion 2.2 can be looked into with help of the following simple model (see Fig. 2.1): For obtaining a magnetic moment we move electrons from the small zone (with the bandwidth ΔE) near Fermi level E_F from majority to minority band. To satisfy the Pauli principle they must be shifted to higher energies which cause an increase of kinetic energy ΔE_k. On the other hand, there is a drop in the exchange energy ΔE_{xc} and new (magnetic) conformation will be stable for $\Delta E_k < \Delta E_{xc}$. The change of kinetic energy is given by the number of moved electron states $\Delta N = \mathcal{N}(E_F)\Delta E$ multiplied by the average energy change ΔE of one electron

$$\Delta E_k = \mathcal{N}(E_F)\,(\Delta E)^2 \ . \tag{2.3}$$

The modification of exchange energy can be expressed as

$$\Delta E_{xc} = I_S\, M\, \Delta N = I_S\, \mathcal{N}^2(E_F)\,(\Delta E)^2 \ , \tag{2.4}$$

where M is the magnetisation which is equal to the number of the moved electron states, I_S is the

[3] **K**orringa–**K**ohn–**R**ostoker method [14], [15]
[4] **L**ocal **S**pin **D**ensity **A**pproximation [16]

Stoner exchange integral (effective interaction parameter), the term $I_S M$ is the change of the energy for one electron. When we use 2.3 and 2.4 in the stability condition $\Delta E_k < \Delta E_{xc}$ we get the Stoner criterion 2.2.

Depending on the value of Stoner product $I_S \mathcal{N}(E_F)$, we can distinguish the following types of magnetic materials

- $I_S \mathcal{N}(E_F) < 1$ the compound is a *Pauli paramagnet*
- $I_S \mathcal{N}(E_F) - 1 \simeq 0^-$ the compound is close to the onset of ferromagnetism and exhibits the collective electron *metamagnetism*
- $I_S \mathcal{N}(E_F) - 1 \simeq 0^+$ the Stoner criterion is fulfilled but the spontaneous magnetisation is small, the compound is called *very weak itinerant ferromagnet*
- $I_S \mathcal{N}(E_F) > 1$ we have two possibilities:
  - two subbands with opposite spins are not filled, the compound is a *weak ferromagnet* (the case of Fe metal)
  - the subband with lower energy is completely full, the compound is a *strong ferromagnet* (the case of Co and Ni metal)

2.1.3 Itinerant electron metamagnetism

A magnetic transition from a low to a high magnetisation state in an external magnetic field in a compound is called a metamagnetic transition. It was predicted [17] that in paramagnetic metals with suitable dependence of the density of states around the Fermi level, a first order field induced phase transition from a paramagnetic to a ferromagnetic state can occur. The reason is ascribed to the Fermi level lying on a strong positive curvature of the density of states of these compounds where the Stoner criterion is almost fulfilled, thus the ferromagnetic state can be induced by the external magnetic field and the phenomenon is called itinerant electron metamagnetism (IEMM).

This phenomenon has been observed in various Co-containing compounds as $Co(S,Se)_2$ pyrites or RCo_2 (R=Y, Lu, Sc) Laves phases (see e.g. [18], [19] and references therein) where the 3d electrons are responsible for magnetic properties and the first order field induced phase transition from paramagnetic to ferromagnetic state was observed. The main characteristics of these phenomena are an exchange enhanced susceptibility with a broad maximum around the characteristic temperature T_{max}, a large high field susceptibility even in magnetic fields above the metamagnetic transition, proportionality at low temperatures between critical field B_c and T^2 and the sensitivity to pressure and alloying.

This type of behaviour was also observed in the 5f itinerant electron metamagnet UCoAl, however significant differences are observed:

- the 5f electrons of U mainly contribute to the magnetism, the 3d electrons of Co do not [20]
- the metamagnetic phenomena are not isotropic, contrary to the 3d itinerant metamagnets

– there is no (or was not found yet) clear correlation between B_c and T_{max} as was observed for 3d itinerant metamagnets [21]

Wohlfarth-Rhodes-Shimizu (WRS) theory for the IEMM [17], [22]

Existence of the IEMM can be understood with help of the Landau expansion in the case of very weak itinerant ferromagnetism or exchange enhanced paramagnetism. Under this assumption, the magnetisation is small enough and the molecular field approximation can be applied. Using the Landau expansion of the magnetic free energy in the magnetisation M

$$\Delta F_m(M) = \frac{1}{2}a_0M^2 + \frac{1}{4}b_0M^4 + \frac{1}{6}c_0M^6 \tag{2.5}$$

$$H = \frac{\mathrm{d}\Delta F_m(M)}{\mathrm{d}M} = a_0M + b_0M^3 + c_0M^5 \tag{2.6}$$

we can find the difference between the free energy of the ferromagnetic and paramagnetic state. The coefficients a_0, b_0 and c_0 can be estimated for actual materials [23], [24]. The application of this phenomenological description and the meaning of the expansion coefficient in the case of presence of magnetic fluctuations is discussed in i.e. [25], [26] and will be reviewed later.
We can discuss parameters a_0, b_0, c_0 from 2.5 in context of IEMM:[5]

– When the parameters a_0 and c_0 are positive, b_0 negative and

$$\frac{9}{20} < \frac{a_0c_0}{b_0^2} ,$$

the compound is paramagnetic. The minimum of F_m lies at zero value of magnetisation when $H = 0$ and $M(H)$ increases monotonously with increasing H.

– The parameter a_0 is approximately zero but still positive as well as c_0, b_0 are negative and

$$\frac{3}{16} < \frac{a_0c_0}{b_0^2} < \frac{9}{20} .$$

Without external magnetic field, this set of parameters leads to the formation of the first minimum at $M \neq 0$, but the energy of this minimum is still larger than the energy at $M = 0$ (see Fig 2.2), and the system becomes unstable. With applying a magnetic field the function $M(H)$ given by 2.6 becomes triple valued for $H_1 < H < H_2$ hence hysteresis in the magnetisation curve is observed. With an applied field H_1, the minimum corresponding to the energy minimum appears at M_1 – see the left part of Fig 2.2. The $F_m(M)$ dependence is changing with increasing the magnetic field, and at the field H_2 (larger than the critical field H_c), the second minimum at M_2 becomes lower in energy than the first one. A first order field-induced transition (collective/itinerant electron metamagnetism) from the low to the high magnetisation state occurs.

[5] See the illustration of the dependence of the free energy on these parameters in Fig 2.2.

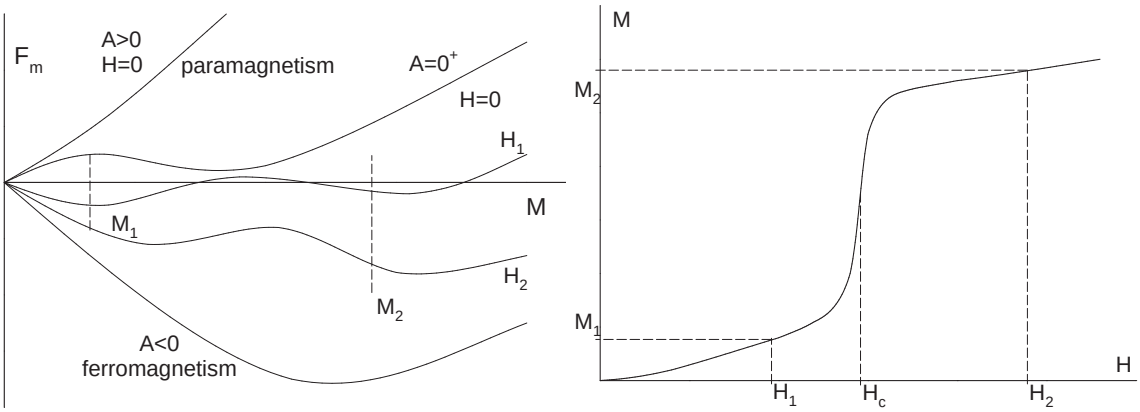

Figure 2.2: Parameters and magnetic states in expansion for magnetic free energy. On the left the $M(H)$ dependence is depicted in the case when the condition for IEMM is fulfilled.

– The parameters a_0 and c_0 are positive, b_0 negative and

$$\frac{a_0 c_0}{b_0^2} < \frac{3}{16} \ .$$

Then the ferromagnetic state is the most stable even in zero external magnetic field.

– The parameter a_0 is negative, the Stoner criterion is well fulfilled, the compound has a spontaneous magnetisation and it is ferromagnetic.

In the Stoner model, the temperature dependence of a_0, b_0 and c_0 in 2.5 come from the Fermi distribution function involved in their expressions [27]. However, this dependence is weak due to the high effective degenerate temperature in the Fermi distribution temperature. On the other hand, spin fluctuations which are not taken into account in the WRS theory play an important role at finite temperatures.

Spin fluctuation enhancement of WRS model [25]

A theoretical approach employing the concept of spin fluctuations (due to its important role at finite temperatures) in order to explain the phenomena of IEEM have been proposed and the magnetic behaviour of $Y(Co_{1-x}Al_x)_2$ and $Co(S_{1-x}Se_x)_2$ was explained in the framework of theory of itinerant electron metamagnetism at finite temperatures ([18], [19] and references therein).

In this approach the temperature dependence of the expansion coefficients in 2.5 is no longer neglected. The renormalisation of a_0, b_0 and c_0 due to the presence of spin fluctuation at finite temperatures leads to the magnetic equation of state[6]

$$\Delta F_{\mathrm{m}}(M) = \frac{1}{2}A(T)M^2 + \frac{1}{4}B(T)M^4 + \frac{1}{6}C(T)M^6 \qquad (2.7)$$

[6]Free energy density is written in the Landau–Ginzburg theory as

$$\Delta f(\mathbf{r}) = \frac{1}{2}a|m(\mathbf{r})|^2 + \frac{1}{4}b|m(\mathbf{r})|^4 + \frac{1}{6}c|m(\mathbf{r})|^6 + \frac{1}{2}D|\nabla \cdot m(\mathbf{r})|^2$$

with coefficients

$$\begin{aligned} A(M) &= a_0 + b_0\left(3\left\langle|\delta m_\parallel|^2\right\rangle + 2\left\langle|\delta m_\perp|^2\right\rangle\right) + \\ &\quad + c_0\left(15\left\langle|\delta m_\parallel|^2\right\rangle^2 + 12\left\langle|\delta m_\parallel|^2\right\rangle\left\langle|\delta m_\perp|^2\right\rangle + 8\left\langle|\delta m_\perp|^2\right\rangle^2\right) \\ B(M) &= b_0 + 2c_0\left(5\left\langle|\delta m_\parallel|^2\right\rangle + 2\left\langle|\delta m_\perp|^2\right\rangle\right) \\ C(M) &= c_0 \end{aligned} \tag{2.8}$$

and

$$\begin{aligned} \left\langle|\delta m_i|^2\right\rangle &= \frac{1}{V}\sum_{\mathbf{q}}\left\langle|m_i(\mathbf{q})|^2\right\rangle \\ \left\langle|m_\parallel(\mathbf{q})|^2\right\rangle &= \left\langle|m_z(\mathbf{q})|^2\right\rangle \\ \left\langle|m_\perp(\mathbf{q}))|^2\right\rangle &= \left\langle|m_x(\mathbf{q})|^2\right\rangle = \left\langle|m_y(\mathbf{q})|^2\right\rangle \ . \end{aligned}$$

The explicit temperature dependence of $\langle|\delta m_i|^2\rangle$ may be obtained [25] in the form of a power series in M

$$\left\langle|\delta m_i|^2\right\rangle = \frac{1}{3}\xi^2(T) + \alpha_i(T)M^2 + \beta_i(T)M^4,$$

where $\xi^2(T)$ denotes the square of the amplitude of fluctuating moment at $M = 0$. The resulting temperature dependence of $A(T)$ and $B(T)$ and its influence on the Arrott plot [25] is sketched in Figure 2.3.[7]

Taking into account that $\chi = \frac{\partial M(T)}{\partial H}$, we may estimate the inverse susceptibility within the framework of this model from 2.7 as

$$\chi^{-1}(T) = A(T)$$

where $A(T)$ is given by 2.8. In order to have a minimum in the $\chi^{-1}(T)$ dependence, the condition

$$\frac{\mathrm{d}\chi^{-1}(T)}{\mathrm{d}T} = \frac{\mathrm{d}A(T)}{\mathrm{d}T} = 0$$

has to be fulfilled and the straightforward derivation leads to the condition on $\xi(T_{\max})$ which we can put in 2.8 and obtain the value of inverse susceptibility at $T_{\max}$

$$\chi^{-1}(T_{\max}) = a_0 - \frac{5}{28}\frac{b_0^2}{c}\ . \tag{2.9}$$

---

where the components of the magnetisation density are given by Fourier transformation

$$m_i(\mathbf{r}) = M\delta_{iz} + \frac{1}{\sqrt{V}}\sum_{\mathbf{q}} m_i(\mathbf{q})\mathrm{e}^{\mathrm{i}\mathbf{q}\mathbf{r}}$$

and the total free energy is obtained by integration in the form

$$\Delta F(M, \left\langle|m_x(\mathbf{q})|^2\right\rangle, \left\langle|m_y(\mathbf{q})|^2\right\rangle, \left\langle|m_z(\mathbf{q})|^2\right\rangle)\ ,$$

where $\langle\bullet\rangle$ denotes thermal average [25].

[7] Arrott plot [28], [29] is in fact graphical representation of the expansion 2.6 finished by third order term.

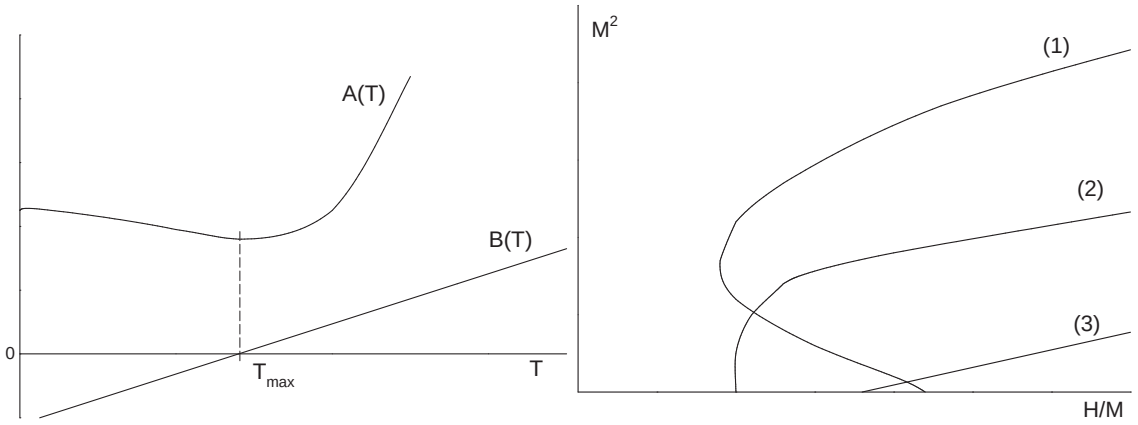

Figure 2.3: The temperature dependencies of $A(T)$, $B(T)$ and Arrott plots in the presence of IEMM [25]. Curves (1), (2) and (3) correspond to $T < T_{\max}$, $T = T_{\max}$ and $T > T_{\max}$.

If we assume strong anisotropy of spin fluctuations as in UCoAl [30], [31], i.e. $\langle|\delta m_{\parallel}|^2\rangle \gg \langle|\delta m_{\perp}|^2\rangle$ we can directly differentiate 2.8 with respect to temperature and obtain the result

$$\chi^{-1}(T_{\max}) = a_0 - \frac{3}{20}\frac{b_0^2}{c} \,. \tag{2.10}$$

2.2 Exchange interactions

The origin of the ordering of magnetic moments is in the exchange interactions. As a prototype an interaction that correlates spins in hydrogen molecule can be taken. These electrostatical interactions lead to a splitting of the energies of the symmetric and antisymmetric orbital and spin ($\uparrow\uparrow$, $\uparrow\downarrow$) states.

In Fig. 2.4, there are schematically reviewed three basic types of exchange interactions. If the magnetic atoms are nearest neighbours (so that the overlap of relevant d or f orbitals is sufficient) the direct exchange can be effective. The best examples of direct exchange can be found in the ferromagnetic 3d metals Fe, Co and Ni.

In alloys and compounds, there are ions carrying magnetic moments frequently separated by other atoms, which can yield various types of indirect exchange interactions. The indirect exchange (super exchange) is typical for materials in which

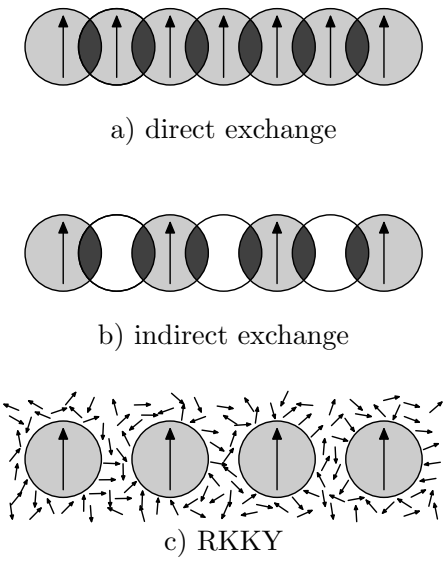

a) direct exchange

b) indirect exchange

c) RKKY

Figure 2.4: Basic types of exchange interactions (after [1]).

the magnetic atoms are surrounded by ligands that do not carry permanent magnetic moments. This interaction is specific for numerous intermetallics although it was introduced to describe a situation in magnetic oxides.

The weak interaction between two magnetic atoms which is mediated by the conduction electrons polarised in the vicinity of magnetic ion (Fig. 2.4 c) is described by RKKY[8] model. This interaction plays an important role in the intermetallic compounds, in particular when the direct and indirect interaction is absent.

Generally, the exchange interaction energy between two magnetic ions can be described as[9]

$$\mathcal{H}_{ij}^{\mathrm{ex}} = -2\mathbf{J}_{ij}\boldsymbol{\mathcal{S}}_i\boldsymbol{\mathcal{S}}_j \ , \tag{2.11}$$

where $\mathbf{J}_{ij}$ is the exchange integral ($10^2 - 10^3$ K for the direct exchange in 3d metals, $10^0 - 10^2$ K for the indirect exchange), and $\boldsymbol{\mathcal{S}}_k$ is spin operator belonging to the k^{th} atom. The exchange energy contribution from the whole system can be obtained by summation of 2.11 through all pairs in system

$$\mathcal{H}^{\mathrm{ex}} = -\sum_{i\neq j}\mathbf{J}_{ij}\boldsymbol{\mathcal{S}}_i\boldsymbol{\mathcal{S}}_j \ .$$

This can be rewritten in the term of molecular (mean, Weiss [3]) field H_{m}

$$\begin{aligned}\mathcal{H}^{\mathrm{ex}} &= -\sum_{i\neq j}\mathbf{J}_{ij}\boldsymbol{\mathcal{S}}_i\boldsymbol{\mathcal{S}}_j = -\sum_i \underbrace{g_i\mu_{\mathrm{B}}\boldsymbol{\mathcal{S}}_i}_{\mu_i}\sum_{i\neq j}\underbrace{\frac{\mathbf{J}_{ij}}{g_ig_j\mu_{\mathrm{B}}^2}}_{V_{ij}}\underbrace{\mu_{\mathrm{B}}g_j\boldsymbol{\mathcal{S}}_j}_{\mu_j} = \\ &= -\sum_i \mu_i\sum_{i\neq j}V_{ij}\mu_j = -\sum_i \mu_i H_{\mathrm{m}} \ .\end{aligned}$$

2.2.1 Magnetic interactions in rare earth transition metal compounds

Generally, magnetic interactions in rare earth (R) transition metal (T) compounds are interesting as the rare earth ion (forming a R sublattice) by rule carry well-defined localised 4f-electron magnetic moment, while transition metal d electron states (in the T sublattice) form an energy band, which gives rise to the d-electron magnetic moments in some cases.

Provided the transition metal sublattice bear stable d-electron magnetic moments the direct d-d interaction is the strongest component. In case of unstable d-electron moments, the strongest component in the system is the 4f-d (R-T) interaction. This interaction usually governs magnetic and transport properties of

[8] Named after Ruderman, Kittel, Kasuya and Yosida who have developed a relevant model ([32], [33] and [34]).

[9] In the case of lanthanides and actinides, we use expression $\mathcal{H}_{ij}^{\mathrm{ex}} = -2\mathbf{J}_{ij}(g_{\mathcal{J}}-1)^2\boldsymbol{\mathcal{J}}_i\boldsymbol{\mathcal{J}}_j$ where $g_{\mathcal{J}}$ is Landé factor

$$g_{\mathcal{J}} = 1 + \frac{J(J+1)+S(S+1)-L(L+1)}{2J(J+1)}$$

and $\boldsymbol{\mathcal{J}}_k$ is total momentum of k^{th} ion.

these compounds. Since the 4f shell is deeply embedded inside of the rare earth ion, the interaction between the R-R nearest neighbours is in principle indirect and is mediated by the 5d and 6s electrons of the R atom.

Another important interaction of the RKKY type which is weakest in the hierarchy of interactions but has a long range character and frequently reflects itself in complex long-period magnetic structures.

For simplification, the basic theory behind these main interactions is discussed in the next sections on the example of the 4f–3d (RE–T) system, however, it is valid generally.

4f–4f interaction (RKKY model)

The RKKY model describes the component of the 4f–4f interaction mediated by conduction electrons[10]. It's usually described in the way that 4f moment localised on the ion i interacts with conduction electrons, leading to their spin polarisation. The spin polarised electrons interacts with another 4f spin localised on the ion j and therefore creates an indirect interaction between the 4f spins $\mathbf{S}_i$ and $\mathbf{S}_j$.

d-d (T-T) interaction (basics of the band theory)

The 3d band calculations are well treated in the Hartree-Fock approximation based on the assumption that each electron is placed in the electrostatic potential of a metal which is taken as a sum of atomic potentials V_i centring on the various lattice sites $i \Rightarrow V \approx \sum V_i$. Therefore the Hamiltonian describing the interaction of the d-electrons in the metal environment can be written as $\mathcal{H} = T + \sum V_i$, where the former term is the kinetic energy of an electron and the second one is the electrostatical potential of metal. This problem is solved by means of LCAO[11] method, where the wave functions $|\Psi\rangle$ are taken as linear combinations of atomic orbitals $|\Psi\rangle = \sum a_{im}|im\rangle$, where constant a_{im} fulfills the orthonormality condition $\sum |a_{im}|^2 = 1$ and m is the projection of the angular moment. The energy of the d band can be determined as

$$\left(T + \sum V_i\right)\left|\Psi\right\rangle = E|\Psi\rangle$$

and the energy change from the atomic state to the metal is calculated as

$$\begin{aligned} E &= \sum_{im} |a_{im}|^2 \alpha_{im} + \sum_{ijmm'} a^*_{im} a_{jm'} \beta_{ijmm'} \ , \\ \alpha_{im} &= \left\langle im \left| \sum V_j \right| im \right\rangle \ , \\ \beta_{ijmm'} &= \langle im \left| V_j \right| jm' \rangle \ . \end{aligned}$$

The atomic states $|im\rangle$ still remain under the influence of $\sum V_i$, thus the α term is only to shift of the energy of atomic levels. In the β term the atom states are

[10] Usually the situation is more complex — the interaction may be also mediated by the 3d itinerant electrons (see below).

[11] **L**inear **C**ombination of **A**tomic **O**rbital [35]

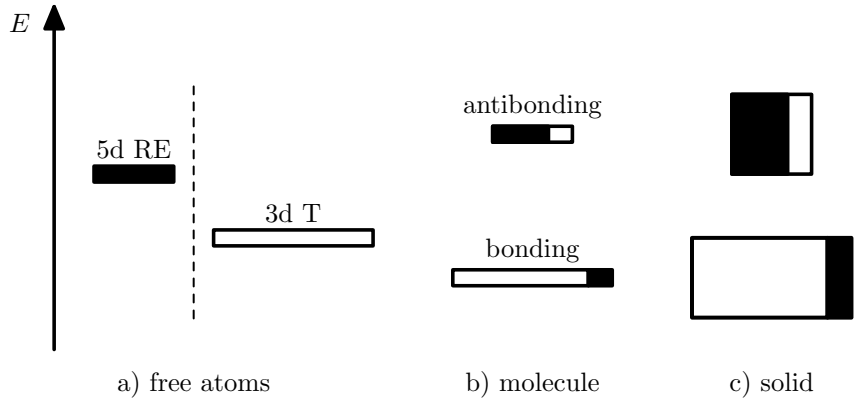

Figure 2.5: Schematic representation of the relative position between the 5d and 3d atomic levels (a), the bonding and antibonding levels for RE–T molecule (b) and illustration of their broadening in a solid (c). The amount of mixing between the original 3d and 5d states is illustrated by the black and white areas. (After [36].)

changed from $|im\rangle$ to $|jm'\rangle$, thus integrals β are called transfer integrals, mixing the atomic states into molecular states extending over the whole crystal.

The character of the 3d band depends strongly on the T–T atomic spacing $d_{\mathrm{T-T}}$; it becomes narrower when increasing the spacing between the atoms.

4f–3d interaction — simple model of electronic structure ($3d_T$—$5d_{RE}$ mixing)

The 3d T–band and 5d RE–band hybridise, yielding to bonding — antibonding band structure[12] (analogue to bonding — antibonding levels in RE–T molecule, see Fig 2.5). In the free atoms, the energy of the T 3d states lies lower then the energy of RE 5d states (see Fig 2.5 a), thus the bonding band will obviously be dominated by 3d states, while the antibonding band has mainly 5d character. The degree of mixing between the 3d and 5d states depends on the overlap matrix element and on the energy separation between the 3d and 5d bands. If this energy separation is increased, the mixing decreases and the opposite holds when the separation is decreased.

Now we introduce the effects due to the 4f states, which retain their atomic character in the solid (and their energy location[13] (relative to the 5d and 3d state energies) is not important). When the 4f electrons remain localised in the core of RE ion, they will influence the magnetic properties of valence electrons through the exchange potential. Since the 4f wave function has a limited extension, this coupling take place essentially within the rare earth ion and mainly with the lanthanide 5d electrons (which have larger density and overlap with the 4f states than have

[12] In reality there is generally no such clear separation in energy between these two parts of electronic structure, but it is used in this model for clarity.

[13] Except some cerium compounds where the energy position of 4f state is located in the gap between bonding and antibonding states.

the 5p or 5s states). The local exchange interactions are positive and the 4f and 5d spins align parallel and the strength of the coupling is clearly dependent upon the number of unpaired 4f spins. By reason that the 5d states are hybridised with the 3d states the 4f spin moments couple indirectly to the 3d spin moments.

If we assume that the 3d electrons spin-polarise, then the energy densities from Fig 2.5 c) are modified as illustrated in Fig 2.6. The energy separation between bonding and antibonding subbands becomes different for the two spin directions, therefore the 3d–5d hybridization is different for majority and minority spins. Therefore now a decrease of the 5d content yields for the majority bonding band. This has the effect that the spin-up (majority) occupation of the 5d part becomes less than the spin-down (minority) occupation of the 5d part. Thus there is a total spin-down 5d moment on the rare earth atom.

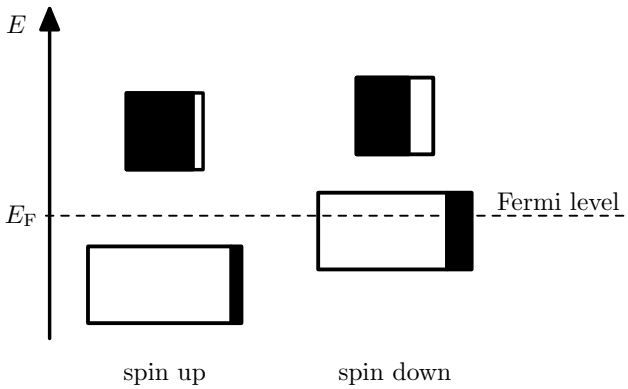

Figure 2.6: Spin-up (majority) and spin-down (minority) densities of states for a saturated ferromagnetic state. The amount of hybridisation between 3d and 5d states becomes different for the two spin directions (illustrated by the black and white areas).(After [36].)

2.3 Magnetism in U intermetallics

In this section we discuss main features (detailed information can be found in specific reviews, e.g. [37] — the key reference considered in Chapter 2.3) of the uranium ordering mechanisms and highlight main differences in comparison with 'elementary' ordering schemes discussed earlier in this chapter and summarised in the next paragraph.
As mentioned earlier, there exists two major types of magnetism in intermetallic compounds:

- Stoner magnetism, connected with the polarisation of the density of states at Fermi energy, typical for transition metals.
- Localised magnetism, characterised by strong localisation and weak interaction with environment of 4f states responsible for magnetism. Due to the negligible mixing between 4f states and conduction and other electron states the observed magnitude of ground state magnetic moment usually well agree with the R^{3+} free ion value calculated within LS coupling scheme.[14] As a result of the interaction between the aspherical 4f charge and the surrounding

[14]Partial discrepancies may be observed due to the lifting of orbital degeneracy of 4f states by the crystalline electric field.

charge distribution the single ion magnetocrystalline anisotropy of 4f magnetic moments is observed.

Generally, the actinides can be taken as a transition between these two extremes with early actinides having the itinerant 5f electrons and heavier having localised 5f electrons.

2.3.1 Uranium 5f states

The uranium 5f-electron wave functions are much more spatially extended than the 4f states in lanthanides leading to more stronger interaction between the 5f electrons and metallic surrounding (including the 5f-electrons of the U nearest neighbours). Consequently, 5f electrons are delocalised due to their participation in the bonding states accompanied with considerable hybridisation with valence states of non-U neighbouring atoms in crystal lattice. Furthermore, a more or less narrow 5f band is formed as a consequence of delocalisation and it is intersected by the Fermi energy E_F.[15] The delocalised character of the 5f states which are usually responsible for the magnetic behaviour in the uranium intermetallic compounds has several consequences:

- The magnetic moments are much smaller than expected for the U^{3+} or U^{4+} ions and magnetic moments can disappear in the broad band limit leading to Pauli paramagnetism. This situation is in some sense similar to 3d transition metals.
- The magnetic coupling (in the presence of 5f magnetic moments interacting directly) is typically stronger than in the case of 4f moments in the case of lanthanides.
- The high density of 5f-electron states at E_F is responsible for high γ values of the low temperature specific heat (further influenced by strong electron electron correlations) and for highly anisotropic transport properties (consequence of hybridisation between electrical current carrying non-f states and heavy electrons from 5f states).
- Essentially different mechanism of magnetic anisotropy, which is based on the two ion interaction (5f–5f), is an important consequence.

Hybridisation of uranium 5f states

Generally, two types of mechanisms affecting the uranium 5f states should be considered — direct overlap of 5f wave functions of neighbouring uranium atoms (leading to the formation of the band) and 5f–ligand hybridisation.

In the first case, the most important role is played by the U–U spacing d_{U-U}, uranium compounds with small d_{U-U} are often superconductive whereas those with larger d_{U-U} has often a magnetic ground state [38]. The critical distance (Hill limit) was considered $d_{U-U} \approx 0.35\,\text{nm}$. The occurrence of magnetic ground state

[15] The bandwidth W_{5f} is typically several eV.

is determined by the Stoner type criterion 2.2 (see page 17). From this criterion, it is evident that the component which mostly affects the occurrence of magnetism is the width of the 5f band W_{5f}.[16] This bandwidth is strongly sensitive to the interatomic distance R following expression $W_{5f}/W_{5f,0} \sim (R_0/R)^x$, where $x \approx 6$ is reported [39], explaining prominent sensitivity of uranium compounds to pressure and alloying. However, this simple rule neglecting details of the density of states and possible ligand hybridisation has several exceptions with magnetic order despite having d_{U-U} well below Hill limit (e.g. UNi_2 [40]) or on the other hand non-magnetic compounds with d_{U-U} well above Hill limit (e.g. URh_3 [41]).

The large number of non-magnetic exceptions with d_{U-U} above Hill limit is caused by the strong hybridisation between 5f electrons and ligand valence states. In the case of strong hybridisation this mechanism can dominate and leads to a non-magnetic ground states in the compounds with a negligible 5f-5f overlap [41]. In the case of neighbouring uranium and p-metal (e.g. UX_3 compounds), the most important parameter is the size of the p-element; smaller ions leads to large overlap integrals (non-magnetic ground state) whereas large ions reduce the hybridisation (magnetic ground state). In the uranium compounds with a transition metal the filling of the transition metal d states is the main parameter governing the hybridisation strength. With gradual increasing of the electronegativity (moving from the left to the right in the transition metal series) the d-band is moved further below the Fermi level, reducing the energy overlap between the uranium 5f states and transition metal d states and consequently the 5f-d hybridisation is weakening. Therefore, the magnetism in this type of compounds is typically observed with transition metals from the right part of a particular series. In these compounds the magnetic moments on the transition metal (if observed) are greatly suppressed due to the delocalisation of d electrons.

Uranium magnetic moments

As mentioned above, the 5f-band model is an appropriate description for the majority of uranium intermetallics, therefore the appearance of U magnetic moments and their ordering can rather be understood as a result of a spontaneous splitting of the spin up and spin down subbands leading to a net spin magnetic moment μ_S. However, there is an important difference between the 3d transition metal and uranium — the energy of the spin orbit coupling E_{so} is much smaller as compared to the energy width of the 3d band in the case of transition metals, however it compares to the energy width of the 5f band in the uranium case. Due to the strong spin orbit interaction, usually a large orbital moment μ_L is induced in the 5f electron system and oriented antiparallel to the spin moment [42]. Based on the calculations, it was predicted [42] that the spin and orbital moments have different sensitivities to applied pressure leading to the assumption that the level of degree of 5f delocalisation should be reflected in the spin to orbital moment ratio. This was later acknowledged by numerous experimental results, however, with exceptions.

[16] The number of 5f electrons in uranium compounds is fixed between 2–3 and exchange integral doesn't significantly vary in similar materials.

Exchange interactions and magnetocrystalline anisotropy

If we compare magnetic ordering temperatures of uranium compounds and their lanthanide analogs,[17] we immediately see significant differences. As implied from facts mentioned earlier, the typical interaction in lanthanide compounds is the indirect interaction (typically mediated by conduction electrons) whereas in the uranium compounds the direct interaction between 5f states may occur, possibly leading to significantly higher ordering temperatures despite (typically) lower magnetic moments.
Depending on the d_{U-U} distance, two main regimes can be observed:

- In the uranium rich compounds (d_{U-U} below or nearby Hill limit) the direct 5f-5f overlap leads to direct exchange coupling. Uranium moments in compounds exhibiting magnetic ordering have magnitude well below $1\,\mu_B$, ordering temperatures are relatively high and only ferromagnetism is observed in this type of compounds.
- For d_{U-U} above Hill limit the antiferromagnetism appears and above $d_{U-U} > 0.4\,\text{nm}$ no ferromagnetic compound is reported. Above this limit (0.4 nm) the 5f–5f overlap is negligible and hybridisation plays important role in the indirect exchange coupling.[18]

If the ion–ion interaction is mediated by different covalent bonding channels, the stronger interaction is for those pointing along the ion–ion bonding axis (representing quantisation axis). Two 5f ions maximise their interaction by compression of the 5f charge in the direction to the nearest 5f ion [43]. The resulting orbital moment perpendicular to the bonding direction has an impact on the magnetic anisotropy, leading to strong ferromagnetic coupling of uranium atoms along the bonding direction (leaving no special tendency for perpendicular direction). This two ion anisotropy, which can be observed only in a system with an unquenched orbital moment, leads to a uniaxial anisotropy in systems with uranium atoms organised in planes (i.e. with short d_{U-U} distancies in a plane and larger interplanar spacings) or a planar type of anisotropy in the case of bonding uranium chains. This anisotropy is observed both in ordered and paramagnetic state and its strength can be estimated from differences in the paramagnetic Curie temperatures obtained from measurements of the magnetic susceptibility with a field applied along different crystallographic directions (typical values are $10^2 - 10^3\,\text{T}$).

[17] with the same crystallographic structure and with magnetism only on uranium (or lanthanide) sites

[18] Therefore, the hybridisation plays dual role in the uranium moments ordering mechanisms — primarily it destabilises the 5f moments (due to the band formation) and secondary it participates on the exchange coupling. Consequently, the maximum ordering temperatures are expected in the compounds with moderate hybridisation — the magnetic moments are not suppressed and well coupled.

2.4 Basic theory behind magnetoelastic phenomena

The dimensional changes are caused by the free energy minimisation, which has contributions coming from the static lattice, lattice vibrations, itinerant electrons, electric dipoles, magnetic ions, nuclear spins, etc. Magnetoelastic effects are therefore closely related to the interaction between the lattice and electron degrees of freedom, playing fundamental importance in magnetism and superconductivity. The study of the magnetoelastic effect is not only restricted to the basic research, there are direct industrial application connected to the application of magnetostrictive effects in ferromagnetic materials (see e.g. [44]).

In this section, the theory behind the magnetoelastic phenomena is briefly discussed, mainly in connection with the general description of phenomena and arguments necessary for the results discussion. For detailed description of a theory and theoretical models of magnetostriction see some of the numerous overviews (e.g. [45], [46]) or monographs (e.g. [47]).

2.4.1 General thermodynamic theory

Important property of material is the variation of a geometrical parameter describing the change of the dimensions and lattice structure, connected to a change in magnetic structure due to the variation of the magnetic field or temperature. Mostly, the coefficient of volume expansion

$$\alpha^V = \left(\frac{\partial \ln V}{\partial T}\right)_p \tag{2.12}$$

is discussed and is obtained (for cubic and isotropic solids) from the coefficient of linear thermal expansion α by

$$\alpha^V \approx 3\alpha = 3\left(\frac{\partial \ln l}{\partial T}\right)_p .$$

More generally the coefficient of linear thermal expansion is defined by the temperature variation of macroscopic strain parameters of anisotropic solids[19]

$$\alpha_{ij} = \left(\frac{\partial \varepsilon_{ij}}{\partial T}\right)_p . \tag{2.13}$$

[19]The strain tensor (more precisely Lagrange finite strain coordinate) $\mathfrak{e}$ is defined as

$$\varepsilon_{ij} = \frac{1}{2}\left(\frac{\partial u_i}{\partial x_j} + \frac{\partial u_j}{\partial x_i}\right)$$

where $\mathbf{u}$ is the displacement vector and describes the deformation of the solid body relatively to the reference configuration.

The volume expansion defined by 2.12 is simply related to the derivatives of the Gibbs free energy $G(P,T)$

$$\alpha^V = \left(\frac{\partial \ln V}{\partial T}\right)_p = \frac{1}{V}\frac{\partial^2 G}{\partial p \partial T}$$

or alternatively to the Helmoltz free energy

$$\alpha^V = -\left(\frac{\partial \ln V}{\partial p}\right)_T \left(\frac{\partial p}{\partial T}\right)_V = -\kappa_T \frac{\partial^2 F}{\partial V \partial T} = \kappa_T \left(\frac{\partial S}{\partial V}\right)_T \tag{2.14}$$

where $\kappa_T = -\left(\partial \ln V/\partial p\right)_T$ is the isothermal compressibility and S is the entropy.[20] The Eq. 2.14 binds the volume entropy change with the isothermal compressibility and the volume change, whereas temperature entropy change is connected with the specific heat at constant volume $C_V = -T\left(\partial S/\partial T\right)_V$. This leads to the definition of the thermodynamic Grüneisen function γ_{G} based on the differential change in entropy

$$\begin{aligned} \mathrm{d}S &= \left(\frac{\partial S}{\partial T}\right)_V \mathrm{d}T + \left(\frac{\partial S}{\partial V}\right)_T \mathrm{d}V \\ &= C_V \mathrm{d}\ln T + \frac{\alpha^V V}{\kappa_T}\mathrm{d}\ln V, \end{aligned}$$

in the case of constant entropy

$$\gamma_{\mathrm{G}}(T,V) \equiv -\left(\frac{\partial \ln T}{\partial \ln V}\right)_S = \frac{\alpha^V V}{\kappa_T C_V}\ .$$

The Grüneisen function is useful in the analysis of thermal expansion data and its interpretation. It connects the two strongly temperature dependent quantities α^V and C_V but is itself relatively weakly dependent on the temperature. The experimental values are usually derived from a combination of several measure quantities (expression obtained by thermodynamic transformations)

$$\gamma_{\mathrm{G}}(T,V) = \frac{\alpha^V V}{\kappa_T C_V} = \frac{\alpha^V V}{\kappa_S C_p}$$

where κ_S is the adiabatic compressibility and C_p is the heat capacity at constant pressure.

The entropy (or related the Helmholtz free energy) may be written as a sum of individual components (typically ionic lattice, conduction electrons and contribution from magnetic subsystem)[21]

$$S = \sum S_r$$

[20] The reciprocal of κ_T, the isothermal bulk modulus $B_T = -\left(\partial p/\partial \ln V\right)_T$ is often used in this description.

[21] Validity of this separation is guarantied when the relaxation times for components are sufficiently different.

leading to the formula analogic to the Matthiessen's rule 3.5

$$\alpha^V = \kappa_T \left(\frac{\partial S}{\partial V}\right)_T = \kappa_T \sum \left(\frac{\partial S_r}{\partial V}\right)_T = \sum \alpha_r^V \ .$$

Consequently, the magnitudes of the α_r^V depends on the sensitivity of the entropy contributions S_r to changes of volume, or more generally to the strain. The separation of individual contributions is based on their known temperature dependencies, e.g. at low temperatures the lattice vibration contribution varies as T^3 (Debye model), whereas the electronic and some magnetic contribution vary as T.

2.4.2 Magnetostriction in the standard model of rare earth magnetism

The following short review of basic features of theoretical model is presented under the assumption that magnetoelastic energy is smaller in comparison to the exchange energy and with neglecting the dynamical coupling between lattice and crystal field or exchange[22]. In the model, the crystal field and bilinear two ion interaction $\mathcal{J}_i \mathbf{J}(ij) \mathcal{J}_j$ between rare earth angular momenta on the i and j sites are considered. Then the Hamiltonian consists of the crystal field, two ion exchange and Zeeman contribution[23]

$$\begin{aligned} \mathcal{H} &= \mathcal{H}_{\mathrm{cf}} + \mathcal{H}_{\mathrm{ex}} + \mathcal{H}_{\mathrm{Z}} \\ \mathcal{H}_{\mathrm{cf}} &= \sum_{ilm} B_l^m(i) O_l^m(\mathcal{J}_i) \\ \mathcal{H}_{\mathrm{ex}} &= -\frac{1}{2} \sum_{ij} \mathcal{J}_i \mathbf{J}(ij) \mathcal{J}_j \\ \mathcal{H}_{\mathrm{Z}} &= -\sum_i g_{\mathcal{J}}\, \mu_{\mathrm{B}} \mathcal{J}_i \mathbf{H} \ . \end{aligned} \tag{2.15}$$

Starting point for further advanced analysis is based on the Taylor expansion of the crystal field $B_l^m(i, \mathfrak{e})$ and magnetic exchange $\mathbf{J}(ij, \mathfrak{e})$ parameters with respect

[22] i.e. neglecting crystal field — phonon and magnon — phonon interaction

[23] Typically, two types of the two ion interaction may be present in rare earth intermetallic compounds (see Section. 2.2), the dipolar interaction

$$\mathbf{J}_{\alpha\beta}^{\mathrm{DD}}(ij) \propto \frac{3R_{ij}^{\alpha} R_{ij}^{\beta} - \delta^{\alpha\beta} \|\mathbf{R}_{ij}\|^2}{\|\mathbf{R}_{ij}\|^5}$$

and RKKY interaction (k_{F} denotes the radius of the conduction electron Fermi surface)

$$\mathbf{J}_{\alpha\beta}^{\mathrm{RKKY}}(ij) \propto \delta^{\alpha\beta} \frac{2k_{\mathrm{F}}\|\mathbf{R}_{ij}\| \cos(2k_{\mathrm{F}}\|\mathbf{R}_{ij}\|) - \sin(2k_{\mathrm{F}}\|\mathbf{R}_{ij}\|)}{\|\mathbf{R}_{ij}\|^4} \ .$$

to the components of the strain tensor leading to the magnetoelastic Hamiltonian

$$\sum_{ilm} B_l^m(i,\varepsilon)O_l^m(\mathfrak{J}_i) \approx \sum_{ilm} B_l^m(i,\varepsilon=0)O_l^m(\mathfrak{J}_i) + \sum_{ilm} \varepsilon^\alpha B_{l,(\alpha)}^m(i,\varepsilon)O_l^m(\mathfrak{J}_i) + \cdots$$
$$\sum_{ij} \mathfrak{J}_i \mathbf{J}(ij,\varepsilon)\mathfrak{J}_j \approx \sum_{ij} \mathfrak{J}_i \mathbf{J}(ij,\varepsilon=0)\mathfrak{J}_j + \sum_{ij} \varepsilon^\alpha \mathfrak{J}_i \mathbf{J}_{(\alpha)}(ij,\varepsilon)\mathfrak{J}_j + \cdots$$

with magnetoelastic constants

$$B_{l,(\alpha)}^m(i,\varepsilon) = \left(\frac{\partial B_l^m(i,\varepsilon)}{\partial \varepsilon^\alpha}\right)_{\varepsilon=0}$$
$$\mathbf{J}_{(\alpha)}(ij,\varepsilon) = \left(\frac{\partial \mathfrak{J}(ij,\varepsilon)}{\partial \varepsilon^\alpha}\right)_{\varepsilon=0}.$$

Usually only harmonic approximation (expansion up to first order in strain) is used and anharmonic coupling is neglected.

Based on the Hamiltonian 2.15 and calculation of the magnetic free energy F_m and corresponding derivatives, the crystal field and exchange strains may be calculated [45]

$$\varepsilon_\mathrm{cf}^\alpha = -\frac{1}{V}\sum_{ilm\beta} s^{\alpha\beta} B_{l(\beta)}^m(i)\langle O_l^m(\mathfrak{J}_i)\rangle_{T,\,\mathbf{H}}$$
$$\varepsilon_\mathrm{ex}^\alpha = \frac{1}{2V}\sum_{ij\beta} s^{\alpha\beta}\langle \mathfrak{J}_i \mathbf{J}_{(\beta)}(ij)\mathfrak{J}_j\rangle_{T,\,\mathbf{H}}$$

where $\langle\bullet\rangle_{T,\,\mathbf{H}}$ denotes the thermal expectation values and $s^{\alpha\beta}$ denotes elastic compliances ($\mathbf{s}\cdot\mathbf{c}=\mathbf{1}$, $\mathbf{c}$ is elastic constant tensor).

2.4.3 Magnetostriction in itinerant electron systems

The above mentioned formulas are well applicable for the localised systems. In the case of itinerant electron systems a simple formula can be derived [11] characterising the magnetovolume effect, derived from Stoner model

$$\frac{\Delta V}{V} = \frac{V\kappa_T}{2D\,{\mu_\mathrm{B}}^2}\frac{\partial \ln D}{\partial \ln V}M^2 \tag{2.16}$$

where D denotes the electron density of states at the Fermi energy and M is magnetisation density, respectively. The proportionality term is called the magnetoelastic coupling coefficient.[24] Because the density of states usually increase with increasing volume ($\partial \ln D/\partial \ln V$) the magnetically induced volume increase is expected.

[24] If the isothermal compressibility is known, than the term

$$\frac{V}{2D\,{\mu_\mathrm{B}}^2}\frac{\partial \ln D}{\partial \ln V}$$

is called magnetoelastic coupling constant.

Chapter 3

Experimental methods

This chapter is devoted to a short overview of experimental methods used in this thesis, theirs theoretical background and basic formulas important for the data evaluation. In the case of sections 3.5 and 3.6, the discussion is more detailed due to their importance in this thesis and their improvement.

3.1 Sample preparation and characterisation

In this thesis only single crystal samples were studied, allowing observation of reflection of material anisotropy on the anisotropy of measured properties. This is very important in the rare earth compounds, where the significant anisotropy is observed and studies on polycrystalline samples cannot give satisfactory information due to the overall averaging over all grains. The need for the single crystal samples predominates the rather difficult single crystal preparation arising from the complexities in the phase diagrams of rare earth alloys.

In this context, the melt grown processes are typically used for congruent compounds simplifying the solidification process and yielding good quality single crystals. Good separation of a desired compound from neighbouring phases and high melting point with respect to them increases the probability of obtaining single crystals of good quality and size.

All samples used for this study were previously prepared by arc melting using the modified Czochralski method. Shortly described, in this method the sample is 'pulled' from the melt using an unsolvable tungsten rod or a polycrystalline seed. In order to obtain only one crystalline grain the necking procedure is used, its speed controls the quality and mosaicity of the crystal. After the necking the desired crystal is grown (the detailed description of this technique can be found in [48]). Due to the differences in apparatus and complexity of rare earth – transition metal phase diagrams several trials are usually needed in order to obtain a good quality single crystal and the experience plays an important role.

The obtained crystals were cut in pieces and properly oriented by Laue X-ray diffraction at ambient conditions confirming the good quality of the single crystal.

3.2 Magnetic properties

For measurements of the magnetisation and magnetic susceptibility a commercial PPMS[1] apparatus from Quantum Design (QD, [49]) was used. As common in many of modern instruments the magnetic moment of a sample is measured using an induction technique. The principle of this method is in the measurement of the induced voltage while moving the sample through pickup coils. Generally speaking, the sample can be moved either periodically (vibrating sample magnetometer) or extracted from the coils. The magnetisation is calculated from the proportionality equation between the induced voltage on the pickup coils and the change of the magnetic flux

$$U \approx \frac{\mathrm{d}B}{\mathrm{d}t} \tag{3.1}$$

where B is calculated from the magnetisation and magnetic intensity $B = \mu_0(M + + H)$.

In the PPMS apparatus the housing consisting of the drive and detection coils, thermometer and standard electrical interface is placed inside the PPMS chamber allowing usual field and temperature control. The sample itself is fixed to a long thin rigid rod connected to a DC servo motor outside the sample chamber. This setup allows longitudinal movements through the pick-up coils. The sample translation is synchronised with data acquisition. The magnetic moment is obtained by numerical integration of the measured voltage profile and fitting of the obtained waveform to the known data for a dipole moving through the detection coils. The homogeneity of the magnetic field across the measuring region is 0.01 %.
Samples were carefully fixed in order to avoid possible rotation due to the torsion forces coming from the strong anisotropy in the majority of the studied compounds.

3.3 Thermodynamic properties

3.3.1 Specific heat

The specific heat is thermodynamically defined as

$$C_x = \lim_{\mathrm{d}T \to 0} \left(\frac{\mathrm{d}Q}{\mathrm{d}T} \right)_x$$

where $\mathrm{d}Q$ is a heat input that causes a subsequent temperature rise $\mathrm{d}T$ in the sample. This definition is not very well suited for practical determination of the specific heat. Various approaches are used to determine the specific heat, depending on the sample and its conditions.

Studies of small solid samples are usually performed using the AC method [50], [51] or the thermal relaxation method [52]. A commercial, fully automated relaxation calorimeter (part of PPMS) was used for specific heat measurements reported in this thesis.

[1] **P**hysical **P**roperty **M**easurement **S**ystem

The QD PPMS relaxation calorimeter consists of an alumina platform ($\sim 3 \times 3\,\mathrm{mm}^2$) which is attached by eight wires (weak thermal link) to the heat sink (puck).[2] The thermometer (Cernox, Lakeshore) and heater (RuO thin film) are attached to the back of the platform. A cap on the top of the puck acts as a radiation shield. During the measurement the puck is placed in an evacuated ($p < 10^{-3}\,\mathrm{torr}$) sample chamber. Prior to the sample measurement the heat capacity of an empty puck (and any additional addenda — usually vacuum Apiezon N grease[3] facilitating fixation of a sample and heat transfer between the platform and the sample) has to be measured. During the measurement (with or without sample) the platform is heated to a temperature $T = T_0 + \Delta T$ and then allowed to relax back to T_0. The decay may be described by one or two exponential components (depending on the thermal link between sample and platform), this decay is recorded and fitted by curve fitting procedure [55]. Independent studies confirmed that the precision of measurement is up to 1 % for temperatures above 5 K and 5 % for lower temperatures [56], however, they also showed difficulties with determining of absolute values of the specific heat in the vicinity of a first order transition [57].

3.3.2 Magnetic phase transitions

Generally, phase transitions are transformations of a thermodynamic system from one phase to another accompanied by an abrupt change in one or more physical properties (heat capacity, resistivity, thermal expansion, etc.) with a small change of a thermodynamical variable (typically temperature, pressure, external fields).

Phase transitions may be divided into two broad classes based on the presence of a latent heat associated with the transition.[4] During the first order transition the latent heat is released/absorbed leading to the observation of hysteresis.[5] The second order (continuous) transition has no associated latent heat.

In both cases, the evolution of the phase boundary may be described relating the sensitivity of the transition temperature (or field) to the pressure with the changes of the elastic or thermal properties across the transition. For the first order transitions the Clausius–Clapeyron relation

$$\frac{\mathrm{d}T_\mathrm{c}}{\mathrm{d}p_x} = V_\mathrm{M} \frac{\Delta \left\{ \frac{\Delta l}{l} \right\}_x}{\Delta S} \tag{3.2}$$

derived from the equality of chemical potentials of two phases in equilibrium is valid, putting the proportionality between the pressure change of the transition

[2] This describes the standard puck, there are slight differences in the design of the ^{3}He puck, which was not used in this study.

[3] This grease is used for its good thermal properties, low vapour pressure and because it is inert. However, care must be taken during the data evaluation, because of two anomalies (step at $\sim 215\,\mathrm{K}$ and peak at $\sim 290\,\mathrm{K}$) in the temperature dependence of the specific heat of grease are observed [53]. Also the dependence of the specific heat on the thickness of used grease layer was reported [54].

[4] Formerly the Ehrenfest classification scheme based on the non-analyticality of the free energy derivatives was used. This scheme allows in principle higher order transitions.

[5] Latent heat is typically a large amount of energy (connected with the discontinuity of the entropy across the phase boundary $L = T\Delta S$) which cannot be transferred instantaneously.

temperature and the ratio between the jump in the thermal expansion and in the molar entropy at the transition.

In the case of a continuous entropy change across the transition the Ehrenfest relation can be formulated

$$\frac{\mathrm{d}T_\mathrm{c}}{\mathrm{d}p_x} = V_\mathrm{M} T_\mathrm{c} \frac{\Delta\alpha_x}{\Delta c_p} \tag{3.3}$$

where V_M is the molar volume, $\Delta\alpha_x$ and Δc_p are jumps associated with the transition in the linear thermal expansion coefficient and the molar specific heat respectively. In the case of hydrostatic pressure the evolution of T_c with pressure may be estimated as $\frac{\mathrm{d}T_\mathrm{c}}{\mathrm{d}p} = \sum_x \frac{\mathrm{d}T_\mathrm{c}}{\mathrm{d}p_x}$ i.e. using the $\alpha = \alpha_a + \alpha_b + \alpha_c$ in the 3.2 and 3.3, respectively.

3.4 Transport properties

Transport phenomena include the electrical and thermal resistivity, thermopower, magnetoresistivity and the Hall effect. These are the physical properties of solids dealing with a charge or heat transport under the influence of external forces. This can be in general[6] described as

$$J_i = \sum_{j=1}^{n} L_{ij} X_j \ ,$$

where $\mathbf{J}$ is current (response of the system), $\mathbf{X}$ is a generalised external force and L_{ij} are so-called linear transport coefficients. The simultaneous application of an external magnetic field is a further scenario – the magnetic field does not cause a drift velocity within a conduction system, but it has an influence on the conduction electron trajectories and thus influence the charge current.

The most common approach to describe transport phenomena is the Boltzmann formalism, which is based on an assumption that the distribution function in the phase space $(\mathbf{r}, \mathbf{k})$ can be defined. From this distribution function f we can calculate appropriate current densities [58]. The distribution function is a solution of Boltzmann equation (which describes time development of the distribution function) in the presence of external forces $\mathbf{F}$

$$\frac{\partial f(\gamma, \mathbf{r}, t)}{\partial t} + \frac{1}{\hbar}\mathbf{F} \cdot \nabla_k f(\gamma, \mathbf{r}, t) + \mathbf{v} \cdot \nabla_r f(\gamma, \mathbf{r}, t) = \left(\frac{\partial f(\gamma, \mathbf{r}, t)}{\partial t}\right)_{\text{collision}} , \tag{3.4}$$

where γ is abbreviation for the band quantum numbers n, σ and $\mathbf{k}$ ($\gamma = (n\ \sigma\ \mathbf{k})$) and $\mathbf{v}$ is the velocity of a wave packet. The left hand side of 3.4 describes the time development of the distribution function caused by the semiclassical equations of motion

[6] under the assumption of linearity between the forces $\mathbf{X}$ and currents $\mathbf{J}$

$$\mathbf{v} = \frac{\mathrm{d}\mathbf{r}}{\mathrm{d}t} = \frac{1}{\hbar}\nabla_k E_{n\sigma}(\mathbf{k}) \ ,$$
$$\frac{\mathrm{d}\mathbf{k}}{\mathrm{d}t} = \frac{1}{\hbar}\mathbf{F} \ .$$

The right hand side of 3.4 is the collision term, which takes into account the changes in the distribution function due to scattering processes.

In the presence of a time-independent electric and magnetic field applied to the system of conduction electrons the external force $\mathbf{F}$ is the Lorenz force

$$\mathbf{F} = -e\left(\frac{1}{c}\mathbf{v}\times\mathbf{B} + \mathbf{E}\right) \ .$$

For this time-independent distribution function we are looking for time-independent solution of Boltzmann equation 3.4 for distribution function $f(\gamma, \mathbf{r})$

$$-\frac{e}{\hbar c}\left(\mathbf{v}_\gamma \times \mathbf{B}\right)\cdot\nabla_k f(\gamma,\mathbf{r}) - \frac{e}{\hbar}\mathbf{E}\cdot\nabla_k f(\gamma,\mathbf{r}) + \mathbf{v}_\gamma\cdot\nabla_r f(\gamma,\mathbf{r}) = \left(\frac{\partial f(\gamma,\mathbf{r},t)}{\partial t}\right)_{\text{collision}} \ .$$

Electrical resistivity

Assuming independent scattering mechanisms (right hand side of 3.4), we can apply the so-called *Matthiessen's rule* for description of the resistivity. The resistivity can be then written in general as

$$\varrho_{\text{tot}} = \varrho_0 + \varrho_{\text{ph}} + \varrho_{\text{mag}} \ , \tag{3.5}$$

where the subscripts denote the residual resistivity, the resistivity due phonon scattering and the spin-dependent resistivity, respectively.

The residual resistivity is caused by scattering of conduction electrons on lattice defects including impurity atoms and is temperature independent. In the ideal case (nonmagnetic, single-phase sample) the residual resistivity is much smaller than other terms (except at lowest temperature).

The phonon term ϱ_{ph} comes from the scattering of conduction electrons on phonons. Assuming, that the conduction electrons are a part of the one and the same s–conduction band and they are scattered into vacant states within the same band, then the $\varrho_{\text{ph}}(T)$ dependence can be aproximated by the *Bloch-Grüneisen law* derived using Debye model

$$\varrho_{\text{ph}}(T) = 4R_\Theta\left(\frac{T}{\Theta}\right)^5\int_0^{\frac{\Theta}{T}}\frac{x^5\mathrm{d}x}{\left(\mathrm{e}^x-1\right)\left(1-\mathrm{e}^{-x}\right)} \ , \tag{3.6}$$

where Θ is Debye temperature of the material and R_Θ includes, among other fundamental physical quantities, the electron-phonon coupling constant and it is proportional to the phonon part of the resistivity at Debye temperature. For a high and low temperature regions it can be derived from 3.6 as

$$\varrho_{\mathrm{ph}}(T) \propto T^5 \quad \text{for} \quad T \ll \Theta \ ,$$
$$\varrho_{\mathrm{ph}}(T) \propto T \quad \text{for} \quad T \gg \Theta \ .$$

The third term in 3.5 describes the spin-dependent scattering phenomena. In a paramagnetic region ϱ_{mag} is temperature independent and proportional to de Gennes factor (so-called spin-disorder resistivity)

$$\varrho_{\mathrm{spd}} = \frac{3\pi^2 N m^*}{he^2 E_{\mathrm{F}}} \left|\mathfrak{J}\right|^2 (g-1)^2 J(J+1) \ ,$$

where $\mathfrak{J}$ is the coupling constant of the electron-spin interaction.
In a magnetically ordered state (at temperatures below the magnetic ordering temperature) the temperature dependence of the magnetic part of the resistivity critically depends on the details of the magnetic ordering and the dispersion of the quasiparticles (magnons etc.) involved in the interaction with conduction electrons. For instance, in the non-gapped dispersion relation of ferromagnetic magnons the electrical resistivity varies as T^2 at low temperatures $T \ll T_{\mathrm{C}}$ (in antiferromagnetic compounds as T^4 for $T \ll T_{\mathrm{N}}$). In the case of presence of a gap Δ in the dispersion relation, the electrical resistivity can be described as [59]

$$\varrho_{\mathrm{mag}} = AT^2 + ET\left(1 + 2\frac{T}{\Delta}\right) \mathrm{e}^{-\frac{\Delta}{T}} \ ,$$

where E depends on the spin-disorder resistivity and the electron-magnon coupling constant.

Magnetoresistivity

Under the influence of a magnetic field we have to consider the conductivity (resistivity) as a tensor and Ohm's law write as

$$\mathbf{i} = \boldsymbol{\sigma}(T, \mathbf{B})\mathbf{E} \ ,$$

where $\mathbf{i}$ is the electrical current density, $\mathbf{E}$ is the electric field and $\boldsymbol{\sigma}$ is the temperature and field dependent conductivity tensor.[7] The conductivity tensor $\boldsymbol{\sigma}$ for an isotropic (cubic) material in the presence of $\mathbf{B} = (0, 0, B)$ is given as

$$\boldsymbol{\sigma}(B) = \begin{pmatrix} \sigma_{xx}(B) & \sigma_{xy}(B) & 0 \\ -\sigma_{xy}(B) & \sigma_{yy}(B) & 0 \\ 0 & 0 & \sigma_{zz}(B) \end{pmatrix}$$

and the corresponding resistivity tensor $\boldsymbol{\varrho}$

[7] In the absence of an external magnetic field the conductivity becomes a scalar for cubic symmetry — $\mathbf{i} = \sigma(T, \mathbf{B})\mathbf{E}$. In an applied field the symmetry is broken, but the Onsager relationships still hold $\sigma_{ij}(\mathbf{B}) = \sigma_{ji}(-\mathbf{B})$.

$$\boldsymbol{\varrho}(B) = \begin{pmatrix} \varrho_\perp(B) & \varrho_{\mathrm{H}}(B) & 0 \\ -\varrho_{\mathrm{H}}(B) & \varrho_\perp(B) & 0 \\ 0 & 0 & \varrho_\parallel(B) \end{pmatrix}$$

where $\varrho_\perp$ and $\varrho_\parallel$ are the resistivity in a transverse and a longitudinal external magnetic field and ϱ_{H} is the Hall resistivity. The transverse and longitudinal magnetoresistance are defined by

$$\frac{\Delta\varrho_\perp}{\varrho}(B) = \frac{\varrho_\perp(T,B) - \varrho(T,0)}{\varrho(T,0)}$$

and

$$\frac{\Delta\varrho_\parallel}{\varrho}(B) = \frac{\varrho_\parallel(T,B) - \varrho(T,0)}{\varrho(T,0)} \ .$$

3.5 Elastic properties

The term "elastic properties" usually refers to the properties standing in the Hook's law, generally written as

$$\sigma_{ij} = c_{ijkl}\varepsilon_{kl} \ ,$$

where σ_{ij} and ε_{kl} are the stress and strain[8] tensor, respectively, and c_{ijkl} is the elastic constant tensor (which may be determined e.g. by measurement of the speed of sound in a material).[9]

The measurement of the temperature (thermal expansion) or field (magnetostriction) dependence of the strain tensor ε_{kl} is a wide and well developed area. The study of the evolution of these properties is not restricted only to the basic research, the knowledge of the thermal expansion of materials at low temperatures is important for aerospace materials and similar industries where significant temperature changes may be expected. The thermal expansion may be used for obtaining consequent information about the material, e.g. information about the point defect (method suggested by Eshelby's theorem [60], see e.g. [61] and [62]). The knowledge of magnetoelastic behaviour of materials is important as well, e.g. it is an important property for materials used in transformers, and of course there are direct applications in actuators, transducers and motors (see e.g. [44]).

[8] see definition on page 31

[9] This is the most general form of Hook's law, in fact, the number of independent elements c_{ijkl} is 21 (reduction due to the symmetries of σ_{ij}, ε_{kl} and positive definiteness of strain energy density). This number can be further reduced by the symmetry of the medium under examination, e.g. in the case of isotropic cubic system only two elements are necessary.

Method	sensitivity	external parameters	
x-ray diffraction	10^{-5}	1.5 – 2000 K	0 – 7 T
neutron diffraction	10^{-5}	0.01 – 600 K	0 – 15 T
capacitance dilatometry	10^{-9}	0.01 – 1000 K	0 – 50 T
strain gauge	10^{-6}	1.5 – 700 K	0 – 50 T
twin microscope	10^{-6}	300 – 2000 K	×
extensometer	10^{-7}	1.5 – 700 K	0 – 30 T
tunnel tip transducer	10^{-9}	×	0 – 3 T
interferometry	10^{-8}	4 – 2000 K	×

Table 3.1: Several experimental methods for thermal expansion and magnetostriction measurements with typical parameters (after [45]).

3.5.1 General overview of methods

In the next two sections a short overview of methods used for determination of the thermal expansion and/or magnetostriction is presented. Generally, these methods can be divided in two groups — microscopic methods (e.g. X-ray and neutron diffraction) and macroscopic methods (e.g. interferometry, various types of dilatometry).

A detailed description is devoted to the methods used in this thesis, whereas the others is mentioned marginally only for comparison (for quick overview, see Table. 3.1). For a more detailed overview of the briefly mentioned macroscopic methods see e.g. review articles [63] (with an overview of available printed and electronic databases) and [64] (with an overview of data obtained on composites).

3.5.2 Microscopic methods

The microscopic methods are non-contact approaches, which provide direct information about changes of the crystal unit cell, e.g. temperature/field dependencies of the lattice parameters. Moreover, the internal stress and its spatial distribution can be analysed simultaneously.[10] The diffraction methods are important especially in the case of very small and/or irregularly shaped specimens, when it is complicated or even impossible to use any of the macroscopic methods.

For thermal expansion and magnetostriction measurements X-ray or neutron beams are used in most cases (occasionally also other types of diffraction are employed in the investigation, e.g. beams utilising electrons [68] or helium atoms [69] may be used).

An important advantage of these methods is the direct measurement of anisotropy on the powder or polycrystalline specimens, bypassing the need of single

[10] Only several notes in the context of thermal expansion and magnetostriction are discussed in this section. General introduction (in the connection to the magnetic structure determination) to the diffraction is given in section 3.6, for the detailed description of the diffraction see appropriate textbooks or monographs, e.g. [65], [66] and [67]

crystals. On the other hand, the high resolution measurements are time consuming and special care has to be taken in order to satisfy the adequate stability of sample environment (temperature, magnetic field) during the measurement.

On the microscopic scale the thermal expansion exhibits itself as a change of the interplanar spacing of lattice planes. This is connected with a change of the Bragg angle θ through the formula

$$\frac{\Delta d}{d} = -\Delta\theta \cot\theta \tag{3.7}$$

which is obtained by differentiating the *Bragg law* $2d\sin\theta = \lambda$. From the definition of the linear thermal expansion coefficient α and 3.7 we get

$$\alpha \sim \cot\theta \frac{\partial\theta}{\partial T} \ .$$

Owing to the term $\cot\theta$ one may obtain a significant increase of sensitivity and accuracy for the $\theta \to 90°$. Therefore, if possible, high-angle ($\theta > 70°$) reflections should be measured for determining the thermal expansion.

In general, the single crystal diffraction methods are preferentially utilised, nevertheless the powder diffraction methods can be used if no suitable single crystal is available, however, the advantage of the highly accurate back-reflections cannot be used.

An advantage in this case (as compared to the other types of diffraction methods) is the fact, that in this case only relative displacements are measured, consequently many complications connected with the determination of the absolute values do not apply for the thermal expansion measurements (such as zero-point correction, diffraction profile, absorption, etc.).[11]

Concerning the differences between the X-ray and neutron beams — the description behind the diffraction experiment is the same, nevertheless there are specifics of basic mechanisms. First of all, there is (generally) a tremendous difference in absorption coefficients, which reflects itself in the fact that X-ray diffraction gain information more or less from the surface only (contrary to the probing bulk properties by neutrons) and complicates the sample chamber construction. Also, the properties of the neutron beam allows to obtain information about the crystal and magnetic structure at once (see section 3.6 for details).

3.5.3 Macroscopic methods

With the macroscopic methods the expansion (contraction) of the whole sample is studied (contrary to the microscopic methods), which include also possible influences from grain boundaries, microcracks and other sample imperfections.

One of the the oldest and most frequently used method is mechanical dilatometry. The displacement resulting from the sample expansion/contraction is mechanically transmitted outside the sample chamber (usually to ambient conditions) giving

[11] The aspects of measuring absolute d values is discussed e.g. in [70].

the dependence of the displacement vs. temperature. The most common arrangement is a push rod dilatometer, which is often used for measuring of standards. The accuracy of the method is critically dependent on the material of the rod, therefore an amorphous vitreous silica (with very low thermal expansion coefficient) is used. The displacement sensor is usually realised by a linear variable differential transformer. Numerous varieties of this arrangement are known, e.g. the differential dilatometer (two specimens, one as the reference with known elastic properties) or scissors-type dilatometer.

The optical methods can be divided into three main groups. First group involves observing a specimen (or its part) and determining the spatial movement of its end or clearly defined parts (i.e. optical path is perpendicular to the displacement direction). As examples of this technique the twin telemicroscope method and various optical comparators can be mentioned. Second group is based on optical interference measurements. Contrary to previous methods, the optical path is parallel to the direction of displacement. By calculating the path difference the displacement can be determined in terms of the wavelength of the used light. Various interferometer arrangements may be involved (Fabry-Pérot, Fizeau, Michelson), e.g. dilatometer based on the Michelson tilt-compensated interferometer for the thermal expansion measurements in the range 4 – 300 K [71]. Despite the relatively simple concept, this type of methods may be extremely accurate. The last group of optical methods is based on the speckle photography or interferometry, i.e. information is obtained from the interference pattern on the sample surface and changes in this pattern allow calculation of the displacement.

In the next two sections a detailed description of the strain gauge technique and capacitance dilatometry is given. Many other techniques, which are not covered by previous and following categories, are used as well, e.g. methods employing an atomic force microscope [72], change of resonant frequency of a microwave cavity [73], thermoelastic effect [74], etc.

Strain gauge

In this method a thin foil with a meander-like wire grid is glued to the sample under investigation. The extension (contraction) of the strain gauge and the sample can be observed as a resistivity change ΔR of the strain gauge grid which depends on the change of sensor's length as well as on it's material. When measuring the temperature dependence of the sample dimension along the strain gauge the relative change of the resistivity is proportional to the temperature change

$$\frac{R(T) - R(T_{\mathrm{ref}})}{R(T_{\mathrm{ref}})} = \left(\frac{\Delta R}{R}\right)_{\mathrm{measured}} = \left[\beta_{\mathrm{g}} + g\left(\alpha_{\mathrm{s}} - \alpha_{\mathrm{g}}\right)\right] \Delta T \ , \tag{3.8}$$

where β_{g} is the thermal coefficient of the grid resistance, $\alpha_{\mathrm{s,\ g}}$ are the thermal expansion coefficients of the sample and grid, respectively and g is the gauge factor of the strain gauge.

If $\frac{\Delta R}{R}$ is measured, the thermal expansion of the strain gauge can be derived using the formula 3.8. In order to measure the thermal expansion of the sample,

the strain gauge is fixed on its surface by a special glue. The measured thermal expansion then contains contributions from the sample (temperature dependence of the sample length) and the strain gauge (temperature dependence of the grids length and conductivity). We have to measure a reference sample (e.g. copper with a well known thermal expansion [75]) to obtain the temperature dependence $\frac{\Delta R}{R}$ of the strain gauge.

The equation 3.8 can be then rewritten into the form where effects of the grid and the sample are separated as follows:

$$\begin{aligned}\left(\frac{\Delta R}{R}\right)_{\text{measured}} &= (\beta_{\text{g}} + \alpha_{\text{g}} g)\,\Delta T + \alpha_{\text{s}} g \Delta T \\ &= \left(\frac{\Delta R}{R}\right)_{\text{SG contribution}} + g\left(\frac{\Delta L}{L}\right)_{\text{sample}}\end{aligned}$$

$$\left(\frac{\Delta L}{L}\right)_{\text{sample}} = \frac{1}{g}\left(\left(\frac{\Delta R}{R}\right)_{\text{measured}} - \left(\frac{\Delta R}{R}\right)_{\text{SG contribution}}\right) .$$

The strain gauge contribution can be calculated from the measurement of a sample of known thermal expansion (Cu)

$$\left(\frac{\Delta R}{R}\right)_{\text{SG contribution}} = \left(\frac{\Delta R}{R}\right)_{\text{measured on Cu}} - g\left(\frac{\Delta L}{L}\right)_{\text{Cu}} .$$

For the measurement of the temperature dependence of the strain gauge resistivity the standard resistivity option in the PPMS was used.

Microdilatometric cell

The practical use of measuring the thermal expansion using the change of capacitance starts with a combination of capacitance dilatometry and three terminal measurement [76]. This concept was later extended for measurements of magnetostriction [77], [78] and to temperatures above room temperature [79]. Further improvement allows the use of less regular samples when using a tilted-plate principle [80], [81]. Another types of dilatometers utilising measurement of the capacitance change are based on the push-rod principle (separation of a sample from the displacement sensor) and are used mainly for temperatures above room temperature.

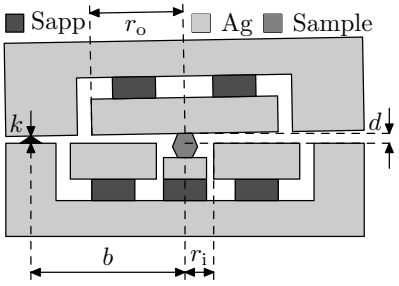

Figure 3.1: Schematic drawing of the dilatometric cell.

The microdilatometric cell [82] used in this thesis was primarily designed for a study of the magnetic phase transitions in the intermetallic rare earth compounds, where only small single crystals are frequently available ($< 1\,\text{mm}^3$). For such investigations a wide range of sample environments is necessary, therefore a small and

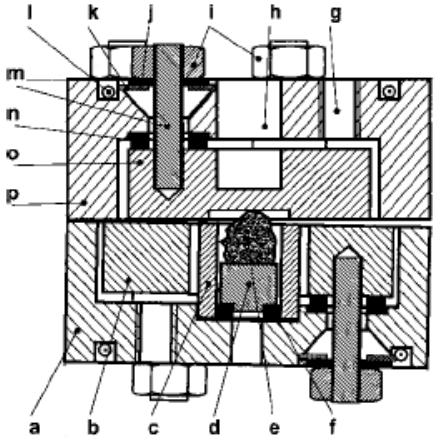

Figure 3.2: Detailed scheme of the dilatometric cell: (a) lower capacitance plate holder (Ag), (b) lower capacitance plate (Ag), (c) electrical shielding of sample space (brass), (d) sample support (Ag), (e) sample, (f) isolation washes for electrical sample isolation (sapphire), (g) mounting holes, (h) temperature sensor hole, (i) plate holder nuts (brass), (j) electrical isolation (kapton), (k) disk spring (Cu-Be), (l) groove for temperature stabilisation of capacitance wires, (m) thread bolt (brass), (n) isolation washers for electrical isolation of capacitance plate, (o) upper capacitance plate (Ag), (p) upper capacitance plate holder (Ag). (From [82].)

compact cell is suitable.[12] In order to minimise the size of the cell, a tilted plate principle was chosen [80], [81] with the sample placed in a hole in the lower capacitance plate, determining the maximal sample size ($3\times3\times3\,\mathrm{mm}^3$), see Fig. 3.1. This allows a smaller cell size and measurements of irregular samples, however, a drawback is in the complicated data evaluation and calibration (see below). The essential parts are made of silver which has a lower (as compared to copper) heat capacity and no nuclear contribution at low temperatures and in high magnetic fields.

The basic formulas describing the relation $C(T) \leftrightarrow \left\{\frac{\Delta l}{l}\right\}(T)$ for this dilatometer are shortly mentioned in the following paragraphs. The temperature dependence of the capacitance is given as

$$C(T) = \frac{2\varepsilon_0}{d(T)}\left(A_\mathrm{o}(T)\frac{1-\sqrt{1-\gamma_\mathrm{o}^2(T)}}{\gamma_\mathrm{o}^2(T)} - A_\mathrm{i}(T)\frac{1-\sqrt{1-\gamma_\mathrm{i}^2(T)}}{\gamma_\mathrm{i}^2(T)}\right) \tag{3.9}$$

where $\gamma_{\mathrm{o,i}}(T)$, $S_{\mathrm{o,i}}(T)$, $k(T)$ are the cell parameters describing the geometry and dimensions of the cell as well as the temperature dependence of the thermal expansion

[12] A small cell fits easily in a magnetic coil systems and allows a wider range of accessible temperatures.

of the cell materials.[13] Their temperature dependence is described as

$$\gamma_{\mathrm{o,i}}(T) = \frac{r_{\mathrm{o,i}}}{b}\left(\frac{k(T)}{d(T)} - 1\right) \tag{3.10}$$

$$k(T) = k(T_0)\left(1 + \left\{\frac{\Delta l}{l}\right\}_{\mathrm{Ag}}(T)\right) \tag{3.11}$$

$$A_{\mathrm{o,i}}(T) = A_{\mathrm{o,i}}(T_0)\left(1 + \left\{\frac{\Delta l}{l}\right\}_{\mathrm{Ag}}(T)\right)^2 \tag{3.12}$$

The meaning of the symbols in 3.9 – 3.12 is following (see Figs. 3.1 and 3.2):

- $C(T)$ – temperature dependence of capacitance (measured).
- $r_\bullet$ – (outer/inner) radius of capacitor plate.
- $A_\bullet$ – area of capacitor plate bounded by radius $r_\bullet$.
- k – pivot distance.
- b – distance between sample and pivot.
- T_0 – reference temperature.
- ε_0 – vacuum permittivity.
- d – gap between capacitor plates (its change determine the length change of the sample).

Because $d(T)$ appears directly in 3.9 as well as in $\gamma_\bullet$, it is necessary to solve the system 3.9 – 3.12 numerically with respect to $d(T)$. Once the temperature (or field) dependence of the gap between plates $d(T)$ is calculated it can be related to the values at initial conditions (zero field, room temperature, etc.). The following expression for the subtraction of the contribution of the cell is used

$$\left\{\frac{\Delta l}{l}\right\}_{\mathrm{sample}} = \frac{1}{l_{\mathrm{sample}}}\left(\Delta d_{\mathrm{sample}} - \Delta d_{\mathrm{Ag\ sample}}\right) + \left\{\frac{\Delta l}{l}\right\}_{\mathrm{Ag}} . \tag{3.13}$$

For the measurement it is necessary to know (except the reference data for thermal expansion of silver and sapphire) the $\left\{\frac{\Delta l}{l}\right\}_{\mathrm{Ag\ sample}}$ data which are measured with an Ag sample of a known length (called also the zero signal of the cell; due to the cells material the obtained dependence should be zero in the ideal case).

The cell was assembled at the Technical University Vienna.[14] In the Joint Laboratory for Magnetic Studies (JLMS) the cell was modified for the use in the PPMS apparatus. The insert for the torque magnetometer was adjusted in the way allowing simultaneous measurement of the temperature of the cell[15] and the capacitance[16]. The cell holder allows both principal orientations of the cell with

[13] The properties $\bullet_{\mathrm{o}}$ and $\bullet_{\mathrm{i}}$ correspond to the outer and inner diameter, respectively, cf. Fig. 3.1.

[14] For the detailed description of the assembly process and premeasurement setup see e.g. [83].

[15] A Cernox thermometer is glued on the cell and its temperature is measured using four wire technique (standard PPMS resistivity option) through the puck socket at the bottom of the PPMS sample chamber.

[16] The low temperature coaxial wires are connected at the top of the sample chamber. Special care was taken for the thermalisation of wires and fulfilling the condition for the three terminal measurement.

respect to the direction of the applied magnetic field, i.e. sample length changes can be measured in the direction along and perpendicular to the field, respectively.

The capacitance is measured by the Andeen–Hagerling AH2500A capacitance bridge [84] and the sample environment is fully controlled by PPMS without any additional constraints. For the automation of the data collection a software interface between MultiVu and capacitance bridge was written as a part of this thesis. This allows considerable simplification of experimentalist work, when all the sample chamber environment parameters (temperature, field, pressure) are controlled in the same fashion as in other PPMS options. The software enables changing all necessary bridge settings (average time, alternate mode) which may be used for this type of measurement. The data file format is identical to other PPMS options, which makes possible to observe data immediately in the MultiVu program. All substantial information is present in the data file, including sample environment parameters (obtained from PPMS), temperature of the cell thermometer (recalculated from the thermometer resistivity using calibration curve) as well as the measured capacitance and losses. As a result, the whole approach to the measurement is as similar to other options as it was possible to make.

A program allowing recalculation of the obtained $C(T)$ data was written, using the approach described earlier in this chapter (see eqs. 3.9 – 3.13). The thermal expansion of silver (contained in these equations) is calculated as the liner interpolation of data taken from literature [85]. Both programs run under MS Windows environment with a user friendly graphical interface.

Note on the coefficient of linear thermal expansion

Before the end of this section a small note concerning the coefficient of linear thermal expansion α (CTE) has to be mentioned. The results of the thermal expansion measurement are usually expressed in terms of the relative change of length $\left\{\frac{\Delta l}{l}\right\}$ or the CTE. Contrary to the self-explaining $\left\{\frac{\Delta l}{l}\right\}$ there are several different definitions of CTE, which may make the comparison with literature data slightly confusing. For the purpose of clarification and possible recalculation the mainly used formulas are shortly summarised.

Two types of definitions are in principle possible — definition over a temperature interval and definition at a single temperature. In the first case, the CTE is defined over certain temperature range, and is referred as the *mean* or *average* coefficient of expansion

$$\alpha_{\mathrm{m}} = \frac{1}{L_0}\frac{L_2 - L_1}{T_2 - T_1} = \frac{1}{L_0}\frac{\Delta L}{\Delta T}\,, \qquad \alpha_{\mathrm{m}^*} = \frac{1}{L_1}\frac{L_2 - L_1}{T_2 - T_1} = \frac{1}{L_1}\frac{\Delta L}{\Delta T}\,. \tag{3.14}$$

In the first definition a specific temperature is chosen as a reference (typically room temperature), whereas in the second case the lower limit of a specified temperature interval is used. The $\alpha_\bullet$ in these cases is related to the slope between two points on the length vs temperature curve, and represents the expansion over the particular temperature interval $\langle T_1,\ T_2\rangle$. In this case it is necessary to mention all three (two) temperatures, when quoting the $\alpha_\bullet$ value. A slightly different definition is used for

the *instantaneous* coefficient of thermal expansion at T_m

$$\alpha_\mathrm{I} = \frac{1}{L_0}\frac{\Delta L}{\Delta T} \quad \text{where} \quad T_\mathrm{m} = \frac{T_1 + T_2}{2} \ .$$

In contrast to the previous definitions the following ones are related to the temperature derivative $\frac{\mathrm{d}L}{\mathrm{d}T}$ at a single temperature and these are referred to as the *true* coefficient of linear thermal expansion (or the *thermal expansivity*). These are the limiting cases of 3.14 for $T_1 \to T_2$ and are related to the slope of the curve $L(T)$

$$\alpha_\mathrm{t} = \frac{1}{L_0}\frac{\mathrm{d}L}{\mathrm{d}T} \ , \qquad \alpha_{\mathrm{t}^*} = \frac{1}{L_1}\frac{\mathrm{d}L}{\mathrm{d}T} \ . \tag{3.15}$$

This definition (namely α_{t^*}) is used for the description of the CTE in the entire thesis (unless specified otherwise), however, noted only as α for simplicity.

3.6 Neutron diffraction

Neutron diffraction has developed in one of the most important microscopic methods during less than a century since neutron discovery [86], [87]. The reasons for this fact are quite unique properties of a neutron beam:

- Neutron has no charge. The consequent absence of any long range interaction (contrary to the Coulomb interaction in the case of charged particles) is the essence for the long penetration depth in materials, typically of the order of centimetres (whereas charges particles can see only a thin layer at the surface).
- The thermal neutron wavelength is comparable to interatomic distances in solids and consequently one may obtain information about the microscopic structure due to the interference effects.
- Neutrons are scattered by the nuclei providing complementary information to X-rays which are scattered by electron clouds. Therefore, contrary to the smooth dependence of atomic form factor on the atomic number in the case of X-rays, the scattering length is (in this context) a random function of the atomic number (and is different for different isotopes). This fact is important for the study of lights atoms (H, C, O) in the presence of heavy atoms and for the use of the isotope labelling.
- Due to its spin ($S = \frac{1}{2}$) the neutron carries a magnetic moment and interacts with unpaired or free electrons via the dipole-dipole interaction. This allows to probe magnetic structures and excitations. Moreover, the neutron beam may be polarised (possibility of separation between magnetic and nuclear contribution).

In this section, a basics of neutron diffraction in solids are reviewed, especially with a focus on magnetic structure determination using the neutron single crystal diffraction. The detailed discussion and derivation can be found in many textbooks, monographes (e.g. [65], [88]) or course notes (e.g. [66], [67]).

3.6.1 Basic description of scattering process

Generally, the scattering process can be described by a double differential cross-section, which is proportional to the number of incident neutrons scattered with an energy and momentum variation into a solid angle $\Delta\Omega$ within an energy range ΔE.

Considering an initial state characterised by the energy $\hbar\omega_\mathrm{i}$, wavevector $\mathbf{k}_\mathrm{i}$ and polarisation σ_i which is scattered to the final state ($\hbar\omega_\mathrm{f}$, $\mathbf{k}_\mathrm{f}$ and σ_f, respectively), we can calculate the double differential cross-section using the Fermi *Golden rule* as

$$\frac{\mathrm{d}^2\sigma}{\mathrm{d}\Omega\mathrm{d}\omega} = \frac{|\mathbf{k}_\mathrm{f}|}{|\mathbf{k}_\mathrm{i}|}\left(\frac{m_\mathrm{n}}{2\pi\hbar^2}\right)^2 \sum_{\lambda,\sigma} \left|\langle \mathbf{k}_\mathrm{f}\sigma_\mathrm{f}\lambda_\mathrm{f}\left|U\right|\mathbf{k}_\mathrm{i}\sigma_\mathrm{i}\lambda_\mathrm{i}\rangle\right|^2 \delta\left(\hbar\omega + \hbar\omega_\mathrm{i} - \hbar\omega_\mathrm{f}\right) \tag{3.16}$$

where the sum is over the all initial and final states. The nuclear and magnetic contributions are superimposed in the interaction potential $U(\mathbf{r})$ between the neutron and the sample. The delta function expresses the energy conservation. In the elastic case (without energy transfer, i.e. $\hbar\omega = 0$) the energy of the incident and outgoing neutron is same, which leads to equal magnitudes of momenta $|\mathbf{k}_\mathrm{i}| = |\mathbf{k}_\mathrm{f}|$. In the following only the elastic scattering is considered.

Nuclear contribution

Since the nucleus is much smaller than the thermal neutron wavelength the potential for the nuclear scattering can be written in the form of delta function — Fermi pseudo-potential is employed

$$U_\mathrm{N}(\mathbf{r}) = \frac{2\pi\hbar^2}{m_\mathrm{n}} \sum_j b_j \delta(\mathbf{r} - \mathbf{R}_j) \tag{3.17}$$

and the sum extends over a unit cell. Contrary to the X-ray case, there is no smooth relation between the scattering length b_j and atomic weight (or similar quantity characterising atom or its nucleus). The scattering length can differ significantly (even in the sign) for different isotopes of the same element. This has a significant impact on the methods used in organic material research (e.g. protein crystallography), owing to the possibility of using isotope labelling, which allows to visualise hydrogen atoms on a specific position in the structure.

Using the Fermi pseudo-potential 3.17 in the formula 3.16 allows us to explain another important property of a neutron beam with consequences in the experiment realisation — the existence of coherent and incoherent scattering. The modified formula 3.16 can be written as

$$\frac{\mathrm{d}^2\sigma}{\mathrm{d}\Omega\mathrm{d}\omega} \approx \sum_{j,j'} \langle b_j b_{j'}\rangle \mathrm{e}^{-\mathrm{i}(\mathbf{k}_\mathrm{i}-\mathbf{k}_\mathrm{f})(\mathbf{R}_j-\mathbf{R}_{j'})} \ .$$

For each atom we average over the isotopes and nuclear spins, for $j = j'$ we have $\langle b_j b_{j'}\rangle = \langle b_j^2\rangle = \langle b^2\rangle$ and for the $j \neq j'$, the is result $\langle b_j b_{j'}\rangle = \langle b_j\rangle\langle b_{j'}\rangle = \langle b\rangle^2$. Then we can formulate 3.16 as a sum of coherent and incoherent part

$$\frac{\mathrm{d}^2\sigma}{\mathrm{d}\Omega\mathrm{d}\omega} = \left(\frac{\mathrm{d}^2\sigma}{\mathrm{d}\Omega\mathrm{d}\omega}\right)_\mathrm{coh} + \left(\frac{\mathrm{d}^2\sigma}{\mathrm{d}\Omega\mathrm{d}\omega}\right)_\mathrm{incoh} \approx \langle b\rangle^2 \mathrm{e}^{-\mathrm{i}(\mathbf{k}_\mathrm{i}-\mathbf{k}_\mathrm{f})(\mathbf{R}_j-\mathbf{R}_{j'})} + N\left(\langle b^2\rangle - \langle b\rangle^2\right)$$

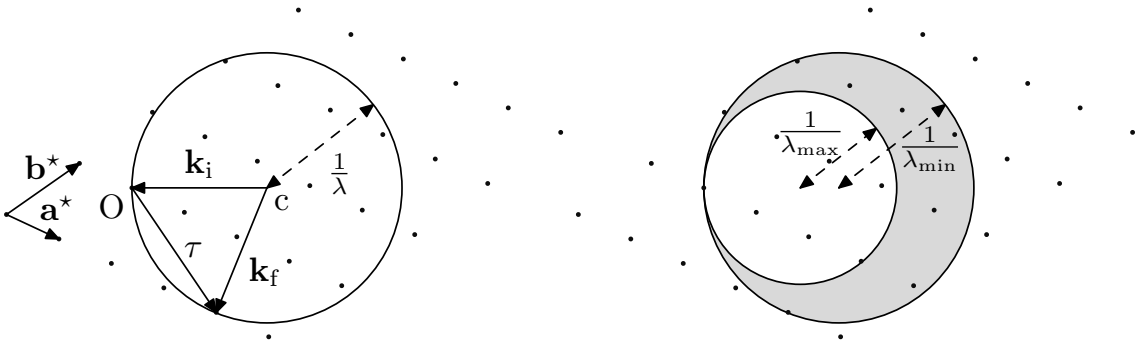

Figure 3.3: Ewald construction in the 2D reciprocal space for a single crystal sample (denoted as "c") radiated by a single wavelength source (left). The origin of reciprocal space is marked as "O", the dashed arrows denote the radius of the Ewald circle. The right hand side depicts the same situation when the sample is irradiated by a polychromatic beam (see section 3.6.3) with a wavelength span $\langle \lambda_{\min}, \lambda_{\max} \rangle$.

The incoherent scattering is responsible for an increased background and therefore for the decrease of the signal to noise ratio. For the absence of the incoherent scattering in the Al metal the aluminium foils are used for sample containers and holders, etc. Similarly, atoms of C, O and N (main components of air) scatter mainly coherently which allows simplification of instrument construction. Contrary, the V metal has the minimum coherent scattering (no Bragg peaks) and it is therefore used for sample containers and as a calibration sample for energy resolution. Finally, the coherent elastic nuclear contribution to the differential cross-section can be written in the form

$$\left(\frac{\mathrm{d}\sigma}{\mathrm{d}\Omega}\right)_{\mathrm{N,\,coh,\,el}} = \frac{(2\pi)^3}{V_{\mathrm{cell}}} \sum_{\boldsymbol{\tau}} |F_{\mathrm{N}}(\mathbf{Q})|^2 \, \delta(\mathbf{Q} - \boldsymbol{\tau}) \tag{3.18}$$

where $F_{\mathrm{N}}(\mathbf{Q}) = \sum_j b_j \, \mathrm{e}^{\mathrm{i}\mathbf{Q}\cdot\mathbf{R}_j}$ contains all structure information of the investigated crystal, $\mathbf{Q} = \mathbf{k}_{\mathrm{i}} - \mathbf{k}_{\mathrm{f}}$ is the momentum transfer and $\boldsymbol{\tau}$ is the reciprocal lattice vector. The delta function contains the Bragg law (cf. Fig. 3.3).

Magnetic contribution

Due to its magnetic dipole moment $\boldsymbol{\mu}_{\mathrm{n}}$, neutron interacts with the magnetic field $\mathbf{B}(\mathbf{r})$ of the electrons in the sample according to

$$U_{\mathrm{M}}(\mathbf{r}) = -\sum_j \boldsymbol{\mu}_{\mathrm{n}} \cdot \mathbf{B}_j(\mathbf{r} - \mathbf{R}_j) \; .$$

The magnetic dipole moment of neutron is given by $\boldsymbol{\mu}_{\mathrm{n}} = -\gamma_{\mathrm{n}} \mu_{\mathrm{N}} \boldsymbol{\sigma}$, where $\gamma_{\mathrm{n}} = -1.913$ is the gyromagnetic factor of neutron, μ_{N} is the nuclear magneton and $\boldsymbol{\sigma}$

denotes the spin operator. The magnetic field has a spin and orbital part[17]

$$\begin{aligned}\mathbf{B}_j &= \mathbf{B}_j^{\mathrm{S}} + \mathbf{B}_j^{\mathrm{L}} \\ \mathbf{B}_j^{\mathrm{S}}(\mathbf{r}) &= \nabla \times \left(\frac{\boldsymbol{\mu}_{\mathrm{e}} \times \mathbf{r}_j}{r_j^3} \right) \;;\; \boldsymbol{\mu}_{\mathrm{e}} = -2\,\mu_{\mathrm{B}}\mathbf{S} \\ \mathbf{B}_j^{\mathrm{L}}(\mathbf{r}) &= -\frac{e}{c}\frac{\boldsymbol{v}_{\mathrm{e}} \times \mathbf{r}_j}{r_j^3}\end{aligned}$$

If we put this type of potential in formula 3.16 we get the proportionality relation for the quantity corresponding to the **Q**–dependent magnetic scattering length

$$b_j^{\mathrm{M}}(\mathbf{Q}) \sim \mathbf{Q_1} \times \mathbf{M}_j(\mathbf{Q}) \times \mathbf{Q_1} = \mathbf{M}_{j\perp}(\mathbf{Q})$$

where $\mathbf{Q_1} = \frac{\mathbf{Q}}{|\mathbf{Q}|}$ stands for a unit vector in the direction of the momentum transfer and $\mathbf{M}_\perp(\mathbf{Q})$ is the component of the Fourier transform of the sample magnetisation perpendicular to the scattering vector **Q**

$$\mathbf{M}_j(\mathbf{Q}) = \int \mathbf{M}_j(\mathbf{r}) \mathrm{e}^{\mathrm{i}\mathbf{Q}\cdot\mathbf{r}} \mathrm{d}\mathbf{r} \;.$$

Similarly to the 3.18 we can write the expression describing the magnetic cross-section in the form

$$\left(\frac{\mathrm{d}\sigma}{\mathrm{d}\Omega}\right)_{\mathrm{M,\,coh,\,el}} = \frac{(2\pi)^3}{V_{\mathrm{cell}}} \sum_{\mathbf{q}} \sum_{\boldsymbol{\tau}} |F_{\mathrm{M}}(\mathbf{Q})|^2 \, \delta(\mathbf{Q} - \mathbf{q} - \boldsymbol{\tau}) \tag{3.19}$$

with the magnetic structure factor $F_{\mathrm{M}}(\mathbf{Q})$ and the propagation vector **q** (see remarks later). An approximation of magnetic structure factors based on the ab-initio calculations (Hartree-Fock wave functions in the case of the transition metal series, e.g. [89] and Dirac-Fock ones for the rare earth and actinide series, e.g. [90], [91] and [92]) is usually used for data evaluation.

Few consequences are notable in the above mentioned formulas. Firstly, the neutron can be scattered only from a component of the magnetisation perpendicular to the scattering vector and it is necessary to keep this fact in mind during the preparation of a single crystal experiment. Secondly, there is a notable difference between the magnetic and the nuclear scattering in the dependence of the form factor (**Q**–dependent part of structure factor). The nuclear form factor is in this approach independent of the momentum transfer whereas the magnetic form factor is strongly dependent and usually drops faster than the X-ray form factor.[18]

[17] Contrary to the X-ray case, neutrons cannot distinguish between spin and orbital magnetism, however these contributions may be partially separated by the analysis of the magnetic form factor dependence on the $\frac{\sin\theta}{\lambda}$ obtained from the polarised neutron experiment. As the result the ratio $\frac{\mu_{\mathrm{L}}}{\mu_{\mathrm{S}}}$ may be obtained.

[18] Because the scattering amplitude is proportional to the Fourier transform of the scattering power density in the direct space, the point like nucleus (as compared to the neutron wavelength) has the scattering amplitude independent of momentum transfer whereas the unpaired electrons (main contributors to the magnetic scattering) are located in outermost shells and therefore their form factor drops faster than the X-ray form factor.

From the 3.19 we clearly see that the condition for observation of scattered intensities is $\mathbf{Q} = \boldsymbol{\tau} + \mathbf{q}$ and the magnetic propagation vector is playing a similar role as $\boldsymbol{\tau}$ in nuclear scattering, i.e. it is bearing some information about the periodicity of the magnetic structure and play a fundamental role in the magnetic structure determination. Due to the possible complexity of the long range magnetic ordering in magnetic substances (see e.g. the extensive review devoted only to the pure rare-earth elements [93]) the description of the magnetic structure in the form of its Fourier components can be used

$$m_{lj} = \sum_{\mathbf{q}} S_{\mathbf{q}j} \exp^{-\mathrm{i}\mathbf{q}\cdot\mathbf{R}_l}$$

where m_{lj} denotes the moment of the atom j in the cell l. The Fourier coefficients may be real (in the case of a single propagation vector $\mathbf{q} = (0, 0, 0)$ or $\mathbf{q} = \frac{\boldsymbol{\tau}}{2}$) or imaginary (sinusoidal and helical structures).

The magnetic contribution may be difficult to separate experimentally from the nuclear component. The usual way is the comparison between the data obtained at temperatures above and below the ordering temperature (nuclear scattering normally does not change significantly with the temperature). If this is not sufficient, the use of polarised neutrons may help. In this case, the spin states of incoming and scattered neutron are determined, which makes it possible to separate the purely magnetic contribution [94].

3.6.2 Single crystal diffraction formalism

Generally, we have (in the case of intermetallic samples) two major approaches in the neutron diffraction. In the case of a powder sample the information obtained during scattering experiments is averaged over all possible orientations of crystallites and naturally we loose a significant amount of it. On the other hand the evaluation of the basic crystallographic information is (usually) easy and straightforward as well as the sample preparation.

The single crystal experiment may give an unambiguous information about the structure, however, the experiment is complicated in preparation (need for single crystal sample), realisation and the data evaluation (correction for secondary extinction). The additional level of complexity during the experiment is given by the necessity of the control of the sample orientation in order to enable observation of a specific part of reciprocal space. Therefore it is necessary to find the relation between the reciprocal space (observed diffraction pattern) and the direct space (orientation of the crystal with respect to the instrument coordinates).

The below discussed transformations are more or less general, the exact expressions are valid in the framework of the terminology used in the (3)4–cycle diffractometers. The transformation of the arbitrary vector $\mathbf{v}^\star$ in the reciprocal lattice coordinate system[19] to the vector $\mathbf{v}_\mathrm{c}$ in the crystal cartesian system can be written

[19] which is defined in the usual way, i.e. $\mathbf{a}^\star = \frac{\boldsymbol{b}\times\mathbf{c}}{\mathbf{a}\cdot(\mathbf{b}\times\mathbf{c})}$, etc.

as[20]

$$\mathbf{v}_\mathrm{c} = \mathbf{B}\mathbf{v}^\star$$

where

$$\mathbf{B} = \begin{pmatrix} a^\star & b^\star\cos\gamma^\star & c^\star\cos\beta^\star \\ 0 & b^\star\sin\gamma^\star & -c^\star\sin\beta^\star\cos\alpha \\ 0 & 0 & 1/c \end{pmatrix} . \tag{3.20}$$

Let now assume the instrument coordinate system rigidly attached to the φ axis of the instrument. Than the transformation between the crystal coordinates and φ–axis system is related through the orthogonal matrix $\mathbf{U}$ so that

$$\mathbf{v}_\varphi = \mathbf{U}\mathbf{v}_\mathrm{c}$$

where $\mathbf{U}$ contains information about the sample orientation (depends on the sample mounting and on the arc settings in the case of goniometer head) and is usually called orientation matrix. The general approach to its determination is described e.g. in [95].

Similarly the three other Cartesian systems connected to the χ, ω and θ axes may be defined, than the vector is transformed as follows

$$\begin{aligned} \mathbf{v}_\chi &= \mathbf{\Phi}\mathbf{v}_\varphi \\ \mathbf{v}_\omega &= \mathbf{X}\mathbf{v}_\chi \\ \mathbf{v}_\theta &= \mathbf{\Omega}\mathbf{v}_\omega \end{aligned}$$

where $\mathbf{\Phi}$, $\mathbf{X}$ and $\mathbf{\Omega}$ are rotational matrices respective to above mentioned axes and may be written as follows

$$\mathbf{\Phi} = \begin{pmatrix} \cos\varphi & \sin\varphi & 0 \\ -\sin\varphi & \cos\varphi & 0 \\ 0 & 0 & 1 \end{pmatrix}, \mathbf{X} = \begin{pmatrix} \cos\chi & 0 & \sin\chi \\ 0 & 1 & 0 \\ -\sin\chi & 0 & \cos\chi \end{pmatrix}, \mathbf{\Omega} = \begin{pmatrix} \cos\omega & \sin\omega & 0 \\ -\sin\omega & \cos\omega & 0 \\ 0 & 0 & 1 \end{pmatrix}.$$

Finally, for non-zero values of the setting angles the transformation from the reciprocal space to the laboratory frame is described by

$$\mathbf{v} = \mathbf{\Omega}\mathbf{X}\mathbf{\Phi}\mathbf{U}\mathbf{B}\mathbf{v}^\star . \tag{3.21}$$

3.6.3 Laue diffractometer VIVALDI

VIVALDI (**V**ery **I**ntense **V**ertical **A**xis **L**aue **DI**ffractometer) installed at ILL[21] in Grenoble, France [96] has the ability of rapid investigation of the reciprocal space using the white thermal neutron beam with a cylindrical image plate detector. It is complementary to the other ILL single crystal diffractometers and it is used for

[20] assuming the x axis parallel to $\mathbf{a}^\star$, y axis in the $\mathbf{a}^\star\mathbf{b}^\star$ plane and the z axis perpendicular to that plane

[21] The neutron source at Institut Laue-Langevin is 57 MW high flux reactor which is the most powerful among the existing reactor based neutron sources and is significant contributor to the neutron scattering investigation of condensed matter and particulary its magnetic properties.

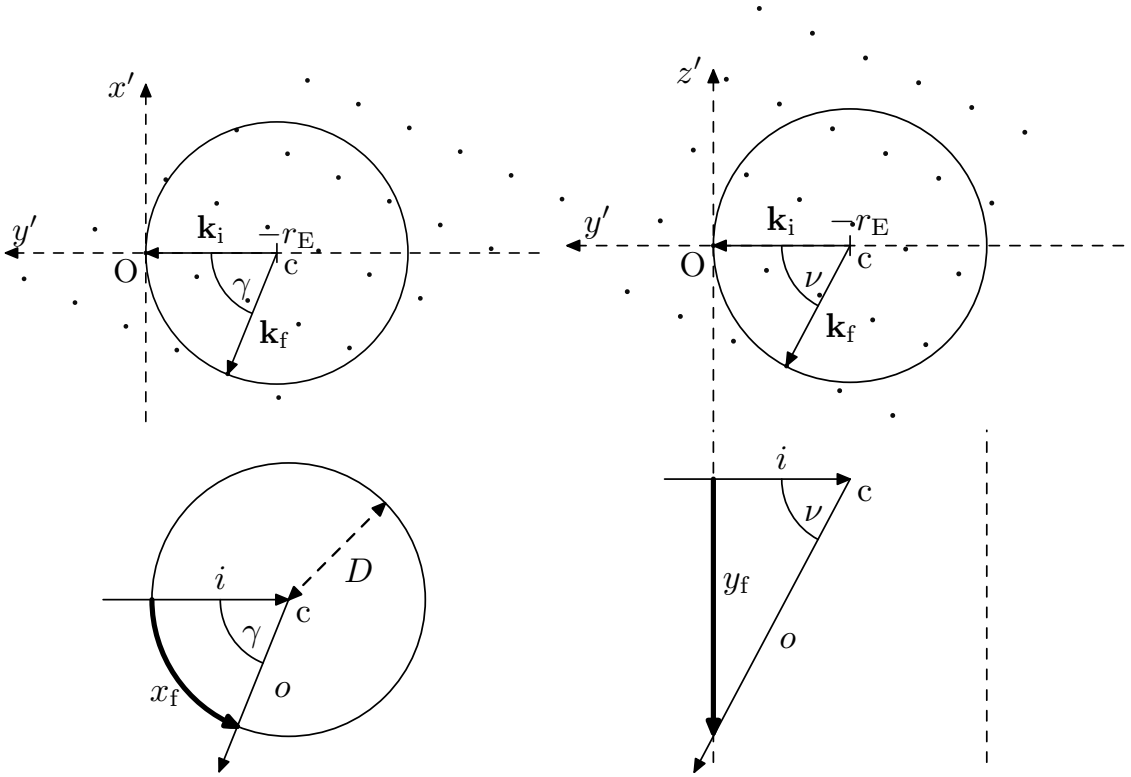

Figure 3.4: Geometrical consideration in reciprocal (upper part) and real (lower part) space for single crystal diffraction and cylindrical detector (VIVALDI case). For clarity the case with only one selected wavelength is sketched in reciprocal space. The incoming and scattered beam in real space is denoted as i and o, respectively.

studies in the fields of magnetism, charge density waves, high pressure studies and structural phase transitions. Its construction and position also allows rapid preliminary investigation, even on small single crystal samples.

The instrument is located at the end of thermal guide H22, the cylindrical image plate detector (BaFBr doped with Eu^{2+} ions with Gd_2O_3 added as a neutron scintillator) is used covering $\pm 144°$ in 2θ and $\pm 52°$ in ν. The detector cylinder axis is vertical (contrary to its predecessor LADI [97]) which allows use of an 'Orange' cryostat capable controlling temperatures down to 1.5 K. As a result we obtain a 2D projection of a large volume of the reciprocal space in one Laue pattern.

For data evaluation the use of the white beam is the main disadvantage of the method – there is no way how to identify the wavelength for the specific spot on the Laue pattern, so the Bragg's law cannot be used for the determination of the interplanar distance. Consequently, it is impossible to determine absolute values of the lattice parameters, only their ratio may be found (the same holds for the diffraction spots of magnetic origin).

Geometrical background for Laue diffraction

We defined orthogonal axes x', y' and z' in the reciprocal space (see Fig. 3.4). From the reciprocal lattice points and white spectrum of wavelengths we choose a pair $((x', y', z'), \lambda)$ which may give rise to a spot on the Laue pattern if the diffraction conditions are satisfied (for illustration of diffraction conditions satisfaction see Figs. 3.3 and 3.4). In the case of diffraction the reciprocal lattice point lies on the (Ewald) sphere of radius $r_\mathrm{E} = 1/\lambda$, with the centre at $(0, -r_\mathrm{E}, 0)$ so the whole Ewald sphere can be analytically described as

$$\frac{x'^2 + y'^2 + z'^2}{2y'} = -\frac{1}{\lambda} = -r_\mathrm{E} \ .$$

The diffraction condition can be than written as $1/\lambda_\mathrm{max} < r_\mathrm{E} < 1/\lambda_\mathrm{min}$. For the sample film distance D the reflection position on the film can be derived as

$$\begin{aligned} x_\mathrm{f} &= -D\gamma \\ y_\mathrm{f} &= \ \ D\tan\nu \end{aligned}$$

where ν in the angle between $\mathbf{k}_\mathrm{f}$ and the $y'z'$ plane and γ is the angle between $\mathbf{k}_\mathrm{i}$ and $\mathbf{k}_\mathrm{f}$ in the $x'y'$ plane (cf. Fig. 3.4)

$$\begin{aligned} \sin\nu &= \lambda z' \\ \cos\gamma &= \frac{\lambda y + 1}{\cos\nu} \ . \end{aligned}$$

The sample holder at VIVALDI has only one degree of freedom — rotation φ around the axis of symmetry of the detector; therefore the (x', y', z') is given by a modified expression 3.21

$$\begin{pmatrix} x' \\ y' \\ z' \end{pmatrix} = \mathbf{v} = \mathbf{\Phi U B v}^\star = \mathbf{\Phi U B} \begin{pmatrix} h \\ k \\ l \end{pmatrix}$$

where the $\mathbf{B}$ matrix is given by 3.20 and the $\mathbf{U}$ matrix is a product of the orientational matrices around laboratory coordinates

$$\mathbf{U} = \begin{pmatrix} \cos\varphi_z & -\sin\varphi_z & 0 \\ \sin\varphi_z & \cos\varphi_z & 0 \\ 0 & 0 & 1 \end{pmatrix} \times \begin{pmatrix} \cos\varphi_y & 0 & -\sin\varphi_y \\ 0 & 1 & 0 \\ \sin\varphi_y & 0 & \cos\varphi_y \end{pmatrix} \times \begin{pmatrix} 1 & 0 & 0 \\ 0 & \cos\varphi_x & -\sin\varphi_x \\ 0 & \sin\varphi_x & \cos\varphi_x \end{pmatrix} .$$

Data evaluation

Laue patterns obtained at ambient temperature were indexed using the LAUEGEN program [98], [99] allowing to check the overall (bulk) quality of a single crystal by observing of possible spurious extra reflections. For indexing information from

a previous powder X-ray experiment was used (cell parameters, crystallographic system and lattice type) allowing fast determination of the crystal orientation. In the subsequent step this orientation is refined (and later the geometrical and cell parameters, too) first only for the manually selected reflection and then automatically for the reflections defined by the nodal spot selection index (which is gradually increasing with increasing goodness of fit).

After refining the orientation and geometrical parameters (in particular a possible minor misalignment of the sample from the centre of the cylindrical detector) and before integration of the image it is necessary to properly characterise the used white beam, i.e. determine soft limits (minimum and maximum wavelengths and minimum d–spacing)[22] in order to avoid following possible errors:

- mis-index reflections
- too many reflections predicted (and as a result the real spots are discarded from integration due to the overlap)
- reflections treated as a singles when they are multiples (and vice versa)

After the proper characterisation of the obtained Laue pattern the .ldm (crystal, orientation and geometrical parameters [100]) and .geasc (reflection parameters) files were exported.

For the integration the ARGONNE_BOXES program was used, which is an updated version of the INTEGRATE+ [101].[23] The ARGONNE_BOXES program uses the profile fitting for integration (peak models obtained from the strongest reflections) which has significant improvements in the speed and precision in comparison with direct generalisation of the original one dimensional $\sigma(I)/I$ method [102].

Once the Laue pattern is integrated and intensities obtained the wavelength normalisation has to be done by the LAUENORM program [103]. This program compares the symmetry equivalent reflections measured at different wavelengths and refines the wavelength normalisation curve (for technical details see [104]) which takes into account the wavelength dependent factors (different flux and wavelength) as well as the wavelength sensitive response of the image plate.

All the above mentioned programs (except ARGONNE_BOXES) are a part of the CCP4 Laue suite ([99], [105] and [106]) which is continually expanded with new routines adapted to the needs of performed neutron experiments.

In the case of the investigation of magnetic phenomena (namely during the study of magnetic compounds with magnetic cell size different than crystallographic)[24] the above mentioned approach has to be modestly modified. The LAUEGEN is not able to treat fractional indices therefore a minor intervention in the

[22] Obviously, the minimum d–spacing is not anyhow related to the neutron beam properties, however, if set to wrong values the results of the pattern simulation/integration has the same errors as in the case of a wrongly determined neutron beam wavelength characteristics.

[23] The EXCHGE routine was used for the preparation of the .ge files (ARGONNE_BOXES input) from .geasc files (LAUEGEN output).

[24] For the discussion of the propagation vector determination see the following section.

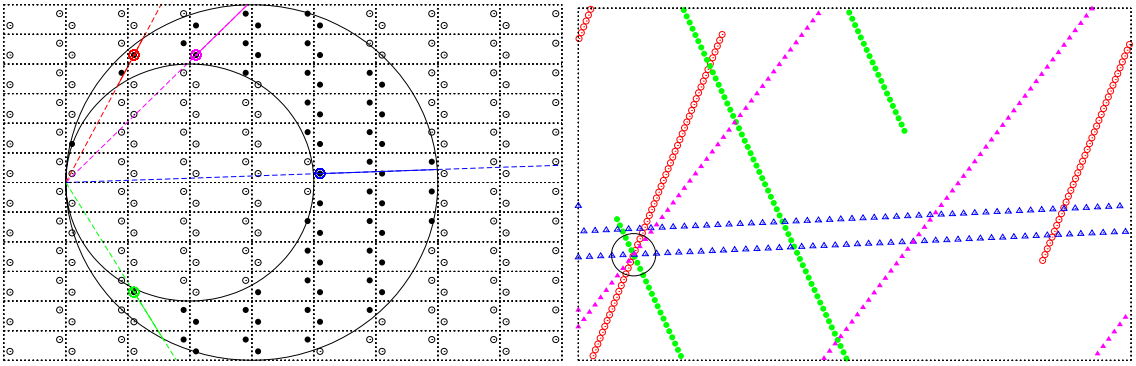

Figure 3.5: Ewald construction in the 2D reciprocal space for a single crystal sample radiated by a polychromatic source (left, cf. Fig. 3.3). The right hand side depicts the same situation where the rays from selected satellites are translated into the one reciprocal unit cell. See text for detailed description.

.geasc files produced by the LAUEGEN has to be made in order to specify additional reflection which should be integrated.[25]

Propagation vector determination

Since we use the polychromatic neutron beam the evaluation of the magnetic propagation vector (indexation of magnetic reflections) may be complicated or even impossible. In simple cases ($(0, 0, 1/2)$, $(0, 0, 1/3)$, etc.) the components of the propagation vector may be guessed or estimated by a trial and error method, however, this approach may not lead to the satisfactory result in a reasonable time for complex or incommensurate structures. For this reason two routines for propagation vector determination were implemented and tested.

The first one is based on simple geometrical assumptions and considerations. From the Laue pattern measured for a given crystal orientation the directional cosines in reciprocal space may be determined for each reflection spot. In the case of monochromatic beam the exact position in the reciprocal space may be determined, however, this is not possible when polychromatic radiation is used because the magnitude of the scattering vector is unknown. Therefore as a result of Laue pattern evaluation we obtain line segments in reciprocal space given by the directional cosines and the minimal and maximal wavelengths present in the incoming beam. The 2D example is schematically depicted in the Fig. 3.5 — in the reciprocal lattice (regular grid) the positions of magnetic satellites for $\mathbf{q} = (0.1, 0.3)$ are denoted by circles. Full circles enclosed in Ewald spheres for minimal and maximal wavelength, respectively, correspond to possible observed reflections.[26] For each of these reflections the directional cosines may be calculated (depicted as dashed lines for several of them). The solid sections of these lines represent information which

[25] A routine allowing automatise this part was written, too.

[26] In this model case the dependency of the magnetic form factor on the scattering vector is neglected for simplicity.

may be directly obtained from the measured Laue pattern, taking into account the wavelength characteristics of the beam (obtained e.g. from the evaluation of measured data in the paramagnetic regime). If we translate (see Fig. 3.5) the obtained line segments to one reciprocal unit cell we have guarantied that each of them passes the **q**–related point (each line segment is associated with one observed reflection) and therefore the propagation vector can be determined as a point with the highest intersection multiplicity. With increasing number of used reflections the occurrence of false, statistical intersections decreases.

For real application the direct implementation of this idea is proved impossible[27] hence the applied implementation of this algorithm divides the reciprocal unit cell in cubes on a regular grid and calculates the total length of line segments going through each cube. With increasing number of cubes the asymptotic behaviour indicates the possible location of propagation vector. The routine takes as an input sets of $x_\mathrm{f}, y_\mathrm{f}$ coordinates of satellite spots on the Laue pattern with the appropriate ldm file for each pattern.

In order to investigate the behaviour of the implementation of this algorithm several synthetic tests based on simulated reflection data were made. For the purpose of illustration of the method several selected examples are shown in Fig. 3.6. The input parameters were chosen in order to depict real situations where the obtained data are not perfect (lack of magnetic satellites, noisy (bad single crystal quality) data, only a few crystal orientations measured). All models were simulated for the same crystal and its initial orientation and the satellites were calculated for the propagation vector $\mathbf{q} = (0.1111, 0.2222, 0.3333)$. The obtained pairs of coordinates were used directly as input (M1 - M4), or were modified in order to simulate error coming from finite size of spots and the inaccuracy in the position spot determination (simulated by a Gaussian distribution of deviations), see the parameters in Table 3.2. For the Laue pattern simulation the $\max(h, k, l) = 2$ was used in the majority of the models, only in M1 and M4 were the Laue pattern simulations done for $\max(h, k, l) = 1$.

In Fig. 3.6 the dependency of the propagation vector coordinates on the evaluation cube size is depicted. In all cases there is an indication for the correct value of the propagation vector. In the models M1 and M5 ($\max(h, k, l) = 1$) there is high proportion of $hk0$ reflections which leads to accumulation of line segments in the first cube; this effect is suppressed with smaller cubes (or higher number of reflections, see other models). Even for the data taken from restricted volume of reciprocal space (one orientation of crystal, M1, M7, M9) it is possible to estimate the correct value of propagation vector from these dependencies and a false result is only suggested for the analysis of simulated data with large noise (M9, $\sigma = 15$ pixel).

Generally we may conclude that in the case of well-spread data (Laue patterns taken for several orientations) the routine asymptotically approaches the correct

[27] Due to the finite size of diffraction spot, crystal quality, etc. there is an error in the spot position determination which leads to a cluster of intersections with lower multiplicity instead of one intersection with maximum multiplicity. The total summed multiplicity in the cluster may be lower than the number of used reflections due to the 3D nature of the problem (error in spot position determination may lead to appearance of skew lines).

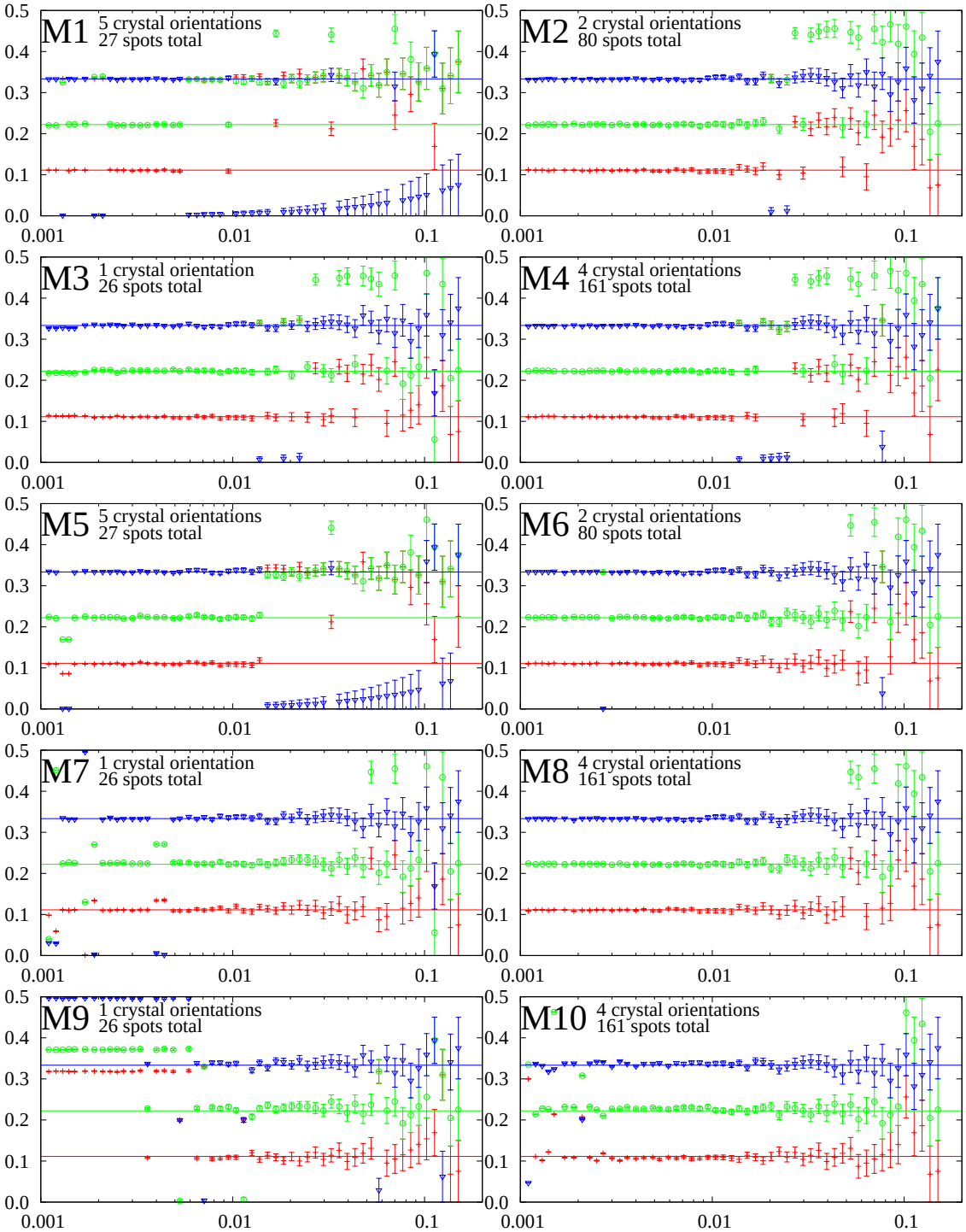

Figure 3.6: Results of a parametrical study for a rather bad data quality. The horizontal lines indicate expected results. The input data for models M1 – M4 are without any additional error, for the model M5 – M10 the error was added during the Laue pattern simulation, characterised by $\sigma = 4$ pixel for M5 – M8 and $\sigma = 15$ pixel for M9 and M10, respectively. On the x–axis is cube edge length, y–axis is q_i.

	M_{hkl}	σ	N_{o}	N_{sp}	N_{refl}	N_{ex}^{5}	N_{ex}^{10}	$\sum$	$\mathbf{q}-\mathbf{q}_0(10^{-6})$			$\sum'$
M1	1	0	5	27	12	0	0	3.20	46	98	154	1.02
M2	2	0	2	80	77	8	0	2.68	86	34	10	0.91
M3	2	0	1	26	26	3	0	2.16	136	89	40	1.00
M4	2	0	4	161	103	17	2	2.51	86	34	10	0.96
M5	1	4	5	27	12	6	0	3.13	5	-1596	-152	2.30
M6	2	4	2	80	77	19	0	3.09	-397	72	-278	2.41
M7	2	4	1	26	26	3	0	3.01	504	-122	-54	2.23
M8	2	4	4	161	103	33	3	2.98	-397	72	-278	2.34
M9	2	15	1	26	26	21	10	2.61	-892	-679	-3314	1.90
$\star$	2	15	1	26	26	$\times$	10	6.56	71	2596	-1904	5.83
M10	2	15	4	161	103	124	58	3.53	-1015	-216	-2142	3.19
$\star$	2	15	4	161	103	$\times$	58	6.58	-2895	-446	-2102	6.29

Table 3.2: List of model trials and their parameters. In the second part of the table the results from the best Monte Carlo trials are summarised. Symbols: $M_{hkl} = \max(h,k,l)$, σ (in pixels) the FWHM of the Gaussian distribution used for error simulation, N_{o} number of crystal orientations used in the model, N_{sp} number of observed spots, N_{refl} number of different reflections (some reflections may be visible for different orientations), N_{ex}^{5} (N_{ex}^{10}) number of excluded spots which were more than 5(10) pixel from position expected by $\mathbf{q}_0$, $\sum = \sum (x_{\mathrm{s}}-x_0)^2+(y_{\mathrm{s}}-y_0)^2$, $\sum' = \sum (x_{\mathrm{s}}-x_{\mathrm{t}})^2+(y_{\mathrm{s}}-y_{\mathrm{t}})^2$.

position of the propagation vector and is not significantly influenced by (statistically distributed) the error in the spot determination. However, in the case of lack of information (small evaluation cube size and small number of reflection) it may mark a false solution or show them randomly (extremely badly determined problems).

The second approach implemented is basic trial and error method based on the Monte Carlo simulation. The input information is the same as in the first approach and two modes are possible. The first one is targeted for the subsequent improvement of the result obtained from the first routine, when the obtained propagation vector $\mathbf{q}_0$ is also provided on the input, all reflections are indexed with this propagation vector and this indexation is kept fixed during the evaluation procedure.[28] The new trial

[28] At this step poorly defined reflections may be excluded based on the maximum hkl of nuclear reflection or the distance from the predicted position of satellite.

$\mathbf{q}_t$ is generated within the ellipsoid centred at $\mathbf{q}_0$ with user-provided radii.[29] In high-symmetry cases (the propagation vector along one of the principal crystallographic axes) the use of the ellipsoidal envelope allows a higher number of trials per unit time. The best solution is chosen to be the one with the minimal

$$\sum_{\text{all reflections}} (x_f - x_t)^2 + (y_f - y_t)^2$$

In the second mode of this routine a full search of reciprocal unit cell is made without any (additional) restrictions.

On the same simulated data sets the test of second approach was made. As the initial estimation (first mode) the value $\mathbf{q}_0 = (0.11, 0.22, 0.33)$ was used. The trials were generated from the sphere with radius 0.05 and centre $\mathbf{q}_0$. Reflections which were found farther than 5 pixel (also 10 pixel in the case of M9 and M10) were excluded, the indexation of reflection was allowed only up to $\max(h, k, l) = 2$ for M1 and M5 and $\max(h, k, l) = 3$ for other models. The results are summarised in the Table 3.2. The non-zero differences in the M1 – M4 models (simulated without any additional noise) is caused by several rounding operations (from the simulation of the Laue pattern integral coordinates are obtained (as in the experiment) and also the Monte Carlo routine has integral numbers on the output).

[29] The q_x, q_y, q_z are generated from a parametric description of an ellipsoid:

$$\begin{aligned} q_x &= q_{0x} + ar\cos(\alpha)\cos(\beta) \\ q_y &= q_{0y} + br\cos(\alpha)\sin(\beta) \\ q_z &= q_{0z} + cr\sin(\alpha) \end{aligned}$$

where r, α, β are randomly generated variables ($0 \leq r \leq 1, -\pi/2 \leq \alpha \leq \pi/2, -\pi \leq \beta \leq \pi$). This approach has the advantage that it naturally leads to higher volume density of trials in the vicinity of $\mathbf{q}_0$.

Chapter 4

Results and Discussion

In this chapter the obtained results are presented. First of all, the investigation of the spin fluctuation phenomena in the UCoAl and UNiAl and its influence on the elastic properties is presented, connected in the case of UCoAl with the investigation of other bulk properties related to the anisotropy of the metamagnetic transition. Following section is devoted to the discussion of elastic properties and single crystal neutron diffraction of the NdRhSn, with respect to the existence of the intermediate magnetic phase. In the third section the results of the magnetoelastic properties of the CePtSn compounds are presented, with emphasis on the existence of the (ir)reversible phase. The last section is devoted to the investigation of several compounds with 1:2:2 stoichiometry and the discussion of the connection between elastic and other properties.

Each section is prefaced by a description of the crystal structure and summarisation of previous results for each compound based on the data found in the literature. Afterwards the results obtained within this thesis are presented followed by short summary and discussion, if necessary. The overall summary (especially from the point of view of the application of new approaches, presented in the Chapter 3 (sections 3.5 and 3.6)) is presented in the Chapter 5.

4.1 UTX compounds

In the UTX[1] group of compounds a large variety of magnetic properties can be found — ranging from enhanced Pauli paramagnetism in UFeX, spin-fluctuation behaviour and metamagnetism in URu(Al,Ga) and UCoAl, respectively, to the ordering of the magnetic moments in size up to 1.5 μ_B/f.u., mainly from the U atoms.

The reason for the variety of magnetic structures in different UTX compounds is the weak interlayer exchange coupling of the U atoms and its dependence on the T element (see section 2.3 for detailed discussion). As a result, the system is very sensitive to the T element species, e.g. UCoGa orders ferromagnetically and

[1]Symbol T stands for the element from the transition metal series and X stands for the element from the s–block of the periodic table. Furthermore, the R stands for the element from either lanthanide or actinide series.

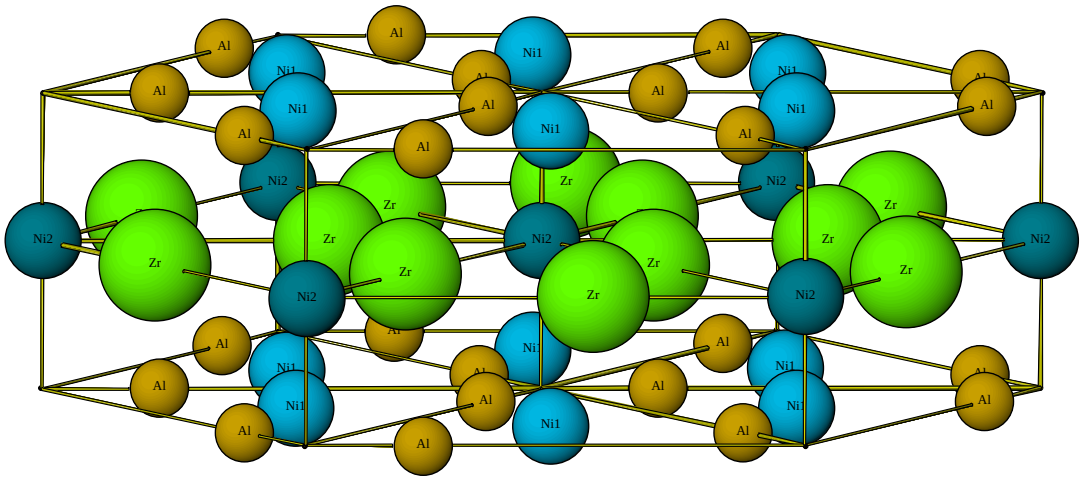

Figure 4.1: Hexagonal ZrNiAl structure.

UNiGa antiferromagnetically but a small substitution of Co into UNiGa leads to the ferromagnetic ordering (see e.g. [107]). URhAl and UIrAl order ferromagnetically, UNiAl is ordering antiferromagnetically at low temperatures with a metamagnetic transition to the field forced ferromagnetic state, whereas UCoAl behaves as enhanced Pauli paramagnet with a metamagnetic transition to ferromagnetic state at low fields applied along c-axis ($B_c \approx 0.6\,\mathrm{T}$).

4.1.1 Crystal Structure and previous results

The UTAl compounds crystallise in the hexagonal ZrNiAl–type structure. This structure (space group $P\bar{6}2m$, No. 189, Pearson symbol hP9) is an ordered Fe_2P–type derivative, which was found simultaneously for ZrNiAl [108], HoNiAl and CeNiAl [109].

This structure has a layered character. It consists of two types of basal plane sheets — one containing all U atoms and one third of the transition metal atoms and in the other remaining transition metal atoms and X atoms (see Fig. 4.1) are confined. These two types are alternating along the c-axis. Each U atom has four nearest U neighbours in the U – T plane and is enclosed in the tetrahedron of four T atoms.

The typical U – U atom separation in this structure is $350 - 400\,\mathrm{pm}$ (equal or higher than the Hill limit, refer section 2.3). Smaller and in some sense more important is the spacing in the U – T plane which has a strong influence on the 5f — d hybridisation. These electronic and crystallographic conditions lead to the extremely strong uniaxial magnetocrystalline anisotropy with the c-axis as an easy axis of magnetisation and with a paramagnetic like response in the basal plane. (The U 5f charge is compressed towards the basal plane and therefore occupying the states with orbital and spin moments locked in the c-axis direction.)

UCoAl

UCoAl crystallising in the ZrNiAl-type structure (Fig. 4.1) is reported as an archetypal itinerant 5f-electron metamagnet. The ground state is essentially paramagnetic but the c-axis susceptibility is exchange enhanced and shows a broad maximum at $\approx 20\,\mathrm{K}$ [110]. Below the characteristic temperature $T^* \approx 10\,\mathrm{K}$ UCoAl undergoes a metamagnetic transition to a ferromagnetic state with a strongly reduced U moment of $0.3\,\mu_\mathrm{B}$. The critical field of this transition is low ($B_\mathrm{c} < 1\,\mathrm{T}$), has to be applied along the c-axis. It is strongly pressure dependent ($\frac{\mathrm{d}B_\mathrm{c}}{\mathrm{d}p} \approx 2.7\,\mathrm{T\ GPa^{-1}}$) as well as sensitive to changes of chemical composition due substitutions (see e.g. [111], [30], [113] and ref. therein). The value of B_c or the onset of metamagnetism can be also efficiently tuned by Ni (increase of B_c) or Fe (ferromagnetism observed already for 2% of Fe which is suppressed by application of hydrostatic pressure and metamagnetic behaviour is recovered) [114] substitutions for Co. The substitution on the p–element site (e.g. Sn, In [115] and Ga [116]) also leads to evolution of a spontaneous magnetic moment, which can be also suppressed by hydrostatic pressure.

The strong uniaxial anisotropy is manifest by the fact that for a field applied in the basal plane only weak paramagnetic response was observed without any transition up to very high fields (magnetisation is increasing linearly up to 42 T [30]).

The ab–initio electronic calculations [117] explained the behaviour of UCoAl as a delocalised 5f-electron system with a paramagnetic ground state and a metamagnetic state at higher energies with a magnetic moment comparable to experimental values and dominated by large orbital part.

The polarised neutron diffraction experiment confirms that the metamagnetic transition takes place in the uranium sublattice ($0.30(1)\,\mu_\mathrm{B}$ per U atom at 1.7 T) whereas only a feeble Co moment ($0.054(8)\,\mu_\mathrm{B}$ at 1.7 T) is induced [20].

Detailed experimental investigation showed anomalies above the characteristic temperature $T^\star$. The temperature dependence of the thermal expansion along the c-axis shows significant deviation from the Debye behaviour and a pronounced minimum around $\sim 50\,\mathrm{K}$ (measured along the c-axis) [118], [119]. Similarly, a pronounced anomaly is observed in the temperature dependence of entropy difference $\Delta S = S_{0\,\mathrm{T}} - S_{10\,\mathrm{T}}$ [120] as well as in the electrical transport properties [121].

As suggested in the brief review above UCoAl was thoroughly explored and described by different methods, however the exact mechanism of existence and manifestation of spin fluctuation at higher temperatures as well as the strong anisotropy are not fully understood. For this reason the main emphasis was put on the description of the influence of spin fluctuations and magnetic ordering on the elastic properties of this compound.

UNiAl

This compound is one of the few antiferromagnetic compounds in the hexagonal UTX family and undergoes a field induced magnetic transition for fields applied along the c-axis [122], [123]. A significant magnetic anisotropy (c-axis is the easy magnetisation axis) is observed in the ordered state below $T_\mathrm{N} = 19.3\,\mathrm{K}$ as well

as in paramagnetic regime. The field induced transition observed at low temperatures ($B_c = 11.3\,\mathrm{T}$ at $2\,\mathrm{K}$) is accompanied by an abrupt reduction of resistivity ($\sim 45\,\%$) [124], [125], [126] as an manifestation of ferromagnetic ordering in high fields. The zero field magnetic structure was identified by neutron diffraction as antiferromagnetic with a propagation vector $\mathbf{q}_1 = (0.1, 0.1, 0.5)$ and U magnetic moments aligned along the c-axis [127]. The three magnetic moments in the basal plane were found ferromagnetically coupled and despite their crystallographic equivalency they carry different magnetic moments (two of them $1.3\,\mu_B$ and the third one $0.7\,\mu_B$). The neutron diffraction experiments in fields confirmed [128] the high-field ferromagnetic ordering with three equal moments with magnitude of $0.91\,\mu_B$ in $12\,\mathrm{T}$ ($> B_c$).

Closer investigation of strong magnetoresponsive phenomena connected with the field induced transition reveals irreversibility (for temperature below $8\,\mathrm{K}$) in the physical properties [129]. Later, it was shown [130], [131] that these are not directly connected with the field induced transition to the ferromagnetic state and slightly lower field ($\sim 9\,\mathrm{T}$) is sufficient to induce the irreversibility. The neutron diffraction study [132] explained this on the microscopic level as a transformation of the zero field cooled magnetic structure characterised by $\mathbf{q}_1$ to a different antiferromagnetic structure with $\mathbf{q}_2 = (0.173, 0, 0.5)$ which occurs for fields above $8\,\mathrm{T}$. The $\mathbf{q}_1$ related structure is not restored with decreasing field and therefore the properties measured in fields below $8\,\mathrm{T}$ are dependent on magnetic history.

Anomalies in the temperature dependence of the entropy change and the thermal expansion (along the c-axis) were observed far above ($T > 2T_N$) the ordering temperature [118] and they are ascribed to the antiferromagnetic correlations, which were traceable in the neutron diffraction experiment up to $30\,\mathrm{K}$ [127].

Similarly to the UCoAl case the goal of the investigation of this compound was examination of the influence of the spin fluctuations on the thermal expansion above T_N in magnetic fields (zero field analysis was already published [133], in fields only longitudinal data for the c-axis were known [134]) as well as a detailed study of the influence of the irreversibility on the magnetostriction in the magnetic history dependent area (only longitudinal data were published [129]).

4.1.2 UCoAl

For the measurement we used a cuboid shaped sample with dimensions $2.7 \times 2.6 \times 1.0\,\mathrm{mm}^3$ ($c \times a \times a'$, a' stands for the direction in the basal plane perpendicular to the a-axis). The temperature sweep during the measurement of the thermal expansion was typically $0.1\,\mathrm{Kmin}^{-1}$. For the measurement of the field dependence of the magnetostriction and magnetisation the field points were held constant during the data acquisition in order to exclude possible instrumental effect on the expected hysteresis.

The magnetostriction shows a field induced metamagnetic transition at $B_c = 0.62\,\mathrm{T}$ along both principal axes, respectively (see Fig. 4.2). Both dependencies are complementary; the unit cell expands at the transition along the a-axis ($1.8 \cdot 10^{-4}$) and shrinks along the c-axis ($-1.5 \cdot 10^{-4}$) yielding to the total positive volume change

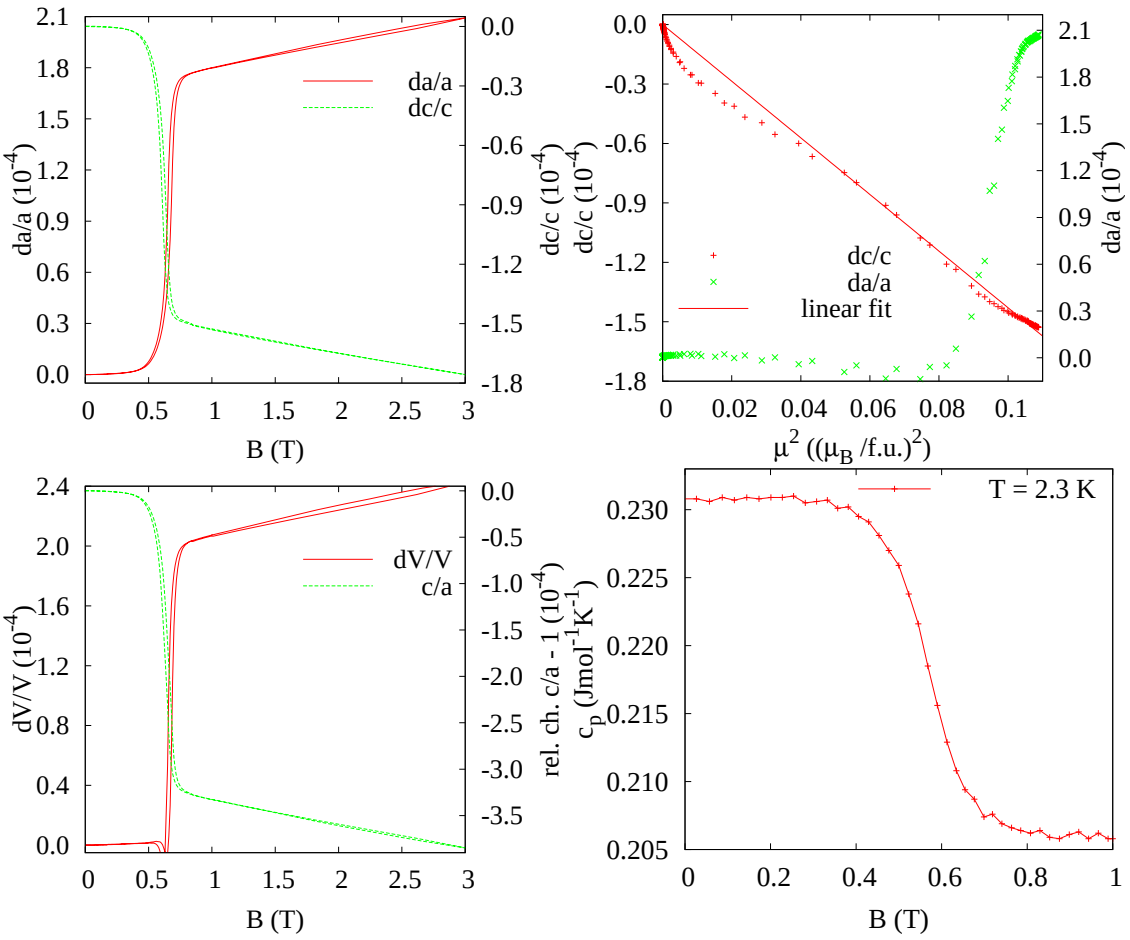

Figure 4.2: Magnetostriction (left) and magnetovolume effect (right top) for the UCoAl single crystal. Bottom right shows the field dependence of the specific heat. In all cases the field was applied along the c-axis.

of $2.0{\cdot}10^{-4}$ (in very good agreement with previous measurements on the same sample using the strain gauge technique [119]).

This metamagnetic transition is naturally accompanied by a significant hysteresis of 0.03 T as expected for a first order phase transition. The transition field and the hysteretic behaviour agree very well with the magnetisation measurements performed on the same sample (Fig. 4.4). In order to have proper characterisation of this specific sample and its quality the measurements of the electrical resistivity ($i \parallel a$, RRR = 11.5, measured magnetoresistance 7.3 % across the transition at 2 K) and field dependence of specific heat (at 2.7 K sudden decrease by 25 $\mathrm{mJmol^{-1}K^{-1}}$ at the transition (see Fig. 4.2) consistently with [135]) were performed on the same sample.

The magnetisation was fitted using the expression 2.6. The parameter a_0 was estimated from the initial slope of the $M(B)$ curve and the cri-

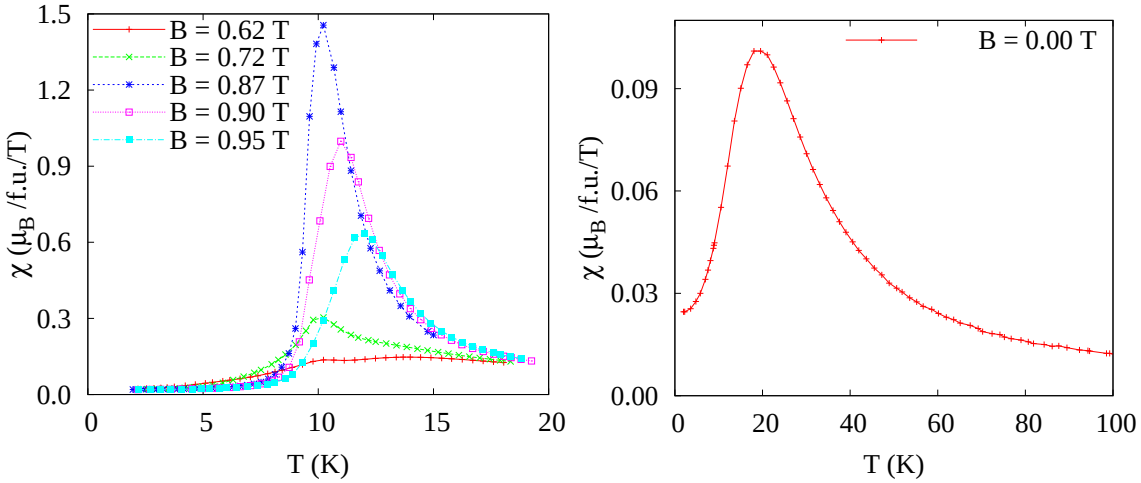

Figure 4.3: Temperature dependence of the magnetic susceptibility. The driving field was applied along the c-axis at frequency 1 kHz with amplitude 1 mT. The external magnetic field was applied along the c-axis, too.

tical field was held fixed[2] reducing the number of free parameters to one. The obtained parameters are

$$a_0 = 19.7\,\frac{\mu_\mathrm{B}}{\mathrm{T}}$$
$$b_0 = -539\left(\frac{\mu_\mathrm{B}}{\mathrm{T}}\right)^3$$
$$c_0 = 3490\left(\frac{\mu_\mathrm{B}}{\mathrm{T}}\right)^5$$

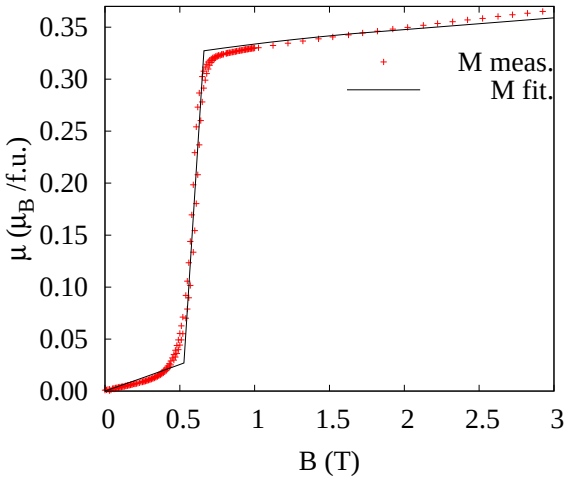

Figure 4.4: Magnetisation curve measured for the UCoAl sample for the field along the c-axis. See text for the description of the fit.

and the resulting fit is shown in Fig. 4.4. The $\frac{a_0 c_0}{b_0^2}$ ratio is 0.237 which in good agreement with [30], taking into account limited field range for fit. If we use these values for estimation of the maximal value of the inverse susceptibility using 2.10 we obtain $\chi = 0.14\ \mu_\mathrm{B}\mathrm{T}^{-1}$ which is in good agreement with experimental value (see Fig. 4.3) whereas the 'isotropic model' 2.9 leads to $\chi = 0.21\ \mu_\mathrm{B}\mathrm{T}^{-1}$. The agreement between the model value based on the magnetisation curve and the experimental data obtained from the temperature dependency may be significantly improved by using expansion of $\Delta F_\mathrm{m}(M)$ to higher orders of M [136].

[2]The two positions of extremes $M_{\mathrm{ex}_{1,2}}$ of the function $H(M)$ were found and the experimental critical field B_c was bound to parameters as $B_\mathrm{c} = 1/2\,(B(M_{\mathrm{ex}_1}) + B(M_{\mathrm{ex}_2}))$.

According to the theory of itinerant magnetism the $\left\{\frac{\Delta V}{V}\right\} \sim M^2$ dependence is expected. In Fig. 4.2 the dependencies of $\left\{\frac{\Delta l}{l}\right\}$ on M^2 are depicted for both axes. The quadratic scaling between the magnetostriction and magnetisation is well fulfilled (except slight misfit around B_c) for the c-axis whereas the dependency for the a-axis has a more complex form (and consequently the volume change too).

The temperature dependence of the thermal expansion was measured along the both principal axes without field and for a field 14 T applied along the c-axis. The results and the curve obtained by subtracting the 14 T curve and the 0 T are shown in Fig. 4.5. Below $\approx$ 80 K a strong anisotropic deviation from the Debye like behaviour is observed leading to the formation of the minimum for the c-axis around 50 K. The application of the field suppresses the minimum in the c-axis, and a plateau in the dependence measured along the a-axis is created. The difference between the curves measured with and without field shows that the spin fluctuations may be present in the system well above T_{max} and significantly influencing elastic properties of the material. The anisotropy of this feature is notable presumably due to the anisotropy of the spin fluctuation phenomena in UCoAl.

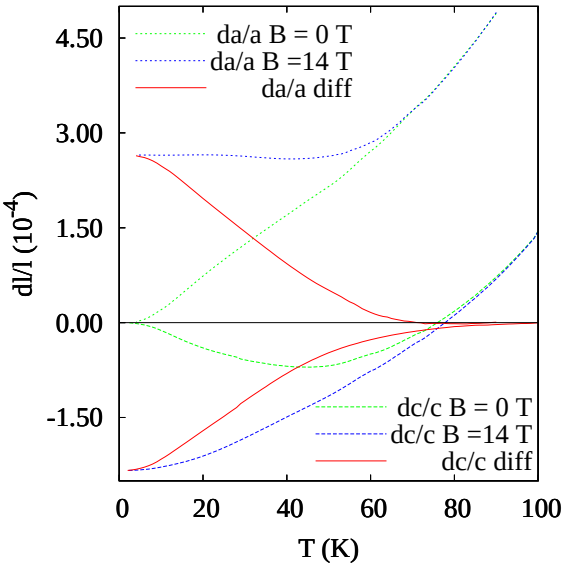

Figure 4.5: Thermal expansion of the UCoAl without field and with field applied along the c-axis as well as difference between values with and without field.

The results of the measurement of the AC magnetic susceptibility (driving field 1 mT applied along the c-axis) are shown in Fig. 4.3. The position, magnitude and shape of the zero field maxima at T_{max} temperature is in good agreement with literature data (e.g. [30]). Application of the magnetic field leads to the formation of the second maxima at lower temperatures (approx. centred at 10 K and 0.87 T) whose amplitude is of about one order of magnitude higher. This phenomenon is related to the appearance of the magnetic ordering and was also observed in the substituted materials [137].

4.1.3 UNiAl

The measurements were performed on the sample of dimensions $0.8 \times 1.2 \times \sim 3\,\mathrm{mm}^3$ ($c \times a \times a'$, a' stands for the direction in the basal plane perpendicular to the a-axis). The typical temperature sweep was $\sim 0.2\,\mathrm{Kmin}^{-1}$ and $0.18 - 0.27\,\mathrm{Tmin}^{-1}$ for the magnetostriction measurement.

The results of the measurement of the thermal expansion are shown in Fig. 4.7, similarly to the UCoAl case the magnetic field was applied only along the c-axis respecting the huge uniaxial anisotropy (see e.g. [126]). The transition tempera-

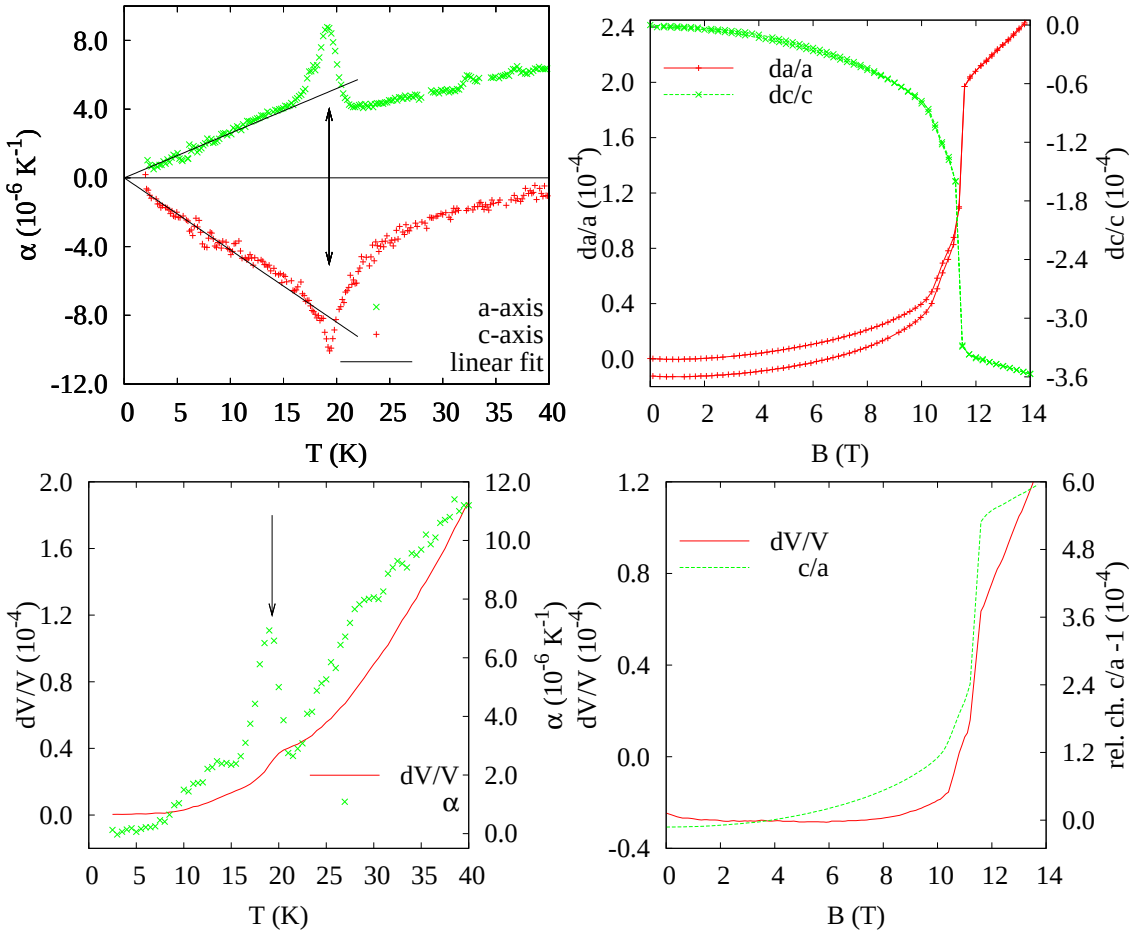

Figure 4.6: Elastic properties of UNiAl. Linear thermal expansion coefficient α (see text for the details about fit) and volume change (left). Field dependence of magnetostriction and relative change of c/a ratio (right). Field applied along the c-axis.

ture $T_N = 19.3\,\mathrm{K}$ determined from the extremes in the temperature dependence of the linear thermal expansion coefficient α (see Fig. 4.6) is in perfect agreement with published bulk and microscopic data.

The characteristic minimum in the thermal expansion along the c-axis as well as the monotonous increase along the a-axis are observed. In comparison with the zero field literature data [133] the transition is also clearly visible on the a-axis dependency and the double peak nature of the transition in the temperature dependency of α is suppressed but still recognisable. A proportionality fit $\alpha_i = A_i T$ to the measured data (for temperatures below 11 K) in Fig. 4.6 is also shown, the obtained values are summarised in Table 4.1. The apparent difference (clear visibility of the ordering) in the behaviour of the a-axis related properties is probably attributed to the different sample quality.

		$\alpha_c^{\min}$	$\alpha_a^{\max}$	A_c	A_a	$\mathrm{MS}_c(14\,\mathrm{T})$	$\mathrm{MS}_a(14\,\mathrm{T})$	$\mathrm{MS}_V(14\,\mathrm{T})$
this	#1	-10	8.8	-4.2	2.6	$-3.6 \cdot 10^{-4}$	$2.4 \cdot 10^{-4}$	$1.2 \cdot 10^{-4}$
study	#2	—	—	—	—	$-2.5 \cdot 10^{-4}$	$1.5 \cdot 10^{-4}$	$0.5 \cdot 10^{-4}$
[133]		-11	3.5	-4.6	1.7	$-2.5 \cdot 10^{-4}$	$2.2 \cdot 10^{-4}$	$1.7 \cdot 10^{-4}$

Table 4.1: Comparison of the measured quantities with earlier studies. Magnetostriction MS was calculated relatively to the 0 T.
Units: $[\alpha_i^{\bullet}] = 10^{-6}\,\mathrm{K}^{-1}$, $[A_i] = 10^{-7}\,\mathrm{K}^{-2}$

With application of 14 T magnetic field along the c-axis the anomaly is partially removed in the c-axis dependency whereas a plateau with a shallow minimum appears in the a-axis dependency (see Fig. 4.7). There is no sharp anomaly neither in the longitudinal, nor in the transversal component. The difference between the curves measured with and without magnetic field, respectively, is noticeable in both directions for temperatures well above ($\sim 2T_\mathrm{N}$) ordering temperature, supporting idea of strong influence of the antiferromagnetic fluctuations on the elastic properties.

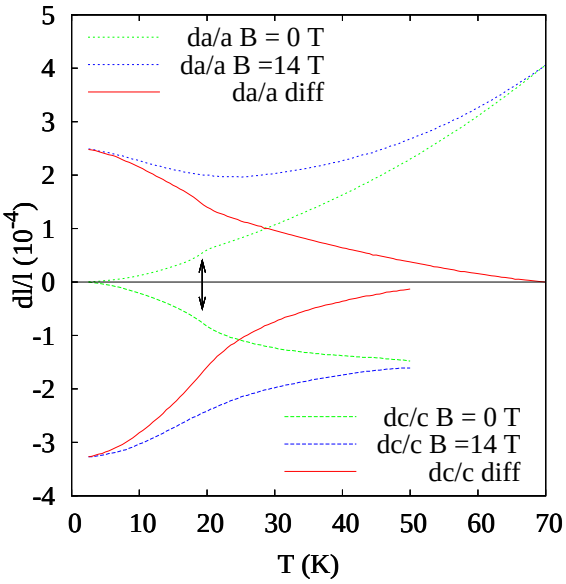

Figure 4.7: Thermal expansion of UNiAl without field and with field applied along the c-axis as well as difference between these values. The arrows indicate the transition temperature T_N determined from the extremities in the $\alpha(T)$ (see Fig. 4.6).

The magnetostriction measurement at 2 K (field applied along the c-axis) shows the field induced transition (see Fig. 4.6) at 11.4 T in good agreement with published longitudinal magnetostriction [134] data as well as with results from as other bulk methods ([130], [124], etc.). In order to investigate the possible effect of irreversibility, which was observed in other bulk properties, several field scans were performed.[3] For the transversal sample orientation there is an irreversibility after the first field scan in the size of $1.2 \cdot 10^{-5}$, i.e. the a-axis becomes longer, which is stable and is not removed neither increased by further magnetic field cycling. No similar anomaly ($> 1 \cdot 10^{-6}$) was observed for the longitudinal geometry. In order to exclude a possibility of uncorrect mounting and/or sample movement rising from the thermal relaxation in the cells spring several measurements were performed. Also the second sample was measured (see Table 4.1 for comparison) confirming the absence of the irreversibility for the longitudinal geometry and showing an anomaly of $5 \cdot 10^{-6}$ in

[3] 0 T → 14 T → 0 T → 14 T → 0 T

the transversal measurement.

The absolute value of this anomaly as well as the value of the magnetostriction at high fields is different, which should be probably attributed to the different quality of the samples as indicated also by the variation of the thermal expansion measurements in comparison with the published data. This idea is also supported by the upturn in the magnetostriction along both directions around 10 T (only in the first sample) which may be explained as the predominant influence of the rotation of the propagation vector [128] and which was not observed in the second sample.[4]

4.1.4 Conclusions

These two compounds were studied at the beginning of the thesis and were chosen due to the partial knowledge of their elastic properties, leaving open the questions about the temperature range where the fluctuations can influence the properties of this compounds and their effect on the observed anisotropy. The obtained results, summarised in last two sections, agree very well with the previously published data. In the case of the UCoAl the agreement is perfect [119], contrary to the UNiAl case ([133], [134] and [129]), were minor discrepancies were found. This seems to be caused by small sample dependency in the quality or stoichiometry.

The comparison of the thermal expansion measured in zero field and in the high field, respectively, applied along the c-axis indicates, that spin fluctuations play an important role in the behaviour of these compounds well above characteristic temperatures, as it was indicated by effects observed on other properties. Also, the notable anisotropy in this field dependent contribution is observed well above the characteristic temperatures, too.

4.2 NdRhSn

4.2.1 Crystal Structure and previous results

The RRhSn (R = La, Ce, Pr, Nd) compounds crystallise [138], [139] in the hexagonal ZrNiAl-type structure (see Section 4.1.1 and Fig. 4.1). Among these compounds, the LaRhSn was found superconductive below 2 K [139], [140], CeRhSn was reported as a valence fluctuator [141] and ferromagnetism was revealed [142] in PrRhSn below 3 K.

The NdRhSn compound was originally reported [138] as ferromagnetic like at low temperatures (4.2 K) with the susceptibility following Curie – Weiss law for temperatures above 40 K ($\theta_p = 12$ K and $\mu_{eff} = 3.55\,\mu_B$). However, no ordering temperature was mentioned. On the other hand, a later study [143] reports NdRhSn as ferromagnetic with Curie temperature 10.3 K, also reporting onset of superconductivity below 6.9 K (determined from resistivity and susceptibility measurements). Only structure type is mentioned, no details about lattice parameters.

[4] The field dependence of the magnetostriction in this intermediate region is linear, and its extrapolation leads to the field 9 T, which is close to the reported appearance ($7-8$ T) of the new magnetic structure [128].

The lack of detailed information and inconsistent claims in literature was the motivation for the detailed single crystal study [144] accompanied by the ab initio calculations. The analysis of a diffraction pattern of a pulverised part of a single crystal revealed significantly different lattice parameters than in previous work [138]. The specific heat data clearly show two magnetic phase transitions at 9.8 K (presumably to antiferromagnetic type of ordering) and 7.6 K. These transitions coincide with a cusp and an abrupt change of the low field ($B < 0.3\,\mathrm{T}$) magnetisation vs. temperature curve. In fields from 0.3 T higher we observed only one visible transition. Significant anisotropy ($0.7\,\mu_\mathrm{B}$ vs. $2.3\,\mu_\mathrm{B}$ at 2 K and 9 T for field applied along a-axis and c-axis, respectively) was also reported. No evidence of any superconductive transition was observed down to 2 K. The results of ab initio calculations (using the experimentally determined lattice parameters) showed that magnetic moment beard by Rh atoms cannot exceed $0.1\,\mu_\mathrm{B}$.

Almost simultaneously a revision of the work [143] was published [145]. Authors used a small single crystal for crystallographic analysis and a polycrystalline sample for AC and DC magnetic measurements and ^{119}Sn Mössbauer spectroscopy. The magnetic phase transition temperature was determined as 10.6 K and ferromagnetic character of ordering was proposed. It is claimed that the results of Mössbauer spectroscopy below the transition temperature support a possibility of non-collinear ferromagnetic ordering with the Nd spins close to the c-axis.

4.2.2 Elastic properties

The measurements of the thermal expansion and magnetostriction were performed along both principal axes. The magnetic field was applied only along the c-axis, which is the easy axis in this compound [146]. The thermal expansion data were taken during the heating with the speed of $0.05 - 0.10\,\mathrm{Kmin^{-1}}$ after cooling in zero field.

The results are depicted in Fig. 4.9. Both transitions are clearly visible on the temperature dependence of the thermal expansion. The transition at $\sim 9.8\,\mathrm{K}$ is accompanied by a change of slope. The thermal expansion has opposite sign in the two main crystallographic directions keeping the overall positive volume change. The low-temperature transition is accompanied by significant jump (in the order of 10^{-4}) in both directions, resulting again in a positive volume change ($\sim 2 \cdot 10^{-5}$).

Based on these data, an estimation of the pressure influence may be made. For the $\frac{\mathrm{d}T_\mathrm{N}}{\mathrm{d}p}$ the Ehrenfest relation 3.3 is used, the $\Delta c_p = 6.5\,\mathrm{Jmol^{-1}K^{-1}}$ estimation was taken from the literature [144], $V_\mathrm{m} = 57.5\,\mathrm{cm^3mol^{-1}}$ and the α_x were determined from thermal expansion data as $1.7 \cdot 10^{-5}$ for the a-axis and $-4 \cdot 10^{-5}$ for the c-axis, respectively. From the obtained changes ($1\,\mathrm{K\,GPa^{-1}}$ for the a-axis and $-2.8\,\mathrm{K\,GPa^{-1}}$ for the c-axis, respectively) for the application of uniaxial pressure the change of the transition temperature with the hydrostatic pressure may be estimated as $\frac{\mathrm{d}T_\mathrm{N}}{\mathrm{d}p} = \sum_x \frac{\mathrm{d}T_\mathrm{N}}{\mathrm{d}p_x} = -0.5\,\mathrm{K\,GPa^{-1}}$. Similarly, the estimation for the T_t pressure dependence may be calculated from Eq. 3.2 (the ΔS was estimated from [144] as $0.5\,\mathrm{Jmol^{-1}K^{-2}}$) leading to the value $\frac{\mathrm{d}T_\mathrm{t}}{\mathrm{d}p} = -4\,\mathrm{K\,GPa^{-1}}$, i.e. the occurrence of the intermediate phase should be extended by applying hydrostatic pressure.

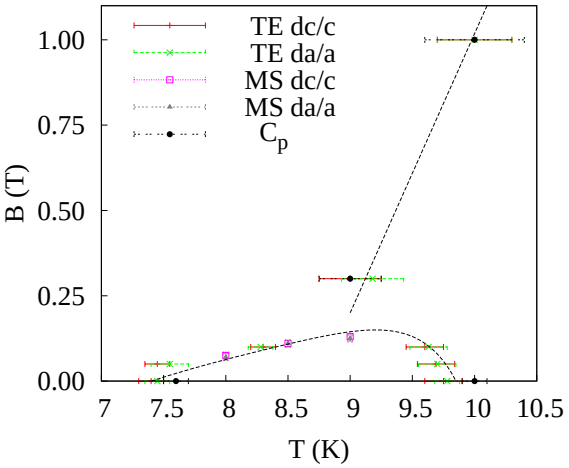

Figure 4.8: The proposed magnetic phase diagram ($B\|c$) based on the specific heat data from the literature [144] and the measured elastic data.

The magnetostriction data show a low field transition for fields below 0.2 T in the intermediate phase. For temperatures above 9 K the transition is not visible as well as for temperatures below 7 K. The jump (its sign and magnitude for different directions) at the transition is similar to the behaviour of the low-temperature transition in the temperature dependence of the thermal expansion.

The obtained transition temperatures and fields are summarised in Fig. 4.8 with sketched magnetic phase boundaries. The measured results fit very well to the previously measured specific heat data [144].

4.2.3 Neutron diffraction

The magnetic structure was determined using the VIVALDI white beam Laue diffractometer. Due to the poor quality of the original sample the new sample was grown.[5]

Laue patterns were taken at several orientations and temperatures; a special care was taken around the temperature interval where the intermediate phase was expected. In the paramagnetic region the Laue patterns show only one grain sample and have been completely indexed using the published crystallographic information [144].

Below approximately 10 K, the additional spots of magnetic origin appears, having increasing intensity with decreasing temperature and the maximum around 8 K followed by decreasing intensity and finally vanishing at 7 K. A closer inspection of the positions of these satellites (for details see section 3.6.3) shows, that all satellites can be indexed by one propagation vector (0, 0, 0.0904).[6] For the analysis 17 Laue patterns measured at temperature 8 K were carefully investigated and together 1401 spots (of magnetic origin) was treated. Using the first routine described in section 3.6.3 the solution (0.001(1), 0.007(1), 0.099(1)) was obtained. The subsequent improvement of this estimation by second routine (from 1401 spots were 89 excluded (too far from expected positions) and in the rest of them there were 477 independent reflections) lead to the final above mentioned propagation vector.

[5] The neutron diffraction experiment was performed approximately one year after the elastic experiments and the sample quality deteriorate with time. On the new crystal the heat capacity was measured prior to neutron experiment showing the same bulk properties as in [144].

[6] Alternatively, this propagation vector can be described as medium periodicity commensurate structure $(0, 0, \frac{1}{11})$.

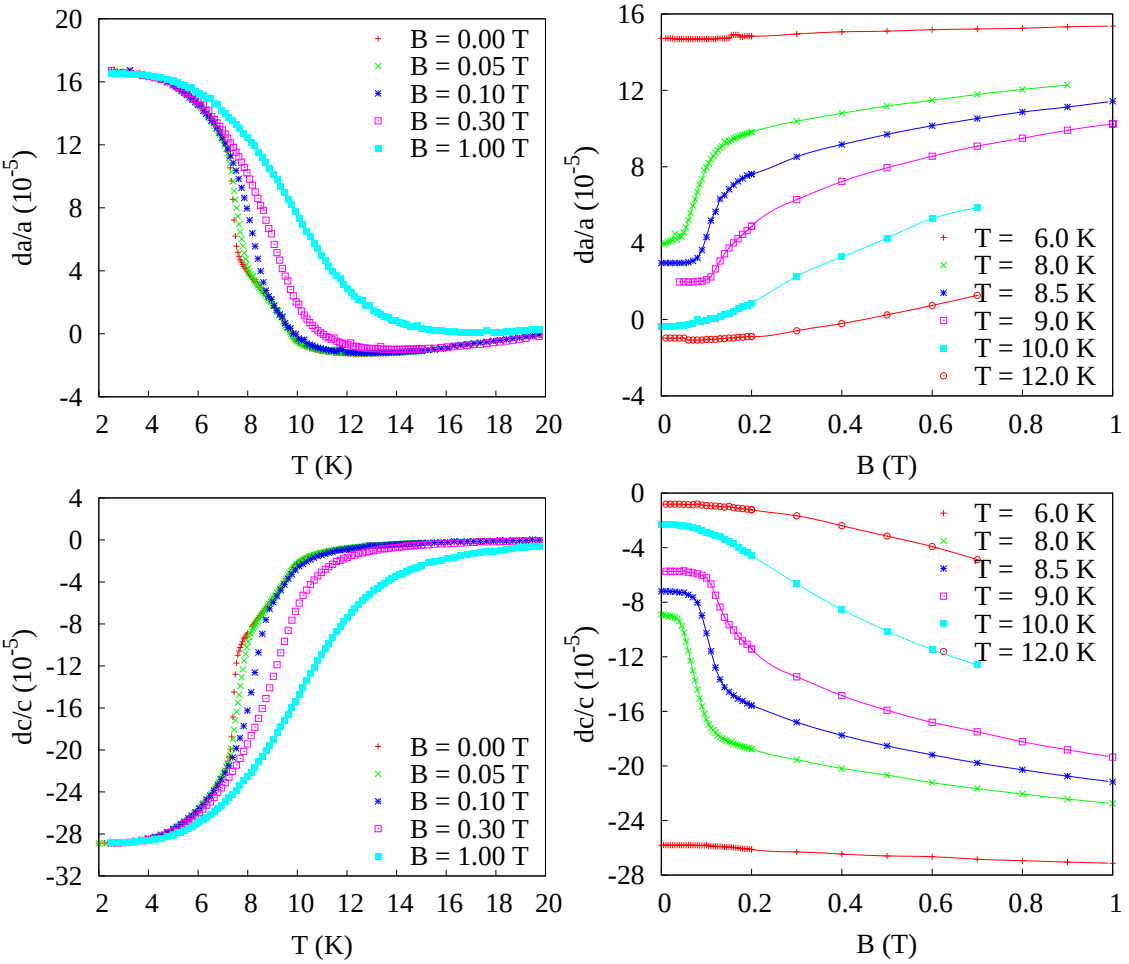

Figure 4.9: Temperature dependence of the thermal expansion in the vicinity of the double phase transition at different magnetic fields (left). Field dependence of the magnetostriction for low temperatures (right). In all cases the field was applied along the c-axis.

With this propagation vector all additional reflection present in the intermediate temperature region can be indexed.

For the example of indexation see Fig. 4.10 where a section of the Laue pattern is shown with the indexation of observed spots. The inspection of Laue patterns taken for $T_t < T < T_N$ revealed that the obtained propagation vector is temperature independent, see right panel of Fig. 4.10 for illustration.

For temperatures below T_t no additional spots were observed (in comparison with the paramagnetic Laue patterns) indicating the same size of the crystallographic and magnetic unit cell.

In order to obtain the moment magnitude and direction, the detailed analysis of the integrated intensities is planned.

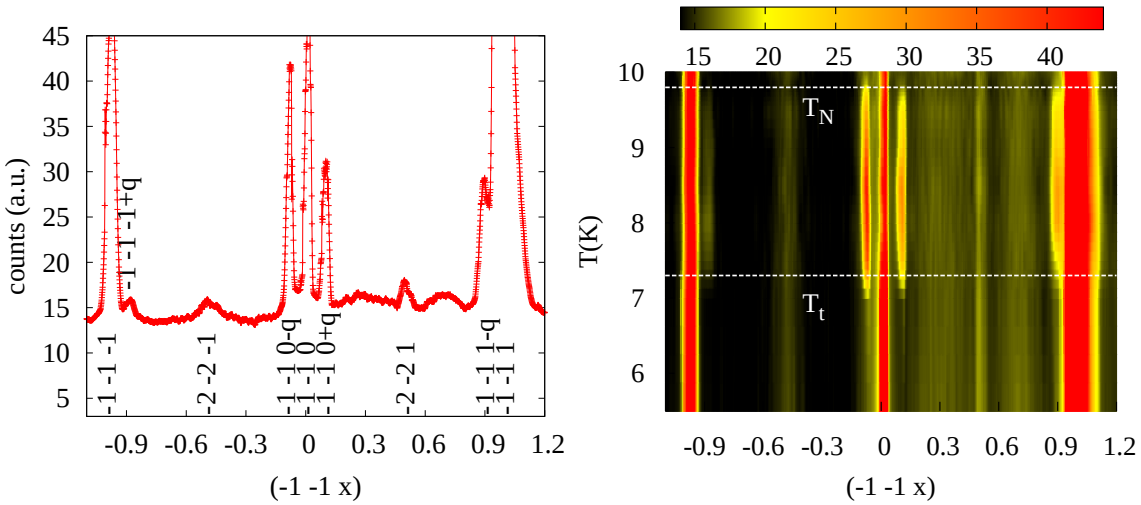

Figure 4.10: Indexed linear cut from the Laue pattern at one selected orientation at temperature 8.5 K (left) and its evolution with temperature (right). The lines indicate the transition temperatures as determined from the elastic measurements.

4.2.4 Conclusions

The thermal expansion and magnetostriction data clearly indicate existence of the intermediate magnetic phase (reported in [144]) present in low fields at the temperatures between approximately 7 K and 10 K, contrary to some previous studies [145]. The results of our elastic studies were complemented by single crystal Laue diffraction on different single crystals confirming the existence of the intermediate phase, having the magnetic periodicity approximately eleven times larger than crystallographic in the intermediate phase and the same size of the magnetic and crystallographic unit cell below T_t.

4.3 CePtSn

Different electronic and magnetic ground states can be found in the CeTX series. For the Ce^{3+} an effective moment (in the Curie-Wiess law) is expected to be $\mu_{eff} = 2.54\,\mu_B$ and saturated magnetisation $M_S = 2.14\,\mu_B$, however only in few of CeTX compounds can reach up to these value, indicating strong crystal field influence or intermediate valence. Various different crystal structures are observed in these compounds, significantly influencing the ground state properties and making difficult to observed any systematic tendencies in the CeTX series.

4.3.1 Crystal Structure and previous results

The CePtSn compound belongs to the group of CeTX crystallising in the orthorhombic TiNiSi–type structure (see Fig. 4.11). The TiNiSi structure (space group *Pnma*,

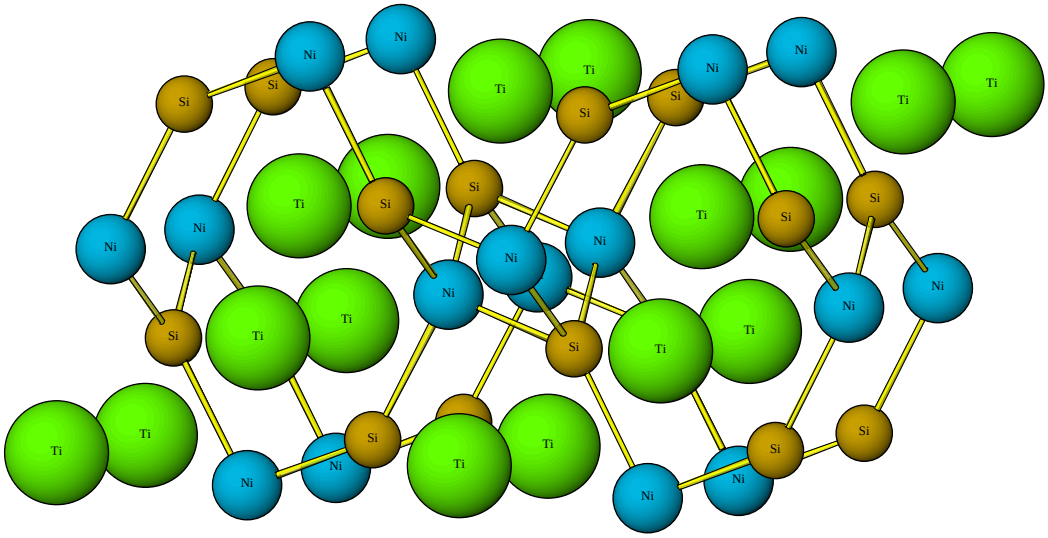

Figure 4.11: Orthorhombic TiNiSi structure ($2a \times 2b \times c$).

No. 62, Pearson symbol oP12) is a low-symmetry variant of the $CeCu_2$ structure type. This structure can be also seen as distorted ZrNiAl-type structure.[7]

At first the CePtSn single crystal diffraction data were analysed within the noncentrosymmetric $Pn2_1a$ space group, which gives slightly better R values than $Pnma$ (0.029 vs 0.031) [150]. The first study of magnetic properties [151] found ordering temperature at $T_N = 7.5\,K$ and second phase transition at $T_t = 5\,K$. These results were later confirmed using the ^{119}Sn NMR technique [152]; the onset of the magnetic ordering (disappearance of signal) was found at 7 K.

As expected from the comparison with the other CeTX compounds a strong anisotropy of electronic and magnetic properties was observed in magnetic fields (see eg. [153] and references therein). The easy axis of magnetisation is the a-axis ($1.2\,\mu_B$/f.u. at 35 T with some tendency to saturation in highest fields [154], but well below the theoretical value $2.4\,\mu_B$ per Ce^{3+} ion). For the field applied along this direction a field induced transition is observed at 12.5 T, accompanied by a sharp drop of magnetoresistance (20% at 1.8 K). However, only a minor S-shaped curvature is visible on the magnetisation data. The c-axis was identified as the hard axis with $0.5\,\mu_B$/f.u. at 35 T and 4.2 K. Consequently, no field dependencies of transition temperatures nor any other features were visible upon this field application.

The most interesting behaviour is observed for the field applied along the b-axis. The magnetisation curve taken at low temperatures undergoes a sharp transition 11 T connected with a small hysteresis. Also in this case an abrupt change in magnetoresistance occurs, connected with a step-like increase ($\sim 10\%$ at 1.8 K).

[7] Several RTX compounds can crystallise in both, the ZrNiAl-type and TiNiSi-type structures, depending on the thermal history of the sample, e.g. RPdAl [147], or structural phase transition between them may be observed, eg. TbPdAl [148]. There is no direct relationship between TiNiSi and ZrNiAl structures, however a connection can be seen [149] through binary prototypes, i.e. $CeCu_2$ and Fe_2P.

A small feature at the magnetisation curve reflects the low-field transition at 3.5 T. This transition is connected with the remarkable drop of the magnetoresistance ($\sim$ 30% at 1.8 K) and its occurrence is strongly dependent on sample history (is irreversible and is not observed in the field cooled state ($B_b > 3.5\,\mathrm{T}$)).

The first neutron diffraction [155] performed on a CePtSn single crystal shows magnetic reflections at positions $\mathbf{Q} = (h,\, k \pm q,\, l)$ where h, k and l are integers and $q = 0.466$ and 0.418 in the low- and intermediate-temperature phases, respectively. The data analysis was consistent with the sinusoidal magnetic structure characterised by propagation vectors $\mathbf{q} = 0.466\mathbf{b}^\star$ and $\mathbf{q} = 0.416\mathbf{b}^\star$ in the two magnetic phases and magnetic moment of $0.84\,\mu_\mathrm{B}$ at 2 K and $0.60\,\mu_\mathrm{B}$ at 4.8 K, respectively. However, no clear conclusion may be made about the moment direction.

The later neutron powder diffraction experiment [156] confirmed the magnetic ordering below T_N with $\mathbf{q} = (0,\, 0.428,\, 0)$ but there was no evidence for the T_t transition.

Contrary the presumably incommensurate magnetic structure, the μSR experiment [157] shows a sharp single precession frequency (at $T = 5.5\,\mathrm{K}$) with weak damping indicating a well defined internal field. The dramatic change was observed in the μSR signal at T_t indicating more complex behaviour than a simple change in propagation vector. In order to explain contradictory data from μSR experiment and neutron diffraction a semiquantitive spin-flip model was proposed [158] based on the representational analysis.

Recently performed extensive study [159] shows a significant sample dependence on the parameters of magnetic ordering. The differences were observed both in the transition temperatures as well as in the propagation vectors and their temperature dependence. In the same study an explanation of the nature of the irreversible phase was proposed: two types of AF domains are presented at zero field and 2 K and the domain population redistribution process is irreversible with application of the magnetic field. Within this model, explanation of the giant magnetoresistance effect is based on the strongly different resistivity behaviour of these domain types [160].

4.3.2 Thermal expansion

Due to its peculiar properties, CePtSn was the most thoroughly (by means of thermal expansion and magnetostriction measurements) studied system in this work.

The available sample was well shaped for the use in the dilatometric cell (cuboid with dimensions $1.50 \times 3.29 \times 1.47\,\mathrm{mm}^3$ ($a \times b \times c$) without any cracks, holes or irregularities on the surface or edges). The main emphasis was on the investigation of the behaviour of the sample for fields applied along the b-axis where the irreversible phase was found at low temperatures, therefore the longitudinal as well as both the transversal geometries were studied. For fields applied along the a-axis and c-axis only longitudinal data were collected (for overview see Table 4.2).

The majority of thermal expansion dependencies were measured in the sweep mode with the typical speed of $50 - 75\,\mathrm{mKmin}^{-1}$, for the measurement of magnetostriction curves the field was held constant during the data acquisition.

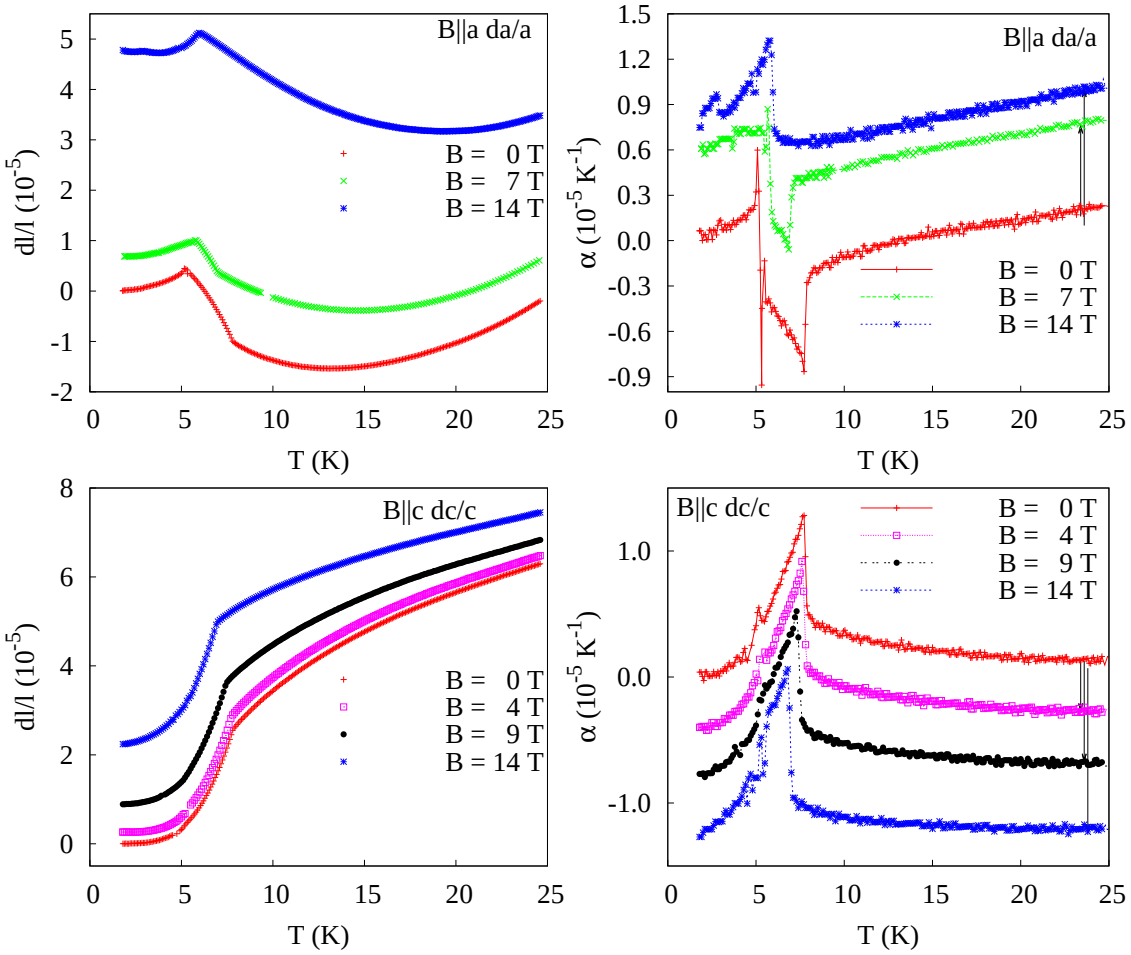

Figure 4.12: Temperature dependence of the thermal expansion (left) measured in longitudinal geometry for field applied along *a*-axis and *c*-axis. See 4.14 for detailed description.

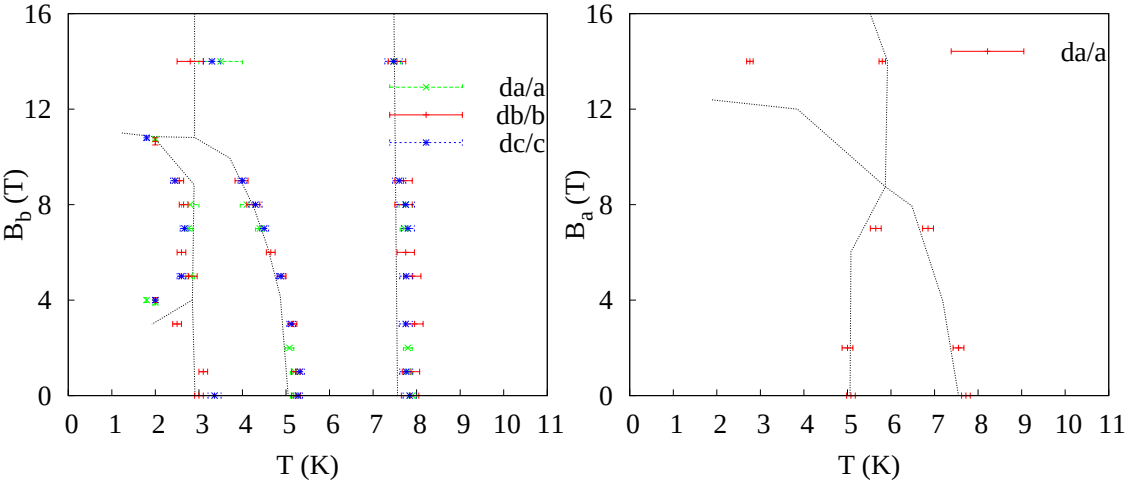

Figure 4.13: The magnetic phase diagram for fields applied along the *b*-axis (left) and *a*-axis (right). The data for the dotted lines indicating the phase borders were taken from [159]. Only transitions obtained from zero field cooled state with increasing field or temperature are shown.

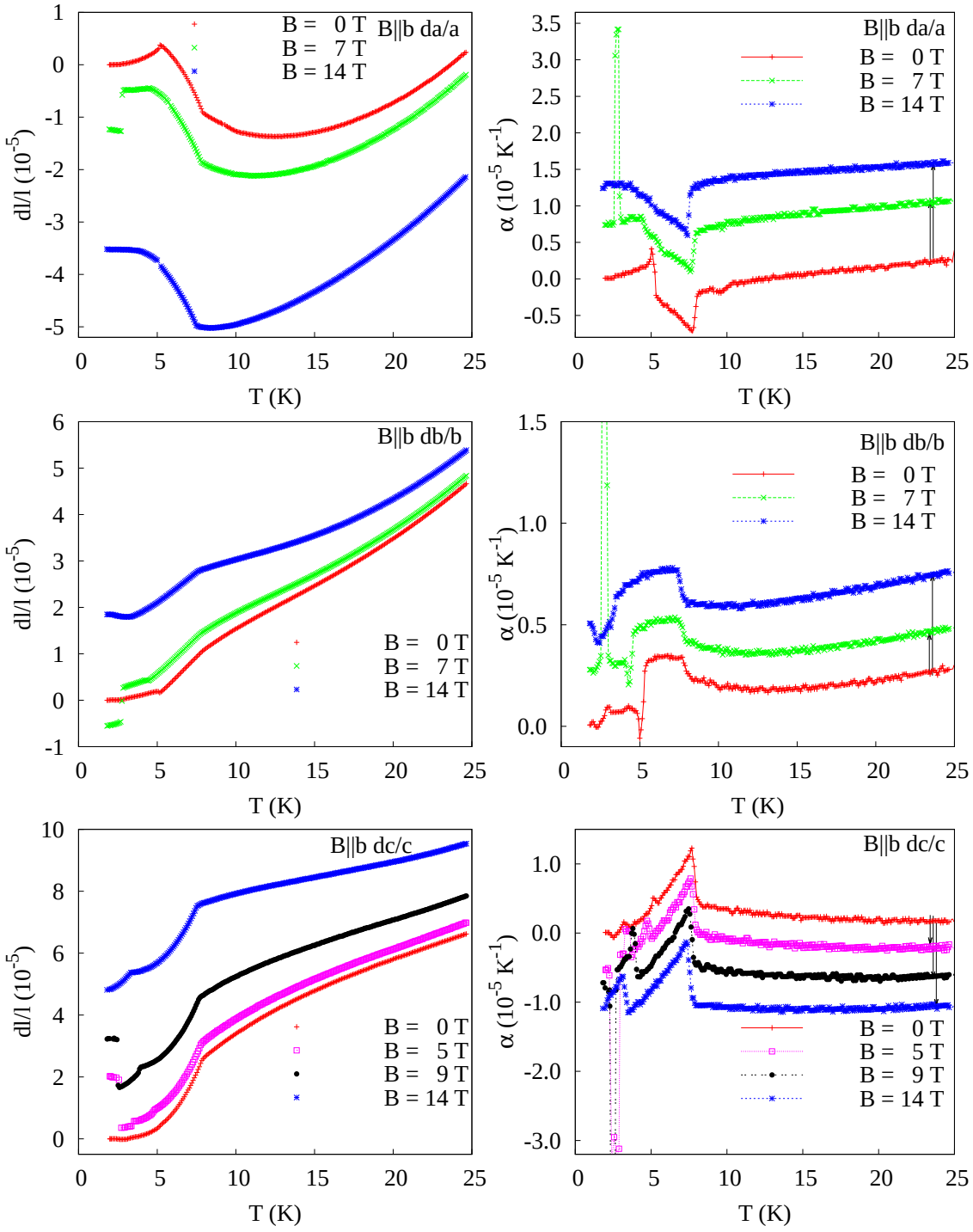

Figure 4.14: Temperature dependence of the thermal expansion (left) measured along the main crystallographic axes for $B \| b$-axis. For each geometrical configuration only well separated curves or the ones with different behaviour are shown for clarity. The corresponding α dependencies are depicted in the right column (dependencies in fields are shifted as denoted by arrows). See Fig. 4.12 for other longitudinal measurements.

			direction of magnetic field		
			a	b	c
$\frac{dx}{x}$	a	TE MS	$0, 2, 7, 14\,\mathrm{T}$ $1.8, 15\,\mathrm{K}$	$0, 1, 2, 3, 7, 8, 14\,\mathrm{T}$ $2, 25\,\mathrm{K}, \sharp$	$\times$
	b	TE MS	$\times$	$0, 1, 3, 5, 6, 7, 8, 9, 14\,\mathrm{T}$ $2, 14\,\mathrm{K}, \sharp$	$\times$
	c	TE MS	$\times$	$0, 1, 3, 5, 7, 8, 9, 14\,\mathrm{T}$ $1.8, 25\,\mathrm{K}, \sharp$	$0, 4, 7.5, 9, 14\,\mathrm{T}$ $2, 5.5, 7\,\mathrm{K}$

Table 4.2: List of performed experiments on the CePtSn sample. The temperature scans were done in the $2 - 25(8)\,\mathrm{K}$ interval, the magnetostriction curves were measured in the range $0 - 14(-0)\,\mathrm{T}$. The $\sharp$ denotes the full magnetostriction scan (see Fig. 4.17). Additional short scans were performed in the case $\frac{dx}{x} \| a, B \| b$, see Fig. 4.13.

Thermal expansion measured in longitudinal geometry

As expected from literature, there were no significant changes of the ordering temperatures with field applied along the c-axis. The T_N transition reflects itself in the $\left\{\frac{\Delta l}{l}\right\}$ dependency as a pronounced downturn whereas the T_t related anomaly is clearly visible only on the $\alpha(T)$ dependency as a small peak (see Fig. 4.12). Above T_N the $\alpha(T)$ is decreasing which reflects itself as an additional bow-like feature centred above T_N which is partially suppressed with applied field.

The transition temperatures and fields obtained from the investigation of the magnetostriction and thermal expansion in the longitudinal geometry for the field applied along the a-axis fit (see Fig. 4.13) to the previously obtained magnetic phase diagram (e.g. [159]). Both the T_N and T_t related anomalies are clearly visible as an upturn in the behaviour, above the T_N the a-axis continues to shrink and form a shallow minimum at $\approx 12\,\mathrm{K}$. This feature is reinforced with the applied magnetic field and the minimum is shifted to higher temperatures.

The thermal expansion measured along the b-axis in zero field reflects both transition temperatures (see Fig. 4.14), the T_t related anomaly is a small depression $(5 \cdot 10^{-7})$ followed by a linear increase up to T_N where an upturn occurs. With increasing field the T_N related feature remains intact in the shape and position, as expected, and the T_t transition is moved to lower temperatures (see Fig. 4.13).

The overall volume change ($\frac{dV}{V} = \sum_x \frac{dx}{x}$) as well as the corresponding $\alpha_V(T) = \sum_x \alpha_x(T)$ are depicted on the Fig. 4.15. The distinctive temperature dependencies for the a-axis and c-axis compensate each other in the region $(T_\mathrm{t}, T_\mathrm{N})$ as well as the opposite contributions above T_N and as a result the overall temperature dependency of $\frac{dV}{V}(T)$ is monotonous with two similar minor inflections at T_t and T_N.

Thermal expansion measured for field applied along the b-axis

With the application of the magnetic field along the b-axis, a new magnetic phase transition emerges for fields above $\approx 4\,\mathrm{T}$. The step like feature is present for all

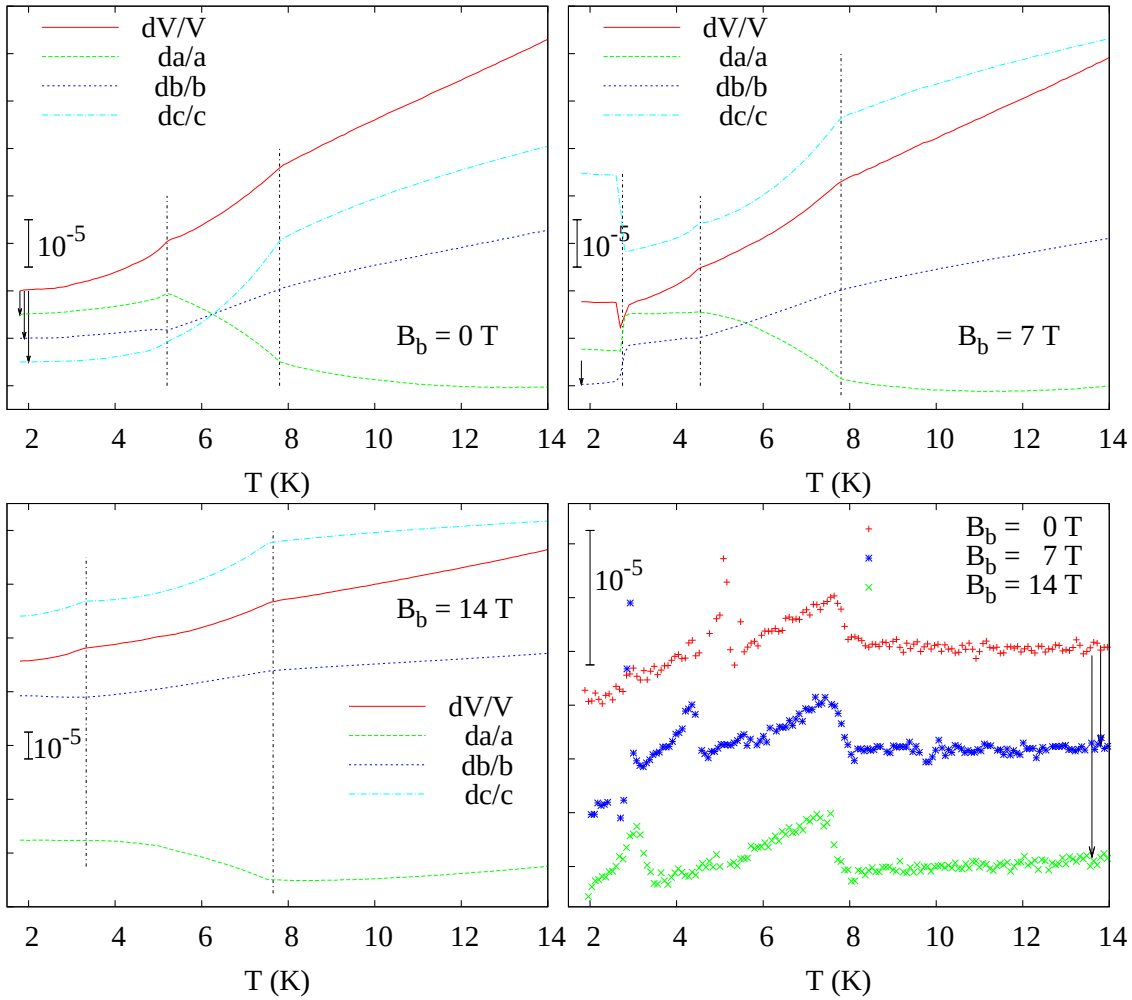

Figure 4.15: Temperature dependence of the volume expansion of the CePtSn sample for fields applied along the b-axis. The vertical lines indicate the transition temperatures as determined from the linear thermal expansion coefficient ($\alpha = \alpha_a + + \alpha_b + \alpha_c$, see bottom right figure).

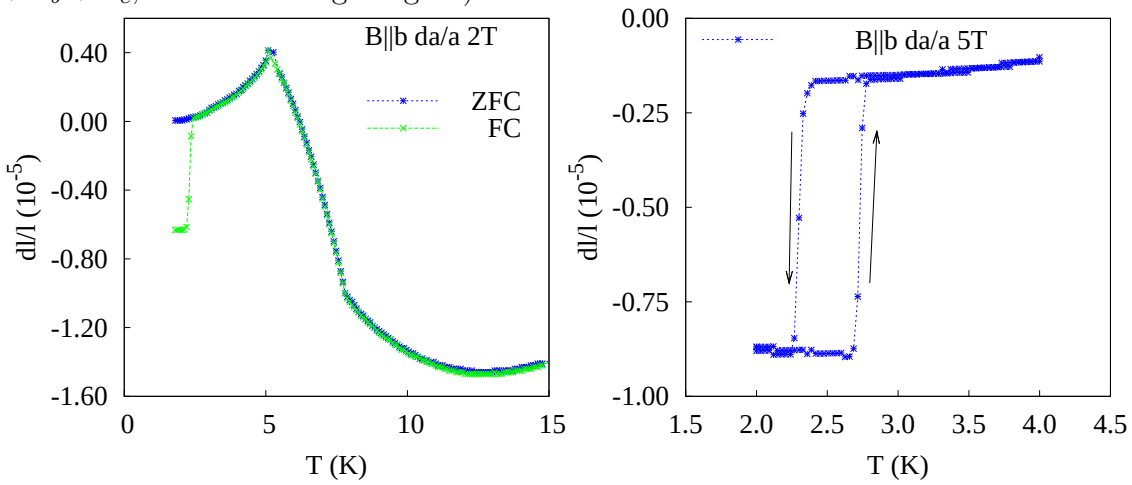

Figure 4.16: On the left side the difference between zero field cooled state and field cooled state is shown for magnetic fields applied along the b-axis. The right figure shows the hysteresis connected with the transition at 2.5 K measured at the magnetic field of 5 T applied along the b-axis. In this case the cooling/heating rate was 0.025 Kmin^{-1}.

crystallographic axes, its size (at 7 T) is $7.9 \cdot 10^{-6}, 7.3 \cdot 10^{-6}$ and $-16.0 \cdot 10^{-6}$ for a, b and c direction, respectively, yielding almost no total volume change ($0.8 \cdot 10^{-6}$). This transition has significant hysteresis (0.4 K at 5 T, see Fig. 4.16 with the result from measurement along the a-axis[8]). Similarly to the 0 T case the monotonous evolution of the overall volume expansion is interrupted only by minor upturns at T_t and T_N and a significant dip at 3 K (Fig. 4.15). For fields above 12 T only two transition are observed in agreement with the magnetic phase diagram. The application of the magnetic field along the b-axis has notable effect on the evolution of the a-axis and c-axis dependencies, causing much faster vanishing of the deviation from the Debye character above T_N (in comparison to the longitudinal results).

For the fields applied along this axis also the magnetic history phenomena arise — the value of the thermal expansion measured for fields below 4 T and temperatures below 2.3 K depends on the used path in the $B - T$ space, leading i.e. to the significant differences in the thermal expansion between the zero field cooled state and field cooled state (see later discussion in the magnetostriction subsection). In the field cooled state a first order transition is observed on the border of sample history dependent area (see the data (Fig. 4.13) for the thermal expansion measured along the a-axis).

In the context of the pressure experiment which was done for CePtSn [161] it is worth to estimate the pressure dependence of ordering temperatures, based on the extrapolation from elastic data. The shift of the Néel temperature T_N is in the case of second order phase transition related to the uniaxial pressure p_x change applied along the axes x by the Ehrenfest relation 3.3 (see p. 38).

The obtained estimations are summarised in the Table 4.3. The predicted value for the change with the hydrostatic pressure is very low, in good agreement with the observation of indifference of the transition up to pressure 0.9 GPa [161]. For the calculation the values $\Delta c_p = -4\,\mathrm{Jmol^{-1}K^{-1}}$ [153] and $V_M = 41.6\,\mathrm{cm^3mol^{-1}}$ were used.

x	$\Delta\alpha_x$ 10^{-6} K	$\frac{dT_N}{dp_x}$ K GPa^{-1}
a	5.7	0.47
b	-1.0	-0.08
c	-8.0	-0.66
V	-3.8	-0.3

Table 4.3: Estimated T_N pressure dependence. See details in the text.

A similar estimation may be made for the pressure dependence of T_t . However in this case the $\alpha(T)$ dependency has attributes of the first order transition, therefore the Clausius–Clapeyron Eq. 3.2 (see p. 37) is used. The estimation of the ΔS from the specific heat data [153] leads to finite value $\approx 0.2\,\mathrm{Jmol^{-1}K^{-2}}$ whereas the $\Delta\left\{\frac{\Delta l}{l}\right\}_x$ are very small values in the units of 10^{-7} leading to even weaker pressure dependence (approx. one order smaller than in the T_N case).

This estimation can be compared with the evolution of the ordering in the isostructural system $CePt_{1-x}Ni_xSn$, where the suppression of the ordering is observed with increasing Ni content. The transition from CePtSn to CeNiSn is con-

[8] In order to avoid possible instrumental effect the sweep rate was set to 25 mKmin^{-1}. This speed should be sufficiently low for proper thermalisation — similar experiment was done at 2 T magnetic field with sweep rate 50 mKmin^{-1} and no shift between heating and cooling curves was observed at the T_t and T_N related anomalies (for the data points measured every 0.08 K).

nected [162], [163], [150] with slight expansion ($\sim 1\,\%$) along the *a*-axis and contraction in the perpendicular plane ($\sim 1\,\%$ and $\sim 5\,\%$). If the relative change of the lattice parameters is coupled with the change of a (virtual) pressure induced by substitution through the compressibility

$$\kappa_T = -\frac{\Delta V}{V}\frac{1}{\Delta p} \tag{4.1}$$

then it can be seen that the individual contributions are added (and not cancelled as in the case of hydrostatic pressure) causing the suppression of the ordering with increasing the Ni content. In agreement with expectations (one order of magnitude lower $\frac{\mathrm{d}T_\mathrm{t}}{\mathrm{d}p_x}$ values) the T_t value remains almost intact with increasing Ni content.

This qualitative discussion supports the idea [161] based on the unexpected results from the experiments for the compound under hydrostatic pressure, that not the unit volume cell but the Ce – Ce distance governs the hybridisation strength.

4.3.3 Magnetostriction

The longitudinal magnetostriction measured (for temperatures see Table 4.2) for the field applied along the *a*-axis and *c*-axis, respectively, does not show any signs of a field induced transition. This is the expected behaviour for the field applied along the *c*-axis which is a hard axis and no significant evolution of the magnetic phase diagram with increasing field was reported. However this is not the case for the magnetic field applied along the *a*-axis where a field induced transition should occurs at $\sim 12\,\mathrm{T}$. Nevertheless, the phase border is rather close, the scan over temperature cross it at 3 K and is reflected as weak bump.

Much more complex situation was found for fields applied along the *b*-axis (see Fig. 4.17). In agreement with the proposed magnetic phase diagram two field induced transitions were observed at 2 K, at 4 T and 10.8 T, respectively, both first order, the upper one is accompanied by the 0.1 T hysteresis. The low field transition is accompanied by the *c*-axis expansion and contraction in the perpendicular plane, whereas the high field transition behaves in the opposite way. The overall volume change is very small ($3 \cdot 10^{-6}$ and $5 \cdot 10^{-6}$, respectively) and positive in both cases.

The low-field transition is on the border of the sample history dependent area and therefore interesting phenomena are connected with this transition. First of all it is not possible to get back to the zero field cooled state by pure cycling the magnetic field (without temperature change, see Fig. 4.17), the change of dimensions during decreasing magnetic field in is only one half of the change associated with the original field up 4 T transition. The original state may be regained by heating above $\sim 3\,\mathrm{K}$ and cooling back. Secondly, starting from the field cooled state the "4 T" transition is shifted to slightly lower fields (3.8 T) and accompanied by a huge ($> 4\,\mathrm{T}$) hysteresis — the zero field (FC) state is recovered for the field of $\sim 0.3\,\mathrm{T}$ applied in the opposite direction. The highest remanent magnetostriction is observed for the *b*-axis with the value of $\sim 2 \cdot 10^{-6}$ in the other two direction the remanent magnetostriction is approx. one order of magnitude lower ($3 \cdot 10^{-7}$ and $2 \cdot 10^{-7}$ for

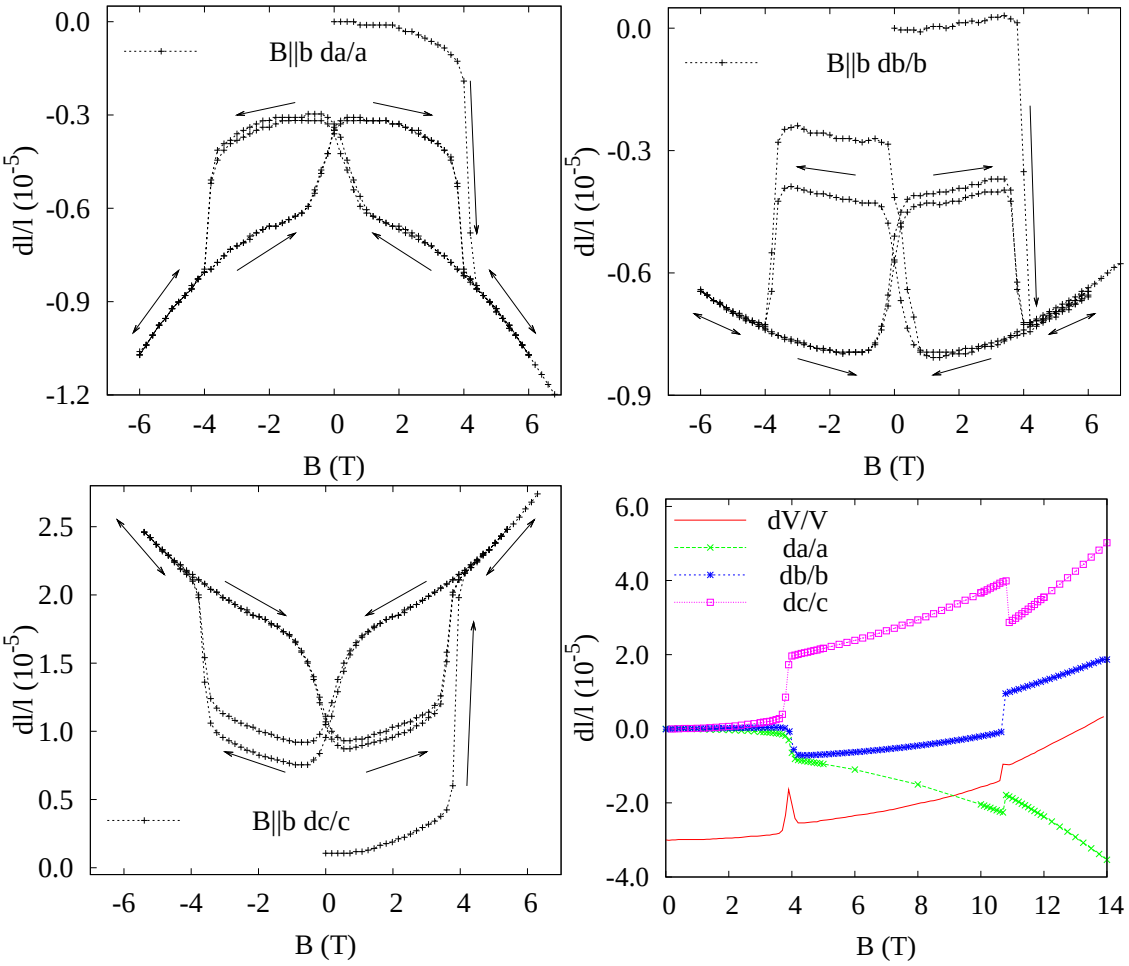

Figure 4.17: Magnetostriction measured along the principal axes of the CePtSn sample at 1.8 K* for the field applied along the *b*-axis. The lines indicate the evolution of the magnetic history of the sample.
*measurement along *c*-axis was done at 1.95 K

the *a* and *c* directions respectively). This measurement was repeated at 2.5 K and no anomaly was observed.

4.3.4 Resistivity

In order to exclude hypothetical instrumental effects and their influence on the partial recovery of the irreversible phase the resistivity measurement on the same sample was performed.[9]

The longitudinal geometry was used, the magnetic field was applied along the *b*-axis. The temperature dependence of the electrical resistivity is in agreement with previously published data. The magnetoresistivity curve was measured at 1.8 K and

[9]The resistivity was chosen due to the large influence of the 4 T transition on the transport properties, contrary to the negligible and almost unidentifiable effect on the magnetisation.

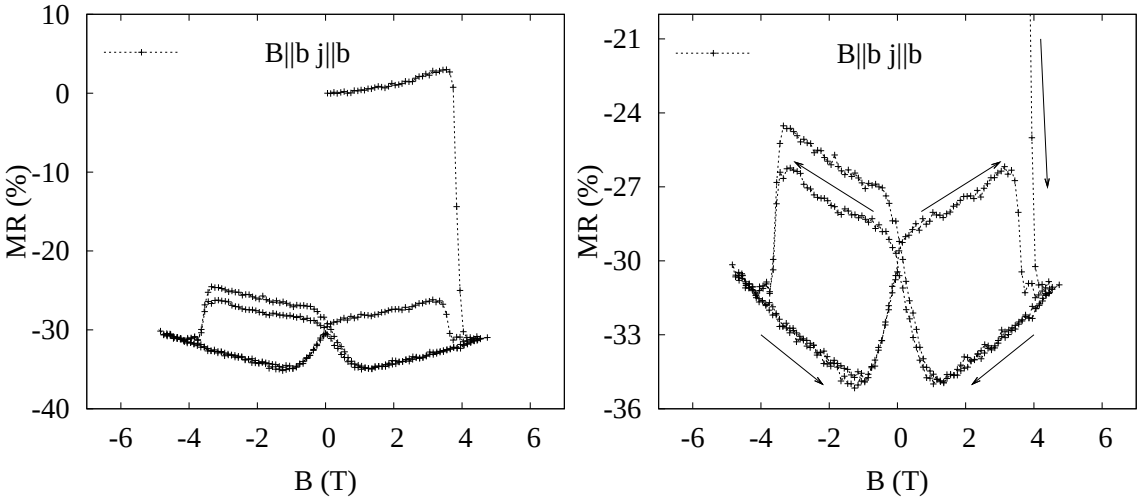

Figure 4.18: Magnetoresistance of the CePtSn sample at 1.8 K for field applied along the *b*-axis in longitudinal geometry. The lines indicate the evolution of the magnetic history of the sample.

the obtained data are presented in the Fig. 4.18. The sample was cooled down in zero magnetic field, after first application of magnetic field the crossing of the 4 T transition is accompanied by the 30% drop of the magnetoresistance (in agreement with previous reports, eg. [160]). With subsequent magnetic field cycling the same phenomena as in the magnetostriction curve is observed (i.e. partial restoration of the zero field cooled properties, including the difference between the first and second field sweep with the opposite field direction). Similarly to the magnetostriction data, the transition field is lower and six times smaller effect is observed across the transition.

These results definitely confirm the observations based on the magnetostriction measurements, however the microscopic origin is still unclear and the extension of the neutron study [160] is necessary.

4.3.5 Conclusions

The temperature and field dependencies of all interesting elements of the elastic tensor were determined. The closer investigation of the irreversible phase (zero field cooled state below 4 T and 3 K) by the magnetostriction and electrical resistivity indicate that potentionally a partial restoration of irreversible phase may occur for field applied in the opposite direction, however neutron diffraction experiment is necessary to confirm this hypothesis.

The analysis of the thermal expansion anomalies and the estimation of the behaviour under applied external pressure are in agreement with previously done hydrostatic pressure experiments [161] and behaviour in the isostructural system $CePt_{1-x}Ni_xSn$ ([162], [163] and [150]) and supports the proposed idea [161] about the importance of the Ce–Ce distance governing the hybridisation strength.

4.4 $PrCo_2Ge_2$

The family of RT_2X_2 compounds is one of the largest among ternary systems. In these ternary intermetallics a large variety of physical properties have been observed covering also interesting phenomena like mixed valence materials, heavy fermions, dense Kondo behaviour and superconductivity. One of the most prominent properties is the strong magnetocrystalline anisotropy usually confining the R magnetic moments along the c-axis and leaving the magnetisation along the directions within the basal plane to mimic paramagnetic behaviour irrespective to the type of magnetic ordering.

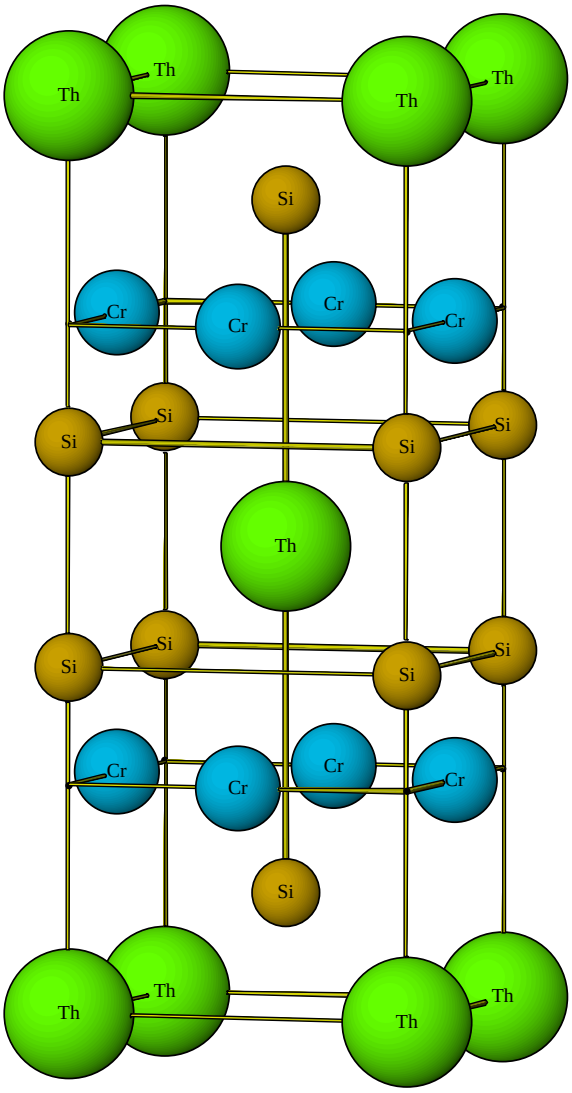

Figure 4.19: Body centred tetragonal $ThCr_2Si_2$-type structure

4.4.1 Crystal Structure and previous results

Majority of these rare-earth transition-metal silicides and germanides crystallise in the body centred tetragonal $ThCr_2Si_2$-type structure (space group I4/mmm, D_{4h}^{17}, firstly reported for $ThCr_2Si_2$ [164] and independently for $CaAl_2Ga_2$ [165]), which is $BaAl_4$-type derivative [166].[10] This structure can be described as layers of atoms of the same kind $(R-T-X-T)$ stacked along the tetragonal axis. Physical, especially magnetic, properties of these compounds reflect the layered character of this structure.

The structural [168] and magnetic [169] properties of RCo_2Ge_2 have been studied systematically first in the early 70's. The powder sample of $PrCo_2Ge_2$ involved in this study was found to be tetragonal (for the details concerning crystal structure see section 4.4.1) and exhibits a peak in susceptibility at 28 K with the susceptibility rising with decreasing temperature. The Néel temperature was however determined to be $T_N = 13.3$ K. Magnetic structure was determined few years later by powder neutron diffraction [170]. The analysis confirms the crystallographic structure

[10] Some of the RT_2Ge_2 compounds crystallise in the $CaBe_2Ge_2$ [167] which is $BaAl_4$-type derivative, too. However, there is lack of the mirror symmetry about the Ca containing plane.

previously reported and determined magnetic structure as antiferromagnetic with moments only in the Pr sublattice (mag. moment $3.7 \pm 0.3\,\mu_B$ per Pr atom) characterised by the propagation vector (0, 0, 0.73) and moment direction along the c-axis. No anomaly on the magnetisation curves measured on the polycrystalline sample was found [171] at 4.2 K in fields up to 14 T.

The neighbouring compound, $PrCo_2Si_2$, was studied in more details by different groups e.g. [172], [173] and [174]. The observed (eg. [175], [176]) large anisotropy makes the study of polycrystalline study more or less worthless for the detailed investigation of bulk properties. Therefore only results based on mainly microscopic or bulk single-crystal experiments are summarised.

The compound undergoes three subsequent transitions at temperatures 9 K, 17 K and 30 K, respectively, as determined from the temperature dependence of magnetisation [176], resistivity [175] and specific heat [174], [177]. The measurement of the magnetisation at low temperatures [175], [176] and [178] with respect to a magnetic field (applied along the c-axis) reveal step-like approach to the saturated value of $3.2\,\mu_B$ observed at 1.3 K and fields above 14 T. The critical fields are 1.2 T, 3.8 T, 6.7 T and 12.2 T. The response to the field application along the a-axis is linear and reaching only $\sim 0.5\,\mu_B$ at 30 T. The magnetic structure was determined by powder [172] and single-crystal [179], [173] neutron diffraction. The transition temperatures were found to be in agreement with bulk studies, the individual phases were identified as long period commensurate antiferromagnetic, with magnetic moments only on the Pr atoms coupled ferromagnetically in the a-a plane and antiferromagnetically along the c-axis. The propagation vectors were found to be $(0, 0, 1)$ for the temperatures below 9 K, $(0, 0, \frac{25}{27})$ for $9\,\mathrm{K} < T < 17\,\mathrm{K}$ and $(0, 0, \frac{21}{27})$ for $17\,\mathrm{K} < T < 30\,\mathrm{K}$. The neutron diffraction done in the fields up to 15 T [173] reveals only three different magnetic structures, no change in magnetic structure which can be attributed to the anomaly at 3.8 T was observed. Recently there was published a slight revision [180] of the magnetic phase diagram based on the resistivity and magnetisation data, clarifying the temperature dependence of phase boundary connected with the 6.7 K transition in low temperatures.

4.4.2 Magnetic and thermodynamic properties

The temperature dependence of magnetisation at various fields is depicted in Fig. 4.20. In agreement with the literature data the temperature dependence of magnetisation at low fields ($< 4\,\mathrm{T}$) shows one maximum at $T_N \sim 28\,\mathrm{K}$ followed by increase with decreasing temperature. The maximum is shifted to low temperatures with increasing the magnetic field as it is expected for the antiferromagnetic type of interaction. With increasing the value of the magnetic moment in paramagnetic region the character of temperature dependence of magnetisation is changed at $B \sim 7\,\mathrm{T}$ to the peak shaped maximum, with almost the same magnetisation at low temperatures as low field dependencies. This behaviour is violated at $B \sim 9\,\mathrm{T}$ by change in the low temperature value of magnetisation suggesting a possible field induced transition to state with a higher magnetic moment.

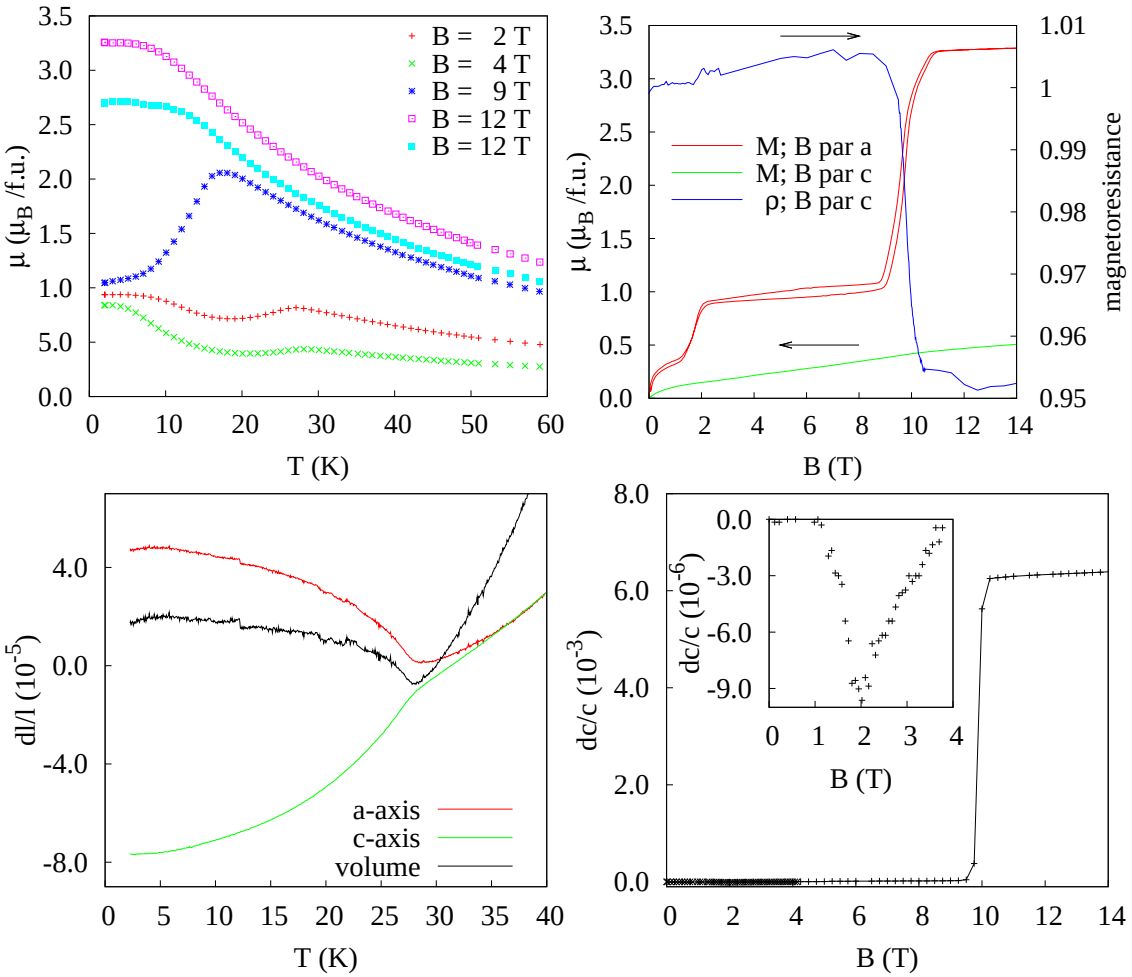

Figure 4.20: $PrCo_2Ge_2$: Temperature dependence of magnetisation (field applied along the c-axis) and thermal expansion as a function of temperature (left). Magnetisation, magnetoresistance and magnetostriction as a function of magnetic field (right).

The temperature dependence of the AC susceptibility clearly indicates two transitions, one in the vicinity of 28 K and the second one below 10 K.

The field dependence of magnetisation for field applied along the c-axis is shown in Fig. 4.20, distinctly indicating two field induced transitions — at 2 T and 10 T. The saturated magnetic moment value reaches 3.29 μ_B (at 2 K), which can be understood in terms of a moment of a Pr^{3+} plus a contribution of conduction electrons. There is a small ferromagnetic contribution ($\sim$ 0.2 μ_B at 2 K) indicating an additional ferromagnetic component in the ordered state. There is only the paramagnetic like response observed for the field applied in the basal plane.

The temperature dependence of the specific heat measured at various magnetic fields applied along the c-axis (Fig. 4.21) confirms the above outlined scenario. The data measured without application of magnetic field show a T_N related anomaly as

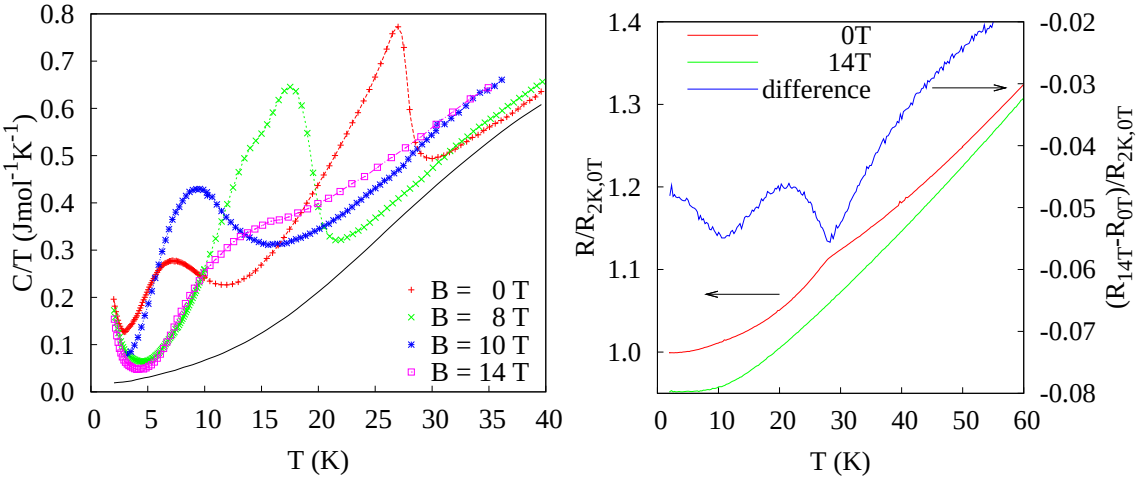

Figure 4.21: Left panel: Temperature dependence of specific heat of the $PrCo_2Ge_2$ in magnetic fields applied along the c-axis. The data from non magnetic analogue ($LaCo_2Ge_2$) are denoted by line. Right panel: Temperature dependence of electrical resistivity of the $PrCo_2Ge_2$ in magnetic fields applied along the c-axis.

a sharp peak, whereas a second transition is reflected as a broad bump at $T_t \sim 8\,K$. The evolution within application of magnetic field follows the evolution of magnetisation — the T_N related anomaly is shifted to lower temperatures and at $\sim 8\,T$ merges with the low temperature anomaly. For the fields above 10 T only a wide bump is observed which is almost suppressed in the 14 T field. The residual bump on the 14 T curve is originated by the Schottky type contribution due to the CF splitting of the Pr ion ground state multiplet. With the application of the magnetic field the ground state degeneracy is lifted and the CF level scheme is modified. As a consequence, the specific heat data exhibit wide-range anomalies also in the field induced ferromagnetic state.

4.4.3 Elastic and transport properties

We measured the temperature dependence of electrical resistivity (RRR $\sim$ 3.3) as well as the magnetoresistance for the current along the c-axis with field applied both in the transversal and the longitudinal geometry, respectively. The temperature dependence of the resistivity without application of the magnetic field in shown in Fig. 4.21. The T_N reflects itself as a significant change in the temperature dependence whereas T_t is visible only in the derivative or as a change in the character of magnetic contribution to the total resistivity.[11] Both the transitions are clearly visible if we subtract the 0 T and longitudinal 14 T curve (where no transition was observed). In the transversal geometry the applied of 14 T magnetic field has no influence on the temperature dependency. The magnetoresistance curve for the longitudinal

[11] Assuming the $R \sim T^x$ behaviour for the magnetic contribution, the low temperature ($T < 8\,K$) part is described by $x = 3.1$ whereas the phase $10\,K < T < 25\,K$ fits to $x = 2.3$.

T(K)	N_o	N_{sp}	$\mathbf{q}_0^{\dagger}$	N_{refl}	N_{ex}^{20}	$\sum$	$q_z^{\star}$	$\sum'$
2.5 K	4	220	(0.01, 0.01, 0.74)	155	30	10.13	0.733	9.98
13.0 K	3	149	(0.01, 0.01, 0.74)	109	5	9.94	0.734	8.20

Table 4.4: Parameters obtained from the propagation vector determination routines. In the second part of the table the results from subsequent utilisation of the Monte Carlo method are summarised. For the symbols meaning see the caption of the table 3.2, page 61. Due to the larger spot size, the cut off value for the rejection of the misindexed reflections was set to 20 pixels.
† The minimum bin size was 0.02, therefore the error estimation is 0.01 and the lowest possible value is 0.01.
* The q_x, q_y components were in later runs smaller than 10^{-4} and therefore treated as zero.

geometry is shown in the Fig. 4.20. The 10 T field induced transition is accompanied by the 5 % drop in resistivity, however no clear indication was seen for the 2 T transition.

The results of the thermal expansion and the magnetostriction measurements are shown in Fig. 4.20. At T_N there is a significant deviance from the Debye-like behaviour for the measurement along both principal axes. There is no visible anomaly on the $\left\{\frac{\Delta l}{l}\right\}$ curve in the vicinity of the T_t temperature, this anomaly reflects itself as a slight upturn in the temperature dependence of the α coefficient. The magnetostriction measured for the field applied along the c-axis in the longitudinal geometry shows both field induced transitions, the 10 T one is accompanied by a 0.6 % change in the linear dimension.

4.4.4 Magnetic structure determination

The magnetic structure was determined using the VIVALDI white beam Laue diffractometer. The Laue patterns taken at several temperatures show appearance of magnetic satellites for temperature below T_N as well as additional spots below T_t (see Fig. 4.23 and 4.24). Closer inspection (for details see section 3.6.3 and Table 4.4) of patterns taken for several crystal orientations at temperatures between T_t and T_N indicate that all satellites can be indexed with one magnetic propagation vector (0, 0, 0.733(1)) in good agreement with the original powder experiment [170].[12]

The additional spots appearing below T_t were identified as third order satellites (see Fig. 4.22) of the (0, 0, 0.733) propagation vector. The appearance of the third order satellites allows in principle more precise determination of the propagation vector, in this case the detailed inspection of positions of third order satellites on the Laue pattern is in excellent agreement with the previous application of automatic routines using large number of first order satellites. The temperature evolution of the intensity of the higher order satellites is well correlated with the appearance

[12] Alternatively, this propagation vector can be described as medium periodicity commensurate structure $(0, 0, \frac{11}{15})$.

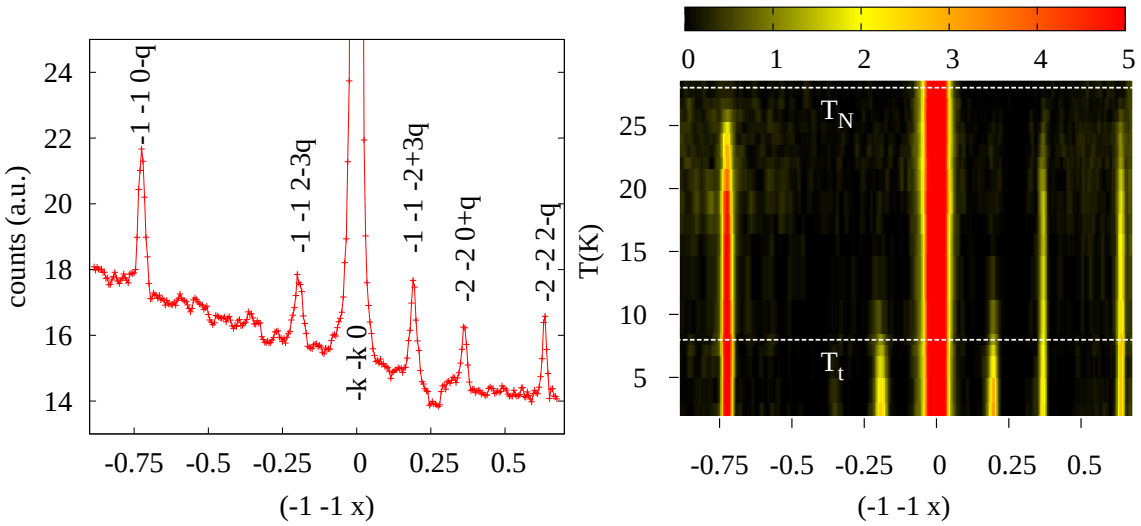

Figure 4.22: Indexed linear cut from the Laue pattern at one selected orientation at temperature 1.8 K (left) and its evolution with temperature (right).

of the anomalies (if observed) in the bulk properties. The observation of the third order satellites (no fifth and higher order satellites were observed) indicate partial squaring up of the magnetic structure.

The propagation vector is temperature independent as can be seen from the temperature evolution of the linear cut from the Laue pattern taken for one fixed orientation at several temperatures (Fig. 4.22).

The magnetic extinction rules indicate a possible direction of the magnetic moment the *c*-axis direction, in agreement with the results of the bulk magnetic measurements and significantly extend results from previously published neutron diffraction experiment [170]. The evaluation of integrated intensities in order to obtain the direction and magnitude of magnetic moments, which is beyond the scope of this thesis, is in progress.

4.4.5 Conclusions

The detailed investigation of the bulk and microscopic properties of $PrCo_2Ge_2$ single crystal sample revealed the same magnetic structure as proposed in earlier studies on the polycrystalline sample ([169], [168] and [171]) or from the powder neutron diffraction experiment [170]. However, a new order-to-order transition was found and identified as partial squaring up of the magnetic structure.

The bulk measurement revealed huge anisotropy, with two field-induced transitions for field applied along the easy axis of the system, the *c*-axis. The second one at 10 T is accompanied by a significant magnetoresponsive effect, namely the large magnetoresistivity ($\sim 5\%$) and magnetostriction (0.6%).

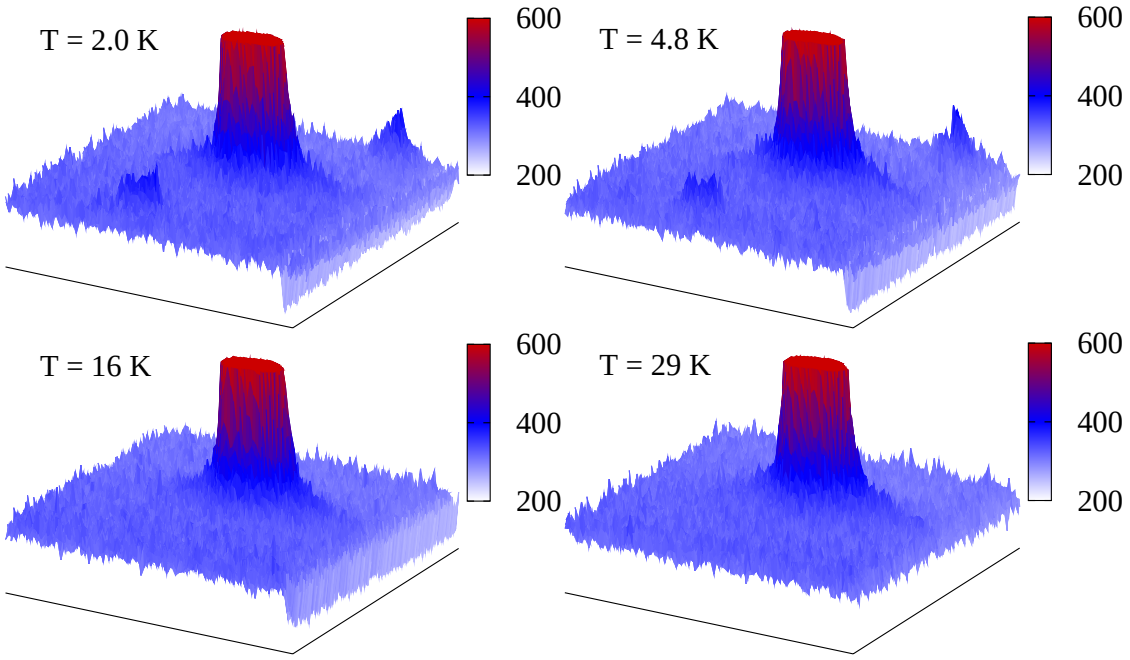

Figure 4.23: $PrCo_2Ge_2$: Temperature dependence of selected area from the Laue pattern taken at given crystal orientation. The $kk0$ nuclear reflection and two third order satellites are visible at lowest temperature. For the indexation see the cut on the Fig. 4.22, which is going through this selection.

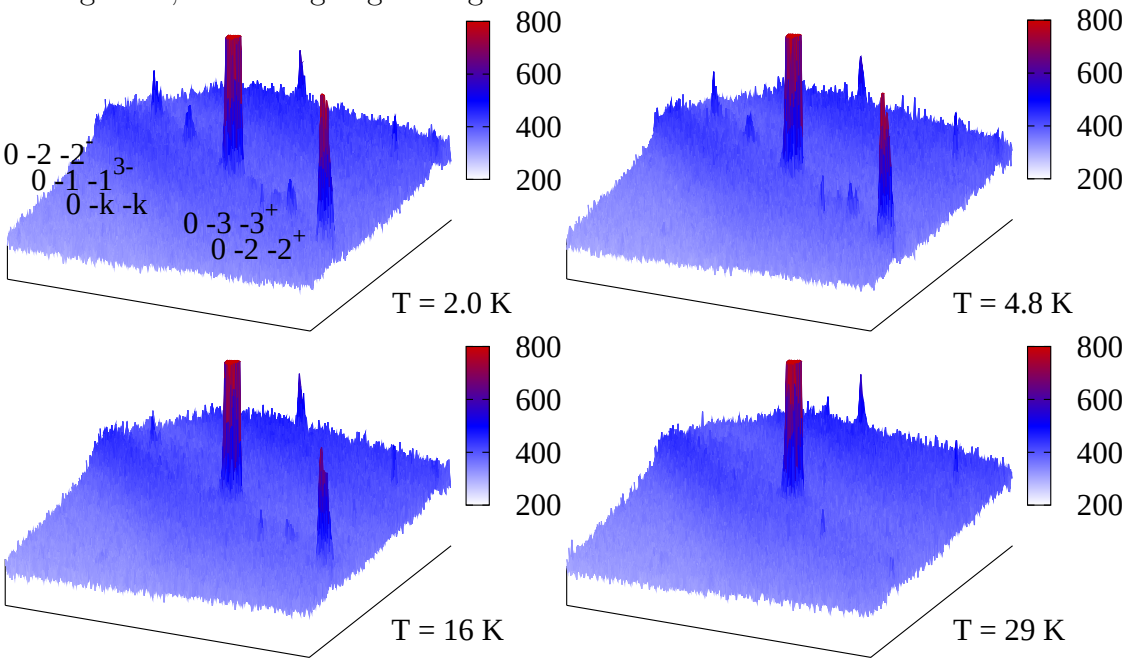

Figure 4.24: $PrCo_2Ge_2$: Temperature dependence of selected area from the Laue pattern taken at given crystal orientation. Subsequent disappearance of several first and third order satellites is notable.

Chapter 5

Summary and conclusions

The results in this thesis fall into two categories with respect to the methodology of the investigation of physics of intermetallic compounds.

Firstly, the microdilatometric capacitance cell [82], allowing very sensitive measurements of elastic properties and removing strong sensitivity to the sample surface quality when using strain gauges, was implemented to the PPMS apparatus in the Joint Laboratory for Magnetic Studies (see section 3.5) and necessary programs for the experiment control, data logging and evaluation were written. The calibration procedure was performed and check against the Cu standard in order to verify the correct functionality of the setup. Note that to our best knowledge this was the first implementation of the microdilatometric cell to the PPMS in the World. The cell was intensively exploited for studying elastic and cohesive properties of single crystals of several f-electron intermetallics representing very interesting aspects of physics of strongly correlated electron materials. The results obtained in this thesis were compared with available literature data (e.g. for UCoAl).

During the author's stay at Institut Laue-Langevin a set of routines aimed at the evaluation of complicated magnetic structures using the VIVALDI instrument have been written (see section 3.6.3). More specifically, two routines for more or less automatic magnetic propagation vector determination were produced, allowing estimation of the propagation vector based on the geometrical considerations and Monte Carlo method. Several supporting routines allowing subsequent integration or Laue pattern simulation were written, too. The synthetic tests show a very good reliability of these routines, especially for higher number of independent magnetic satellites.

These routines were applied by the author for determination of some magnetic structures for the purposes of this thesis. Nevertheless, the main impact of author's work at ILL consists in availability of the routines for a wide community of ILL users, who were so far suffering from the lack of reasonable methodology and software allowing magnetic structure determination from complex but extremely valuable data received at VIVALDI.

Besides the dilatometric experiments, the physical properties of several compound were studied in detail in this thesis and they were discussed with respect

to physics of the studied materials. Due to the notable anisotropy in all studied compounds, only single crystal samples were used.

Through investigation of the influence of the spin fluctuation phenomena on the elastic properties of uranium UTAl compounds have been made, showing very good agreement with the so far available experimental findings received by various methods ([119], [133]). The thermal expansion measurements of these materials without magnetic field and in magnetic field applied along the c-axis clearly demonstrate the surviving influence of the strongly anisotropic spin fluctuations well above the characteristic temperatures.

The next studied compound, NdRhSn, was chosen because of the outlasting discrepancies in the literature (reporting e.g. superconductivity [142] and the double phase transition [144]) observed in the early stages of this study. The studies of elastic properties confirm two phase transitions where the intermediate phase is suppressed by applying a small magnetic field. This effect is accompanied by a step like change of the magnetostriction. In order to clarify these phenomena by microscopic methods a neutron scattering experiment was performed. The analysis of the data obtained from the experiments on the VIVALDI diffractometer reveals two magnetic phase transitions, the low temperature phase has the same size of the magnetic and crystallographic unit cell, whereas the intermediate magnetic phase has a propagation vector indicating eleven times larger magnetic unit cell along the c-axis.

The most thoroughly studied compound by means measuring elastic properties in this thesis was CePtSn [159]. The rather low symmetry of the crystal structure and the strong anisotropy of magnetic and other electronic properties make this compound an ideal candidate for the investigation of the complete temperature and field dependence of the elastic tensor. Therefore the temperature and field dependencies of the majority of the elastic tensor elements have been determined. The quantities characterising the effect accompanying the transitions were used for testing the response on applied hydrostatic pressure. The results of the tests are in good agreement with the previously published pressure experiment. One step further is the estimation of the behaviour of the isostructural system $CePt_{1-x}Ni_xSn$ using the change of (virtual) pressure (connected through compressibility). These estimations are in good agreement with behaviour reported in this system, too.

The last system studied in detail in this thesis is $PrCo_2Ge_2$, the strongly anisotropic compound with a field induced transition accompanied by strong magnetoresposive phenomena — 5% decrease of the resistance and 0.6% change of magnetostriction. Contrary to previous studies ([169], [170]) the second low-temperature transition was found in the majority of studied properties. This transition was later identified by white neutron beam Laue diffraction as partial squaring up of the magnetic structure. The propagation vector determined for both the magnetic phases is in agreement with original powder neutron diffraction data [170].

Besides the compounds mentioned above and studied in details, there were several others studied only briefly as a part of a broader cooperation. Few of them

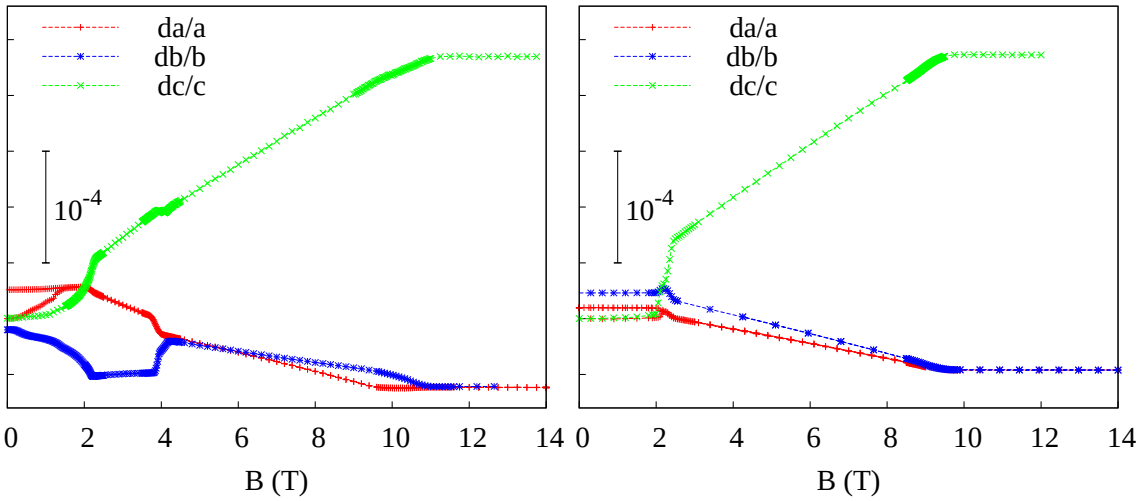

Figure 5.1: Magnetostriction of the $GdRu_2Si_2$ sample at 2 K for field applied along the *a*-axis (left panel) and *c*-axis (right panel).

are notable in within the context of this thesis. The first one is gadolinium based[1] tetragonal $GdRu_2Si_2$ ([181], [182]), one of the compounds whose elastic properties are recently investigated [183] in order to clarify the so-called Magnetoelastic paradox [184] and especially its lifting by small magnetic fields.[2] A field dependence of all important magnetostriction tensor elements at 2 K were measured in order to bring additional information about this compound and its elastic properties and the high sensitivity of the microdilatometric capacitance cell was used for clarification of the low resolution data from X–ray experiment. The obtained data (see Fig. 5.1) indicate the presence of the orthorhombic distortion in non-zero magnetic field as well as the small magnetocrystalline irreversibility. These data may be partially interpreted as a repopulation of crystallographic magnetic domains, however the data on magnetic domain population in this compound are not available yet.

Two other compounds crystallising in the tetragonal $ThCr_2Si_2$–type structure were studied, namely $PrRu_2Si_2$ and $PrRu_2Ge_2$ [185], where the measurements of the thermal expansion and magnetostriction were used as a tool for basic characterisation and mapping of the magnetic phase diagram. In these compounds only some of the elastic tensor elements were measured, because the fragility of the samples and strong anisotropy does not allow measurement in the direction perpendicular to the cleavage plane.

[1] The 4f shell is in the Gd case half-filled, i.e. its ground state, $^8S_{\frac{7}{2}}$, is insensitive to the crystalline electric field effect (CEF) due the missing orbital moment. Thus, neglecting CEF for Gd compounds, the variations of magnetic properties are driven purely by variations of exchange interactions.

[2] Formulation of the Magnetoelastic paradox, as stated in [184]: *In antiferromagnetic systems without orbital moment symmetry-breaking distortions below the Néel temperature are expected, but have not been found.*

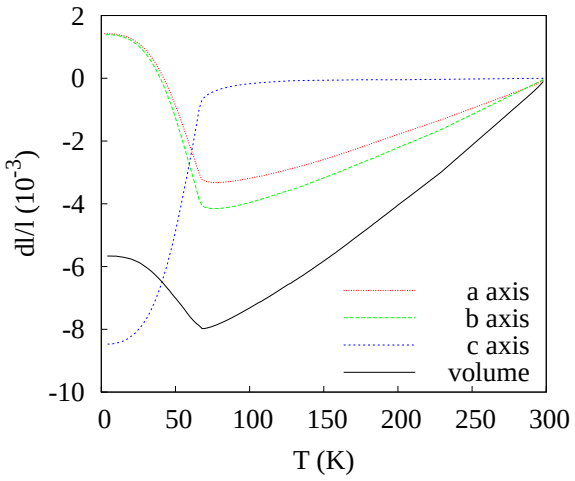

Figure 5.2: Temperature dependence of the thermal expansion measured along main crystallographic axes in the GdNi compound in zero magnetic field.

Notable results were also observed in the elastic properties of the GdNi compound [186], crystallising in the orthorhombic CrB–type structure, ordering ferromagnetically below $T_C = 69\,K$. The anomalous thermal expansion observed in the ferromagnetic state (see Fig. 5.2) is due to the large spontaneous magnetostriction caused by the anisotropy in magnetoelastic coupling.

In this thesis two important approaches to the investigation of the magnetism in intermetallic compounds were introduced and carefully tested.

Two routines for more or less automatic magnetic propagation vector determination were produced, allowing estimation of the propagation vector from Laue patterns, based on the geometrical considerations and Monte Carlo method. Several supporting routines allowing subsequent integration or Laue pattern simulation were written, too.

The microdilatometric cell was used for the investigation of the elastic properties of several chosen compounds, namely the influence of the spin fluctuations in the UCoAl and UNiAl and the phase ordering schemes in CePtSn, NdRhSn and $PrCo_2Ge_2$. The basic theory approaches, summarised in the Chapter 2 are not capable of treating the the spin fluctuation phenomena and its influence on the elastic properties, however basic theoretical approaches for static ordering are available (e.g. McPhase package [187], capable of magnetic structure stabilisation and calculation of magnetic properties, including elastic one) and their usage may indicate one of the possible future continuation of this work. The other one is a detail analysis of the obtained Laue patterns, including the determination of the moment magnitude and direction based on the reflection intensity evaluation.

Bibliography

[1] Kittel C. (1985) *Úvod do fyziky pevných látek* Academia, Praha

[2] Langevin P. (1905) *J. de Physique* **4** 678

[3] Weiss P. (1907) *J. de Physique* **6** 667

[4] Pauli W. (1927) *Z. Phys.* **41** 81

[5] Bloch F. (1929) *Z. Phys.* **57** 545

[6] Mott N. F. (1935) *Proc. Phys. Soc.* **47** 571

[7] Slater J. C. (1936) *Phys. Rev.* **49** 537

[8] Slater J. C. (1936) *Phys. Rev.* **49** 931

[9] Stoner E. C. (1936) *Proc. Roy. Soc. A* **154** 656

[10] Stoner E. C. (1938) *Proc. Roy. Soc. A* **165** 372

[11] Janak J. F. (1977) *Phys. Rev. B* **16** 255

[12] Gunnarsson O. (1976) *J. Phys. F: Metal. Phys.* **6** 587

[13] Morrish A. H. (1965; 2001) *The physical principles of magnetism* John Wiley & Sons; An IEEE Press Classic Reissue

[14] Korringa J. (1947) *Physica* **14** 392

[15] Kohn W. and Rostocker N. (1954) *Phys. Rev.* **94** 1111

[16] Kohn W., Sham L.J. (1965) *Phys. Rev. A* **140** 1133

[17] Wohlfarth E. P., Rhodes P. (1962) *Phil. Mag.* **74** 1817

[18] Goto T., Shindo Y., Takahashi H., Ogawa S. (1997) *Phys. Rev. B* **56** 14019

[19] Goto T., Aruga Katori H., Sakakibara T., Mitamura H., Fukamichi K., Murata K. (1994) *J. Appl. Phys.* **76** 6682

[20] Wulff M., Fournier J. M., Delapalme A., Gilloin B., Sechovský V., Havela L., Andreev A. V. (1990) *Physica B* **163** 331

[21] Sakakibara T., Goto T., Yoshimura K., Murata K., Fukamichi K. (1990) *J. Mag. Mag. Mater.* **90 − 91** 131

[22] Shimizu M. (1982) *J. Phys. Paris* **43** 155

[23] Wagner D. (1989) *J. Phys.: Condens. Matter* **1** 4635

[24] Hathaway K., Cullen J. (1991) *J. Phys.: Condens. Matter* **3** 8911

[25] Yamada H. (1993) *Phys. Rev. B* **47** 11 211

[26] Barbara B., Gignoux D., Vettier C. (1988) *Lectures on modern magnetism* Springer Verlag Berlin

[27] Shimizu M. (1981) *Rep. Prog. Phys.* **44** 329

[28] Arrott A. (1957) *Phys. Rev.* **108** 1394

[29] Arrott A., Noakes A. E. (1967) *Phys. Rev. Lett.* **19** 786

[30] Mushnikov M.V., Goto T., Kamishima K., Yamada H., Andreev A.V., Shiokawa Y., Iwao A., Sechovský V. (1999) *Phys. Rev. B* **59** 6877

[31] Mushnikov M.V., Goto T., Andreev A.V., Yamada H., Sechovský V. (2004) *J. Mag. Mag. Mater.* **272 − 276** e207

[32] Ruderman M.A., Kittel C. (1954) *Phys. Rev.* **96** 99

[33] Kasuya T. (1956) *Prog. Theory Physics* **16** 45

[34] Yosida K. (1957) *Phys. Rev.* **106** 893

[35] Hückel E. (1931) *Z. Phys.* **70** 204

[36] Brooks M. S. S., Johansson B. (1993) *Density functional theory of the ground–state magnetic properties of rare earth and actinoids in Handbook of magnetic materials* **7** Elsevier Science Publishing

[37] Sechovský V., Havela L. (1998) *Magnetism of ternary intermetallic compounds of uranium (in Handbook of Magnetic Materials 11)* Elsevier Science

[38] Hill H. (1971) *Plutonium 1970 and other actinides* AIME, New York

[39] Johansson B., Skriver H. L. (1982) *J. Mag. Mag. Mater.* **29** 217

[40] Sechovský V., Smetana Z., Hilscher G., Gratz E., Sassik H. (1980) *Physica* **102B** 277

[41] Koelling D. D., Dunlap B. D., Grabtree G. W. (1985) *Phys. Rev. B* **31** 4966

[42] Brooks M. S. S., Kelly P. J. (1983) *Phys. Rev. Lett.* **51** 1709

[43] Cooper b. R., Siemann R., Yang D., Thayamballi P., Banerjea A. (1985) *Hybridization induced anisotropy in cerium and actinide systems (in Handbook on the Physics and Chemistry of the Actinides 2)* Elsevier Science

[44] Claeyssen F., Lhermet N., Le Letty R., Bouchilloux P. (1997) *J. Alloys Comp.* **258** 61

[45] Doerr M., Rotter M., Lindbaum A. (2005) *Adv. in Phys.* **54** 1

[46] Barron T. H. K. (1980) *Adv. in Phys.* **4** 609

[47] E. du Tremolet de Lacheisserie (1993) *Magnetostriction: Theory and appliccations of magnetoelasticity* CRC Press, Boca Raton

[48] Poltierová Vejpravová J. (2007) *Impurities in rare earth metallic systems* PhD Thesis, Universita Karlova

[49] http://www.qdusa.com/products/ppms.html

[50] Handler P., Mapother D. E., Rayl M. (1967) *Phys. Rev. Lett.* **19** 356

[51] Sullivan P. F., Seidel G. (1968) *Phys. Rev.* **173** 679

[52] Bachmann R., DiSalvo Jr. F. J., Geballe T. H., Greene R. L., Howard R. E., King C. N., Kirsch H. C., Lee K. N., Schwall R. E., Thomas H.-U., Zubeck R. B. (1972) *Rev. Sci. Instr.* **43** 205

[53] Schnelle W., Engelhardt J., Gmelin E. (1999) *Cryogenics* **39** 271

[54] Swenson C. A. (1999) *Rev. Sci. Instr.* **70** 2728

[55] Hwang J. S., Lin K. J., Tien C. (1996) *Rev. Sci. Instr.* **68** 94

[56] Kennedy C. A., Stancescu M., Marriott R. A., White M. A. (2007) *Cryogenics* **47** 107

[57] Lashley J. C., Hundley M. F., Migliori A., Sarrao J. L., Pagliuso P. G., Darling T. W., Jaime M., Cooley J. C., Hults W. L., Morales L., Thoma D. J., Smith J. L., Boerio–Goates J., Woodfield B. F., Stewart G. R., Fisher R. A., Phillips N. E. (2003) *Cryogenics* **43** 369

[58] Nowotny H., Gratz (2001) *Boltzmann equation and scattering mechanism in Encyclopedia of Materials: Science and technology* Elsevier Science Publishing

[59] Andersen N. H. (1979) *Phys. Rev. B* **19** 384

[60] Eshelby J. D. (1954) *J. Appl. Phys.* **25** 255

[61] Feder R., Nowick A. S. (1958) *Phys. Rev.* **109** 1959

[62] Simmons R. O., Balluffi R. W. (1960) *Phys. Rev.* **117** 52

[63] James J. D., Spittle J. A., Brown S. G. R., Ewans R. W. (2001) *Meas. Sci. Tech.* **12** R1

[64] Kanagaraj S., Pattanayak S. (2003) *Cryogenics* **43** 399

[65] Valvoda V., Polcarová M., Lukáč P. (1992) *Základy strukturní analýzy* Karolinum, Praha

[66] Baruchel J., Hodeau J. L., Lehmann M. S., Regnard J. R., Schenkler C. (Eds.) (1994) *Neutron and synchrotron radiation for condensed matter studies Vol. I* Springer–Verlag, Berlin

[67] Brückel T., Heger G., Richter D., Zorn R. (Eds.) (2001) *Neutron scattering* Forschungszetrum Jülich GmbH, Jülich

[68] Zeng X., Elsayed–Ali H. E. (1999) *Surf. Sci.* **422** L977

[69] Miyake T., Oodake I., Petek H. (1999) *Surf. Sci.* **427 − 428** 39

[70] Wilson A. J. C. (2006) *International Tables for Crystallography, Vol. C* 490

[71] Bianchini G., Barucci M., Del Rosso T., Pasca E. (2006) *Meas. Sci. Tech.* **17** 689

[72] Cannaerts M., Seynaeve E., Rens G., Volodin A., Van Haesendonck C. (2000) *Appl. Surf. Sci.* **157** 308

[73] Keystone J. R. G., Macpherson J. D., Guptill E. W. (1959) *Rev. Sci. Instr.* **30** 246

[74] Beghi M. C., Luzzi L. (2000) *Rev. Sci. Instr.* **71** 154

[75] Kroeger F. R., Swenson C. A. (1977) *J. Appl. Phys.* **48** 853

[76] White G. K. (1960) *Cryogenics* **1** 151

[77] Fawcett E. (1970) *Phys. Rev. B* **2** 1604

[78] Fawcett E. (1970) *Phys. Rev. B* **2** 3887

[79] Miller D. A., Kauffman J. W., Kannewurf C. R. (1971) *Rev. Sci. Instr.* **42** 155

[80] Brändli G., Griessen R. (1973) *Cryogenics* **13** 299

[81] Genossar J., Steinitz M. (1990) *Rev. Sci. Instr.* **61** 2469

[82] Rotter M., Müller H., Gratz E., Doerr M. (1998) *Rev. Sci. Instr.* **69** 2742

[83] Barcza A. (2006) *Magnetostriction in rare earth elements measured with capacitance dilatometry* Diplomartbait, Univetsität Wien

[84] http://www.andeen-hagerling.com/ah2500a.htm

[85] White G. K., Collins J. G. (1972) *J. Low Temp. Phys.* **7** 43

[86] Chadwick J. (1932) *Nature* **129** 312

[87] Chadwick J. (1932) *Proc. Roy. Soc. A* **136** 692

[88] Chatterji T., Ed. (2005) *Neutron scattering from magnetic materials* Elsevier science, Amsterdam

[89] Clementi E., Roetti C. (1974) *Atomic Data and Nuclear Data Tables* **14** 177

[90] Freeman A. J., Descleaux J. P. (1979) *J. Mag. Mag. Mater.* **12** 11

[91] Descleaux J. P., Freeman A. J. (1978) *J. Mag. Mag. Mater.* **8** 119

[92] Stassis C., Deckman H. W., Harmon B. M., Descleaux J. P., Freeman A. J. (1977) *Phys. Rev. B* **15** 369

[93] Jensen J., Mackintosh A. R. (1991) *Rare Earth Magnetism* Clarendon Press, Oxford

[94] Moon R. M., Riste T., Koehler W. C. (1969) *Phys. Rev.* **181** 920

[95] Busing W. R., Levy H. A. (1967) *Acta Cryst.* **22** 457

[96] http://www.ill.fr/YellowBook/VIVALDI/

[97] http://www.ill.fr/YellowBook/LADI/

[98] Campbell J. W., Hao Q., Harding M. M., Nguti N. G., Wilkinson C. (1998) *J. Appl. Cryst.* **31** 496

[99] Campbell J. W. (1995) *J. Appl. Cryst.* **28** 228

[100] Campbell J. W., Clifton I. J., Harding M. M., Hao Q. (1995) *J. Appl. Cryst.* **28** 635

[101] Wilkinson C., Khamis H. W., Stansfield R. F. D., McIntyre G. J. (1988) *J. Appl. Cryst.* **21** 471

[102] Lehmann M. S., Larsen F. K. (1974) *Acta Cryst.* **A30** 580

[103] Campbell J. W., Habash J., Helliwell J. R., Moffat K. (1986) *Information Quaterly for Protein Crystallography* **18**

[104] Campbell J. W. (1986) *Information Quaterly for Protein Crystallography* **19**

[105] Helliwell J. R., Habash J., Cruickshank D. W. J., Harding M. M., Greenhough M. M., Campbell J. W., Clifton I. J. Elder M., Machin P. A., Papiz M. Z., Zurek S. (1989) *J. Appl. Cryst.* **22** 483

[106] http://www.ccp4.ac.uk/

[107] Andreev A.V., Chernyavsky A., Sechovský V., et al. (2003) *J. Alloys Comp.* **353** 102

[108] Kripyakevich P. I., Markiv V. J., Melnik E. V. (1967) *Dopov. Akad. Nauk Ukr. R.S.R. Ser. A* **8** 750

[109] Dwight A. E., Mueller M. H., Conner R. A. Jr., Wowney J. W., Knot H. (1968) *Trans. Metall. Soc. AIME* **242** 2075

[110] Andreev A.V., Levitin R.Z., Popov Y.F., Yumaguzhin R.Y. (1985) *Sov. Phys. Solid State* **27** 1145

[111] Andreev A.V., Bartashevich M.I., Goto T., Kamishima K., Havela L., Sechovský V. (1997) *Phys. Rev. B* **55** 5847

[112] Mushnikov M.V., Goto T., Andreev A.V., Sechovský V., Yamada H. (2002) *Phys. Rev. B* **66** 064433

[113] Andreev A.V., Koyama K., Mushnikov M.V., Sechovský V., Shiokawa Y., Satoh I., Watanabe K. (2007) *J. Alloys Comp.* **441** 33

[114] Andreev A.V., Mushnikov M.V., Goto T., Sechovský V., Homma Y., Shiokawa Y. (2003) *Physica B* **329 – 333** 499

[115] Andreev A.V., Sechovský V., Mushnikov M.V., Goto T., Homma Y., Shiokawa Y. (2000) *J. Alloys Comp.* **306** 72

[116] Andreev A.V., Homma Y., Shiokawa Y., Sechovský V. (1998) *J. Alloys Comp.* **269** 34

[117] Eriksson O., Johansson B., Brooks M. S. S. (1989) *J. Phys.: Condens. Matter* **1** 4005

[118] Sechovský V., Honda F., Janoušová B., Prokeš K., Svoboda P., Syshchenko O., Andreev A. V. (2003) *Physica B* **328** 95

[119] Honda F., Kagayama T., Havela L., Sechovský V., Andreev A. V. (2000) *Physica B* **284 – 288** 1299

[120] Janoušová B., Andreev A. V., Šebek J., Homma Y., Shiokawa Y., Sechovský V. (2002) *Physica B* **312 – 313** 888

[121] Matsuda T. D., Sugawara H., Aoki Y., Sato H., Andreev A. V., Shiokawa Y., Sechovský V., Havela L. (2000) *Phys. Rev. B* **62** 13852

[122] Sechovský V., Havela L., de Boer F. R., Franse J. J. M., Veenhuizen P.A., Šebek J., Stehno J., Andreev A. V. (1986) *Physica B* **142** 283

[123] Sechovský V., Havela L., Neužil L. , Andreev A. V. (1986) *J. Less. Comm. Met.* **121** 169

[124] Sechovský V., Havela L., Jirman L., Brück E., de Boer F. R., Nakotte H, Ye W., Takabatake T., Fujii H., Suzuki T., Fujita T. (1992) *Physica B* **177** 155

[125] Šebek J., Tuan N. C., Havela L., Sechovský V., Suzuki T., Fujita T., Nohara M., Ikeda S., Goshima H. (1994) *Physica B* **194 – 196** 247

[126] Brück E., de Boer F. R., de Châtel P. F., van der Meulen H. P., Franse J. J. M., Menovsky A. A., Havela L., Sechovský V., Perenboom J. A. A. J., Tuan N. C., Šebek J. (1994) *Phys. Rev. B* **49** 8852

[127] Prokeš K., Bourdarot F., Burlet P., Javorský P., Olšovec M., Sechovský V., Brück E., de Boer F. R., Menovsky A. A. (1998) *Phys. Rev. B* **58** 2592

[128] Prokeš K., Bourdarot F., Burlet P., Olšovec M., Sechovský V., Javorský P., Brück E., Goukassov A., de Boer F. R., Menovsky A. A. (1999) *Physica B* **259 – 261** 246

[129] Sechovský V., Prokeš K., Svoboda P., Syshchenko O., Chernyavski O., Sato H., Fujita T., Suzuki T., Doerr M., Rotter M., Loewenhaupt M., Goukassov A. (2001) *J. Appl. Phys.* **89** 7639

[130] Syshchenko O., Prokeš K., Brück E., Sechovský V. (2002) *Physica B* **312 − 313** 879

[131] Syshchenko O., Prokeš K., Sechovský V., Fujita T., Suzuki T. (2002) *Physica B* **311** 233

[132] Prokeš K., Javorský P., Goukassov A., Brück E., de Boer F. R., Sechovský V., Gortenmulder T. J. (1996) *J. Appl. Phys.* **79** 6358

[133] Prokeš K., de Visser A., Menovsky A. A., Brück E., Sechovský V. (2002) *Physica B* **312 − 313** 872

[134] Sechovský V., Honda F., Svoboda P., Prokeš K., Chernyavski O., Doerr M., Rotter M., Loewenhaupt M. (2003) *Physica B* **329 − 333** 480

[135] Aoki Y., Matsuda T. D., Sugawara H., Sato H., Ohkuni H., Settai R., Onuki Y., Yamamoto E., Haga Y., Andreev A. V., Sechovský V., Havela L., Ikeda H., Miyake K. (1998) *J. Mag. Mag. Mater.* **177 − 181** 271

[136] Yamada H., Mushnikov M.V., Goto T. (2000) *Physica B* **281&282** 218

[137] Kolomiets A., Havela L., Sechovský V., DeLong L. E., Watkins D.B., Andreev A. V. (1998) *J. Appl. Phys.* **83** 6435

[138] Routsi Ch. D., Yakinthos J. K., Gamari-Seale H. (1992) *J. Mag. Mag. Mater.* **117** 79

[139] Canepa F., Cirafici S. (1996) *J. Alloys Comp.* **71** 232

[140] Ho P.-C., Zapf Z. S., Ślebarski A., Maple M. B. (2004) *Phil. Mag.* **84** 2119

[141] Kim M. S., Echizen Y., Umeo K., Tayama T., Sakakibara T., Takabatake T. (2003) *Physica B* **329 − 333** 524

[142] Łątka K., Kmieć R., Gurgul J., Rams M., Pacyna A. W., Schmidt T., Pöttgen R. (2005) *J. Sol. State Chem.* **178** 3101

[143] Łątka K., Kmieć R., Kruk R., Pacyna A. W., Rams M., Schmidt T., Pöttgen R. (2003) *Nucleonika* **48** S35

[144] Mihalik M., Diviš M., Kamarád J., Sechovský V. (2006) *Physica B* **383** 161

[145] Łątka K., Kmieć R., Gurgul J., Pacyna A. W., Rams M., Schmidt T., Pöttgen R. (2006) *J. Mag. Mag. Mater.* **301** 359

[146] Mihalik M., et al. (2007) *in preparation*

[147] Hullinger F. (1995) *J. Alloys Comp.* **218** 44

[148] Dönni A., Kitazawa H., Fischer P., Fauth F. (1999) *J. Alloys Comp.* **289** 11

[149] Nylund A. M., Roger MM. A., Sénateur J. P., et al. (1972) *J. Sol. State Chem.* **4** 115

[150] Higashi I., Kobayashi K., Takabatake T., Kasaya M. (1993) *J. Alloys Comp.* **193** 300

[151] Sakurai J., Yamaguchi Y., Mibu K., Shinjo T. (1990) *J. Mag. Mag. Mater.* **84** 157

[152] Kyogaku M., Kitaoka Y., Nakamura H., Asayama K., Teshima F., Takabatake T., Fujii H., Yamaguchi Y., Sakurai J. (1990) *J. Mag. Mag. Mater.* **90 − 91** 487

[153] Khmelevska T., Svoboda P., Janoušová B., Sechovský V., Chang S., Nakotte H., Torikachvilli M. S. (2001) *J. Appl. Phys.* **89** 7189

[154] Takabatake T., Iwasaki H., Nakamoto G., Fujii H., Nakotte H., de Boer F. R., Sechovský V. (1993) *Physica B* **183** 108

[155] Kadowaki H., Ekino T., Iwasaki H., Takabatake T., Fujii H., Sakurai J. (1993) *J. Phys. Soc. Japan* **62** 4426

[156] Bażela W., Kolenda M., Leciejewicz J., Stuesser N., Szytuła A., Zygmunt A. (1995) *J. Mag. Mag. Mater.* **140 − 144** 881

[157] Kalvius G. M., Kratzer A., Münch K. H., Wagner F. E., Zwirner S., Kobayashi H., Takabatake T., Nakamato G., Fujii H., Kreitzman S. R., Kriefl R. (1993) *Physica B* **186 − 188** 412

[158] Kadowaki H. (1998) *J. Phys. Soc. Japan* **67** 3261

[159] Janoušová B. (2004) *Magnetic state instability in intermetallics with f- and d- electrons RPtSn compounds (R = La — Nd)* PhD Thesis, Charles University

[160] Janoušová B., Sechovský V., Prokeš V, Komatsubara T. (2003) *Physica B* **328** 145

[161] Janoušová B., Sechovský V., Sushko Yu. V., Komatsubara T. (2003) *Acta Phys. Polonica B* **34** 1039

[162] Sakurai J., Kawamura R., Taniguchi T., Nishigori S., Ikeda S., Goshoma H., Suzuki T., Fujita T. (1992) *J. Mag. Mag. Mater.* **104 – 107** 1415

[163] Adroja D.T., Rainford B.D., Neville A.J., Jansen A.G.M. (1996) *Physica B* **223&224** 275

[164] Ban Z., Sikirica M. (1965) *Acta Cryst.* **18** 594

[165] Zarechnyuk O. S., Kripyakevich P. I., Gladyshevskii E. I. (1965) *Sov. Phys.: Crystallogr.* **9** 706

[166] Parthé E., Chabot B., Braun H. F., Engel N. (1983) *Acta Cryst.* **B39** 588

[167] Eisenmann B., May N., Müller W., Schäfer H. (1972) *Z. Naturforsch. Teil B* **27** 1155

[168] McCall W. M., Narasimhan K. S. V. L., Butera R. A. (1973) *J. Appl. Cryst.* **6** 301

[169] McCall W. M., Narasimhan K. S. V. L., Butera R. A. (1973) *J. Appl. Phys.* **44** 4724

[170] Pinto H., Melamud M., Gurewirz E. (1979) *Acta Cryst.* **A35** 533

[171] Vinokurova L., Ivanov V., Szytuła A. (1991) *J. Mag. Mag. Mater.* **99** 193

[172] Leciejewicz J., Kolenda M., Szytuła A. (1983) *Solid State Comm.* **45** 145

[173] Nojiri H., Uchi M., Watamura S., Motokawa M., Kawai H., Endoh Y., Shigeoka T. (1991) *J. Phys. Soc. Japan* **60** 2380

[174] Takeda K., Konishi K., Deguchi H., Iwata N., Shigeoka T. (1992) *J. Mag. Mag. Mater.* **104 – 107** 901

[175] Shigeoka T., Fujii H., Yonenobu K., Sugiyama K., Date M. (1989) *J. Phys. Soc. Japan* **58** 394

[176] Shigeoka T., Iwata N., Fujii H., Okamoto T., Hashimoto Y. (1987) *J. Mag. Mag. Mater.* **70** 239

[177] Takeda K., Konishi K., Deguchi H., Iwata N., Shigeoka T. (1991) *J. Phys. Soc. Japan* **60** 2538

[178] Sugiyama K., Yonenobu K., Date M., Shigeoka T., Fujii H. (1992) *Physica B* **177** 275

[179] Shigeoka T., Iwata N., Hashimoto Y., Andoh Y, et al. (1989) *Physica B* **156 & 157** 741

[180] Kawae T., Mito M., Hitaka M., Ichikawa F., Shigeoka T., Iwata N., Tageda K. (2000) *J. Phys. Soc. Japan* **69** 586

[181] Ślaski M., Szytuła A. (1982) *J. Less. Comm. Met.* **87** L1

[182] Garnier A., Gignoux D., Iwata N., Schmitt D., Shigeoka T., Zhang F. Y. (1995) *J. Mag. Mag. Mater.* **140 – 144** 899

[183] Rotter M., Doerr M., Zschintzsch M., Lindbaum A., Sassik H., Behr G. (2007) *J. Mag. Mag. Mater.* **310** 1383

[184] Rotter M., Lindbaum A., Barcza A., El Massalami M., Doerr M., Loewenhaupt M., Michor H., Beuneu B. (2006) *Europhys. Lett.* **75** 160

[185] Vejpravová J., Prokleška J., Sechovský V. (2007) *J. Mag. Mag. Mater.* **316** e374

[186] Uhlířová K., Prokleška J., Vejpravová J., Sechovský V., Maezawa K. (2007) *J. Mag. Mag. Mater.* **310** 1753

[187] http://mcphase.de